Università di Pisa

Corso di Laurea Magistrale in Fisica

Anno accademico 2017-2018

Development of a Fast Simulation of the LHCb Calorimeter

Tesi di Laurea Magistrale
Master thesis

Author:
Giacomo Vitali

Supervisors:
Prof. Giovanni Punzi
Dott. Matteo Rama

Contents

Introduction

LHCb is one of the experiments collecting data at the Large Hadron Collider (LHC), and it is the only one specifically designed to perform measurements in the bottom and charm quark sector. Many of the results obtained by LHCb during the first two runs of the LHC have the best available precision, and much larger data samples are expected from the upcoming runs.

The use of very large samples of data to perform precision measurements in LHCb is often accompanied by large samples of simulated data, which are needed to determine reconstruction and selection efficiencies, evaluate systematic uncertainties and optimize the analysis procedure. Unfortunately, simulating the effect of an LHC collision event inside a complex detector like LHCb requires a very large amount of computing time, significantly larger than the time needed to reconstruct a real data event. During Run 2, the production of simulated events has taken more than 80% of the computing resources of the LHCb experiment. Despite this large amount of allocated resources, for some measurements the number of events that was possible to simulate has not been sufficient to make the systematic uncertainty associated to Monte Carlo[1] (MC) statistics small compared to the main systematic uncertainties. The increase in number of events that will need to be simulated in Run 3 to match the higher luminosity and trigger rate will worsen the situation. To face this problem it is necessary to develop new ways to significantly increase the speed of the simulation and the work of this thesis is one of the first efforts in this direction.

In the simulation of a typical LHCb event about 55% of the CPU time used by *Geant4* to simulate particle transportation is spent in the calorimeter system, followed by the Ring Imaging Cherenkov detectors with about 25% (*Geant4* is the software used by most of the high energy experiments, including LHCb, for the detailed simulation of particle interactions with matter). Therefore, in the effort of developing a faster detector simulation it is natural to start from the calorimeter. The aim of my work is the development of a fast simulation of the LHCb calorimeter. Since most of the particles reaching the calorimeter are photons, I have focused my work on these particles. However, the method that I have developed can be applied to all particle types.

To implement a fast simulation of the detector two results must be achieved: the development and test of the fast simulation algorithms and the development of the interface between the new fast simulation and the existing simulation software.

This thesis presents the first effort towards the development of a fast simulation interface for the LHCb simulation software and of an actual fast simulation engine. The interface must be designed to be flexible enough to allow the users to choose for which subdetector, and for which particles, the fast simulation should replace the standard simulation. Furthermore, for a given subdetector it must allow to activate different fast simulation engines depending on the particle properties.

The development of the fast simulation engine must take into account the wide energy

[1]the term Monte Carlo refers to the simulation of physics events.

range of the photons reaching the calorimeter. For this reason, two different engines can be used for the lower and higher parts of energy spectrum. These models must be tested to evaluate their time and accuracy performances.

This thesis is structured as follows. In Chapter 1 I briefly introduce the LHCb experimental apparatus. In Chapter 2 I describe the role of the simulation at LHCb and I also introduce the problems caused by the low statistics of the available Monte Carlo samples. In Chapter 3 I give an overview on the physics principles of calorimetry and I describe in more detail the LHCb calorimeter. I explain the development of the fast simulation interface and of the actual fast simulation in Chapter 4 and in Chapter 5, respectively. Finally, the results of timing and performance tests for the created fast simulations, as well as the analysis of real data compared with Monte Carlo samples, are showed in Chapter 6.

Chapter 1

The LHCb experiment

The primary goal of LHCb is to search for effects of physics beyond the Standard Model (SM) and to characterize its properties. The experiment has a wide physics program [1, 2] covering many important aspects of Heavy Flavor, Electroweak and QCD physics.
In this Chapter I describe briefly the LHC and the LHCb detector.

1.1 The Large Hadron Collider

The LHC [3] is a proton–proton (pp) and heavy ion collider operating in the European Organization for Nuclear Research (CERN) laboratory, on the French-Swiss border, near Geneva. The LHC is installed in a 27 km long, nearly circular tunnel located about 100 m underground. Before circulating into the LHC, protons are extracted from hydrogen and accelerated by a succession of machines with increasingly higher energies, as shown in Fig. 1.1. Protons are injected into the Proton Synchroton Booster (PSB) at an energy of 50 MeV from Linac 2. The booster accelerates them to 1.4 GeV. The beam is then fed to the Proton Synchrotron (PS) where it is accelerated to 25 GeV. Protons are then sent to the Super Proton Synchrotron (SPS) where they are accelerated to 450 GeV. Finally, they are transferred to the LHC (both in clockwise and anticlockwise direction) where they are accelerated up to 6.5 TeV. Beams collide in four points placed along the LHC ring, where the detectors of the four main experiments ATLAS, CMS, LHCb and ALICE are installed.
The LHC machine is designed to collide protons up to a centre-of-mass energy (E_{cm}) of 14 TeV, at an instantaneous luminosity of 10^{34} cm^{-2}s^{-1}. During Run 1, E_{cm} was equal to 7 TeV in 2010 and 2011, and equal to 8 TeV in 2012. During Run 2, which started in 2015 and will end in 2018, E_{cm} has been 13 TeV.

1.2 The LHCb detector

The LHCb detector [4] is a single-arm spectrometer with a forward angular coverage ranging from approximately 15 mrad to 300 (250) mrad in the bending (non bending) plane, corresponding to a pseudorapidity interval of $1.8(2.07) < \eta < 4.9$ [1] and θ is the polar angle with respect to the beam direction. It is composed of a charged particle tracking system and a particle identification system. The layout of the LHCb detector is shown in Fig. 1.2. The tracking system includes a magnet and three detectors: the

[1] $\eta = -\log[\tan(\theta/2)]$

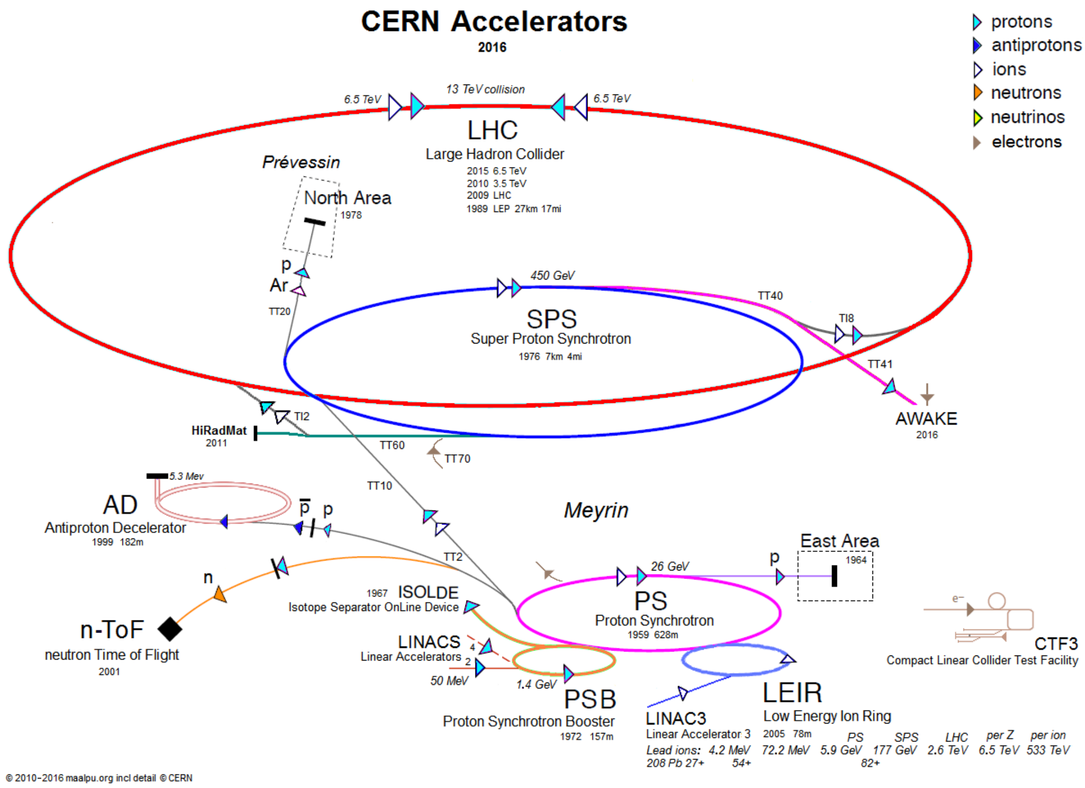

FIGURE 1.1: Schematic representation of the CERN accelerator complex.

Vertex Locator (VELO) and the Tracker Turicensis (TT), both upstream of the magnet, and a system of three tracking stations (T1–T3), downstream of the magnet. These detectors employ two technologies: the Outer Tracker (OT), used in the outer section of T1-T3 and the Silicon Tracker, used in the T1-T3 area around the beam pipe, called the Inner Tracker (IT). The particle identification system includes several detectors, each one exploiting a different technology: two ring imaging Cherenkov (RICH) detectors, the calorimeter system and the muon system. The right handed coordinate system has the x axis pointing toward the center of the LHC ring, the y axis pointing upwards, and the z axis pointing along the beam direction. The design and forward geometry of the LHCb detector allow to exploit unprecedented heavy flavor production rates.

The detector cannot be readout at a rate higher than 1 MHz. When the beams intersect, multiple primary pp interactions may occur causing high particle occupancy in the detector. This makes the events difficult to manage, especially for online systems, and high particle density may cause important radiation damage to the detector. For these reasons the nominal LHC luminosity is reduced in the LHCb intersection point and the average number of primary pp interaction per bunch crossing is reduced to almost 1. The technique of luminosity leveling is used, defocusing the beams by moving them apart transversely. The LHC has recorded a luminosity of $\approx 4 \times 10^{32}\ cm^{-2}s^{-1}$ in Run 1 and of $\approx 1.0 \times 10^{34}\ cm^{-2}s^{-1}$ in Run 2, well above the design value. The recorded LHCb integrated luminosity in 2015 and 2016 is shown in Fig. 1.3.

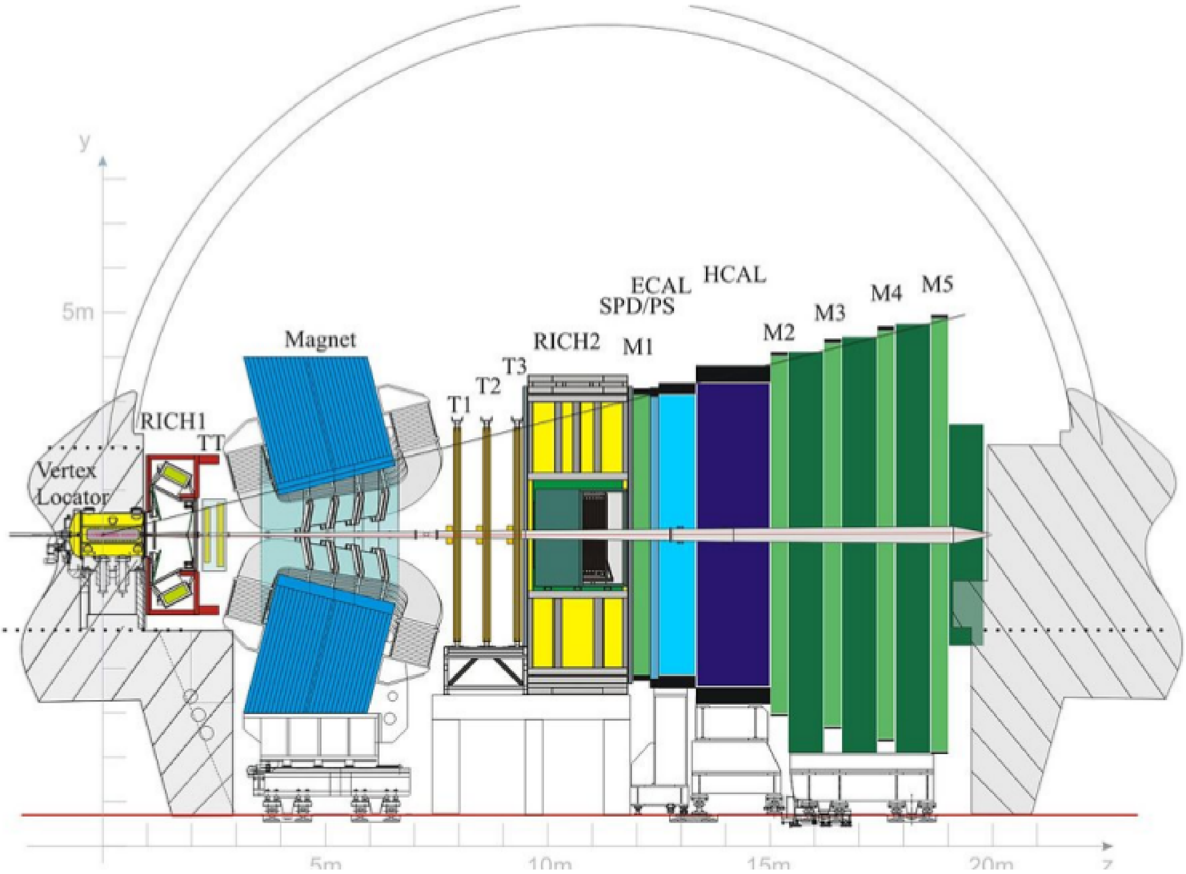

FIGURE 1.2: Layout of the LHCb detector.

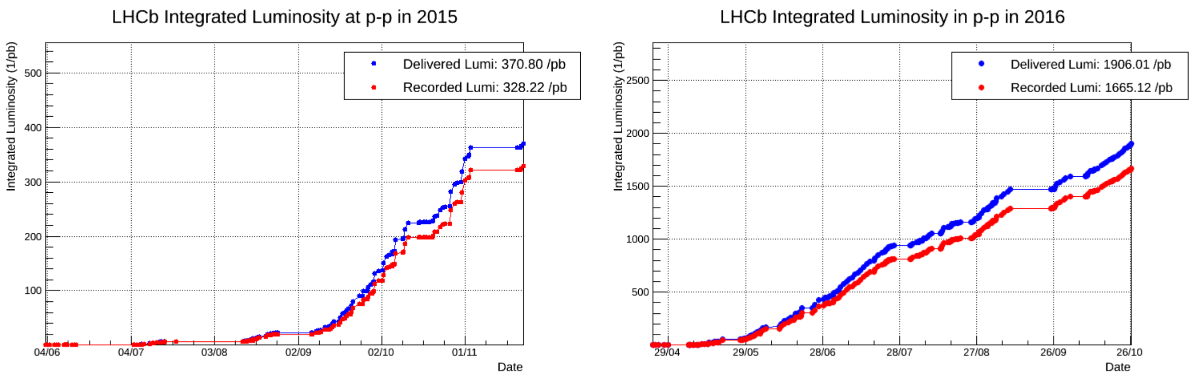

FIGURE 1.3: Integrated LHCb luminosity in 2015 (left) and 2016 (right).

1.2.1 The tracking system

The tracking system must provide accurate spatial measurements of charged particle tracks, in order to allow quantities such as charge, momentum, and vertex locations to be determined.

The dipole magnet

The LHCb warm dipole magnet provides bending of charged particles for the measurement of their momentum. The magnet is formed by two coils placed with a small angle with respect to the beam axis, in order to follow the acceptance of the LHCb detector. The main component of the magnetic field is along the y-axis as shown in Fig. 1.4 and the x,z plane can be considered with good approximation the bending plane. The maximum

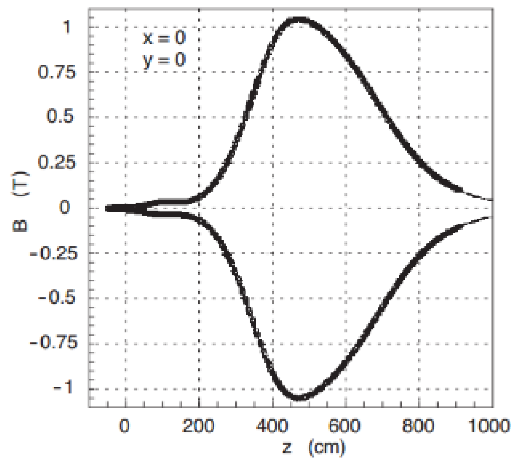

FIGURE 1.4: Measured B_y component of LHCb magnetic field for the two polarity (Up and Down).

magnetic field strength is above 1 T, while its integral is about $\int B\,dl = 4$ Tm. All the tracking detectors are located outside the magnetic dipole. The magnetic field is measured before the data-taking periods with Hall probes to obtain a precise map, which is crucial to have a good momentum resolution and consequently a good mass resolution that helps select the processes of interest. Among the main LHC experiments, the LHCb detector is the only one that has the possibility to reverse the polarity of the magnetic field. This allows a precise control of the charge asymmetries introduced by the detector. Particles hit preferentially one side of the detector, depending on their charges, and this can generate non-negligible detection asymmetries. If data samples collected with the two different polarities have approximately equal size and the operating conditions are stable enough, effects of detection charge asymmetries are expected to significantly decrease. The magnet polarity is therefore reversed approximatively every two weeks to meet these constraints.

The VELO detector

The VErtex LOcator (VELO) [5] measures charged particle trajectories in the region closest to the interaction point. Its main purpose is the reconstruction of primary vertices and displaced secondary vertices, the latter being a signature of heavy flavor decays. Typical b hadrons in LHCb have a decay length $c\beta\gamma\tau \approx$ 7mm, so the vertex detector spatial resolution is required to be far better to discriminate between primary vertices and displaced secondary vertices. The vertex detector consists of 21 disk–shaped tracking stations positioned along the beam axis, both upstream and downstream of the nominal interaction point. Each tracking station is divided in two retractile halves, referred to as modules, each one consisting of two silicon strip sensors, one with radial and one with azimuthal segmentation, as shown in Fig 1.5. Both r and ϕ sensors are centred around the

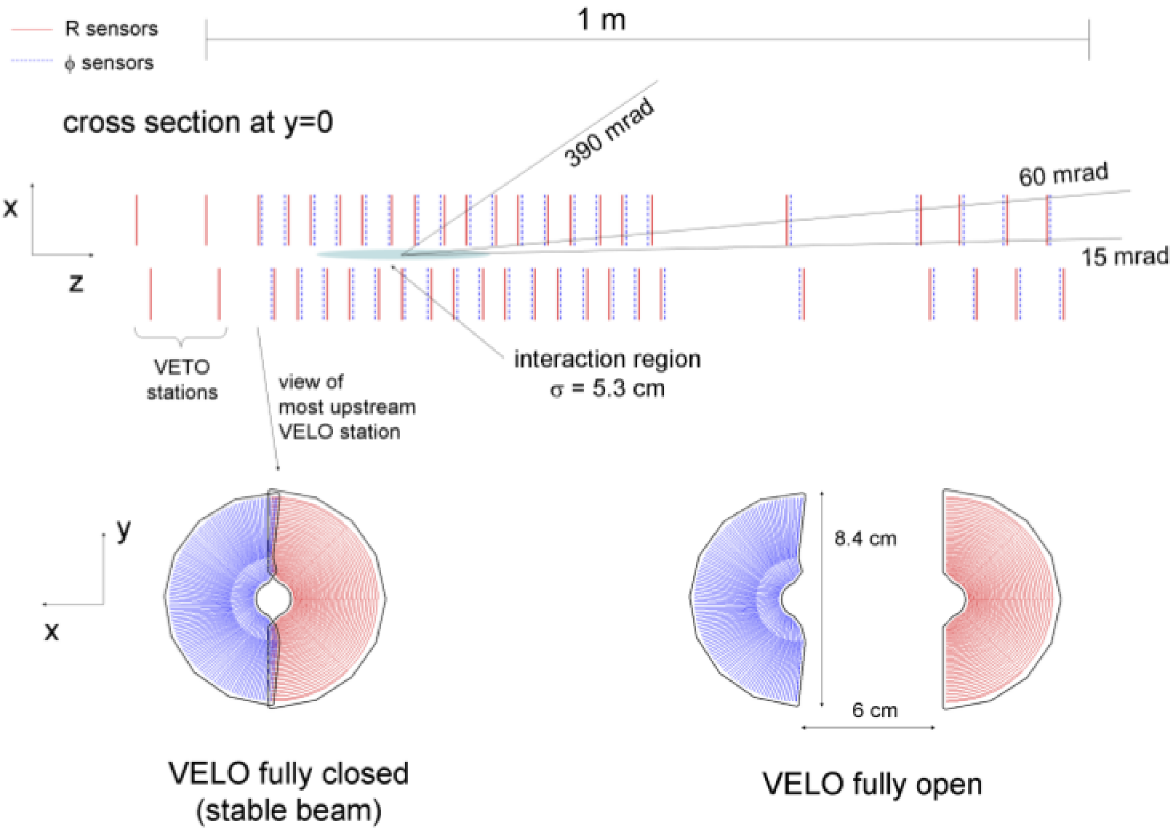

FIGURE 1.5: Representation of the VELO detector, with a transverse view in the (x,z) plane (top) and a front-view of a single station (bottom).

nominal beam position and have a sensitive area covering the region from r = 8 mm to r = 44 mm. The r sensor consists of concentric semicircular strips, which are subdivided in four 45° sectors each, to reduce occupancy. The pitch increases linearly from 38 μm at the innermost radius to 101.6 μm at the outermost radius. The ϕ sensor is subdivided in two concentric regions: the inner region with r in the range 8 - 17.25 mm, the outer region with r between 17.25 and 42 mm. The pitch increases linearly from the centre, with a discontinuity in passing from the inner to the outer region. A representation of the $r\Phi$ geometry of VELO sensors is shown in Fig. 1.6.

Each VELO module is encased in a shielding box to protect it from the radiofrequency electric field. The VELO performance has been measured in test beams. Raw hit resolution varies from $\approx 10\mu$m to $\approx 25\mu$m. This results in an average decay time resolution for $B_s \to J/\psi\,\phi$ decays of about 45 fs [6], about 3% its lifetime.

The Silicon Tracker: Tracker Turicensis and Inner Tracker

The Silicon Tracker [7] consists of two detectors based on the same technology and sharing a similar design: the TT, upstream of the magnet, and the IT, downstream of it. Both TT and IT use silicon microstrip sensors with a strip pitch of about 200 mm. The TT consists of a silicon microstrip detector placed just before the dipole magnet. It consists

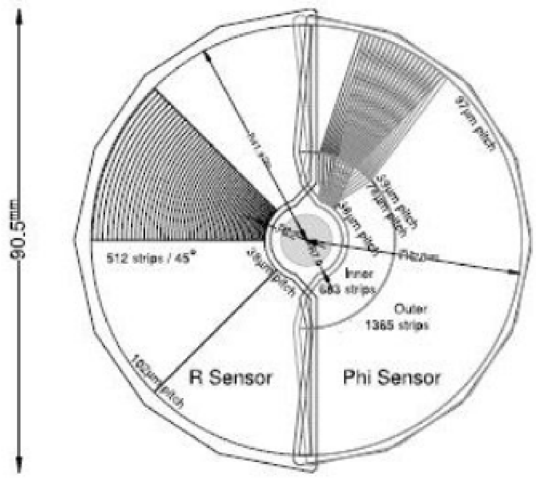

FIGURE 1.6: $r\Phi$ geometry of VELO sensors.

of four layers grouped in two stations separated by about 30 cm along the beam line. The four layers are arranged in a "x-u-v-x" pattern. The first and last layer ("x" configuration) consist of vertical strips (Fig. 1.7) while the "u" and "v" layers are rotated by $\pm 5°$. The slight rotation with respect to the vertical layers avoids the ambiguities that would arise with a horizontal orientation providing a measurement in the y-direction as well. The TT has two purposes: reconstructing trajectories of low-momentum particles that are swept away from the acceptance by the magnet and reconstructing long-lived particles, as K^0_S and Λ, which decay outside the VELO region.

The IT is mounted in three tracking stations, called T-stations, each one with four overlapped detection planes. Planes configuration is the same as that of TT sub-detectors. The purpose of IT is to reconstruct tracks that passed through the magnetic field region near the beam axis. The TT covers the full acceptance of the experiment while the IT, placed downstream of the magnet, covers an acceptance of $\simeq 150 - 200$ mrad in the bending plane and $\simeq 40 - 60$ mrad in the $y - z$ plane. The IT layout is shown in Fig. 1.8. The single-hit resolution of both TT and IT detectors is $\simeq 50\,\mu$m.

The Outer Tracker

The Outer Tracker (OT) [8] is a gaseous ionisation detector consisting of straw tubes operating as proportional counters. As the IT, the OT is arranged in three stations composed of four detection planes. The plane configuration is equal to the IT and the TT ones (x-u-v-x). The drift tubes are 2.4 m long with an inner diameter of 4.9 mm. The gas mixture filling the tube is $Ar(75\%)/CF_4(15\%)/CO_2(10\%)$ to achieve a drift time of 50 ns. The position resolution is approximately 200 μm, while typical occupancies are of the order of 10% and the hit efficiency is above 99% for tracks passing close to the centre of a tube. The OT layout is shown in Fig. 1.9.

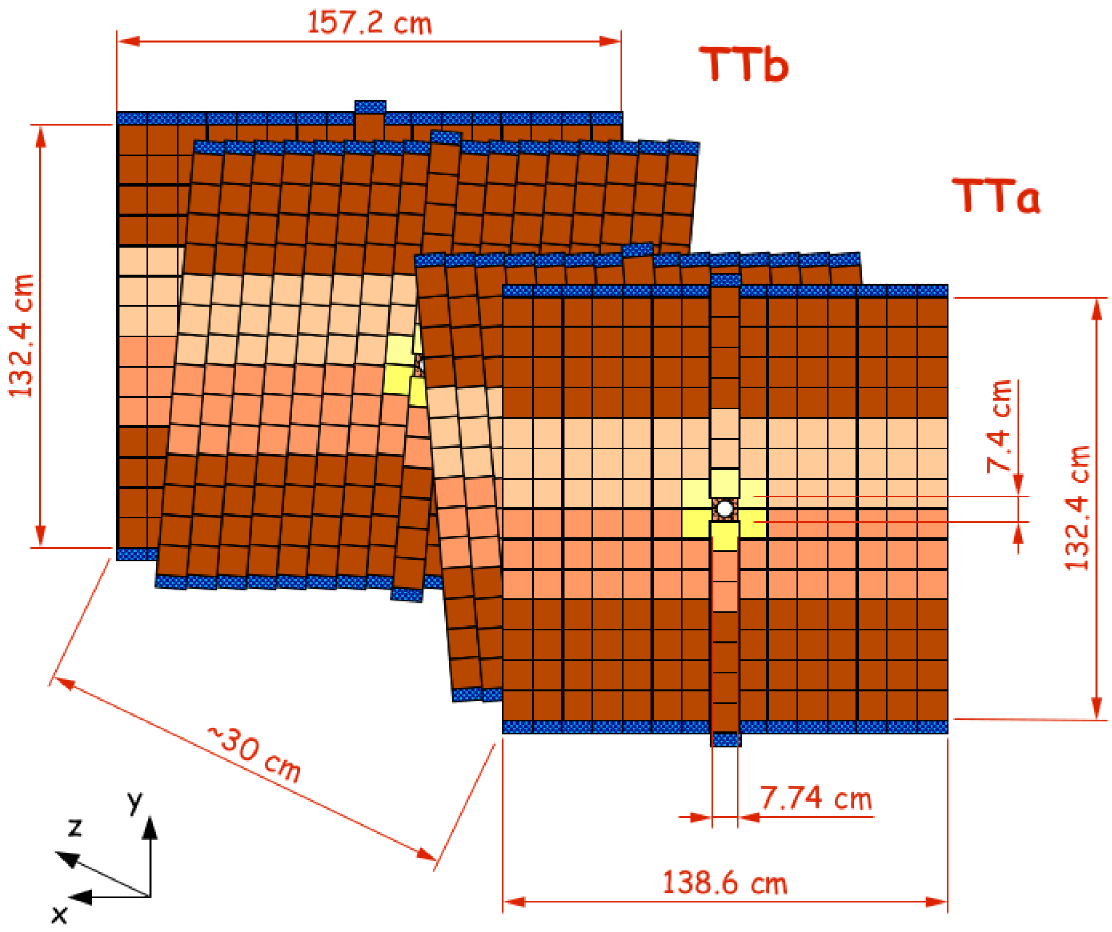

FIGURE 1.7: "x-u-v-x" configuration of the TT station.

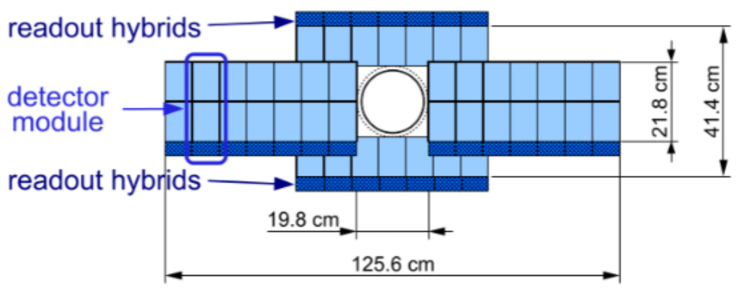

FIGURE 1.8: Layout of one IT layer.

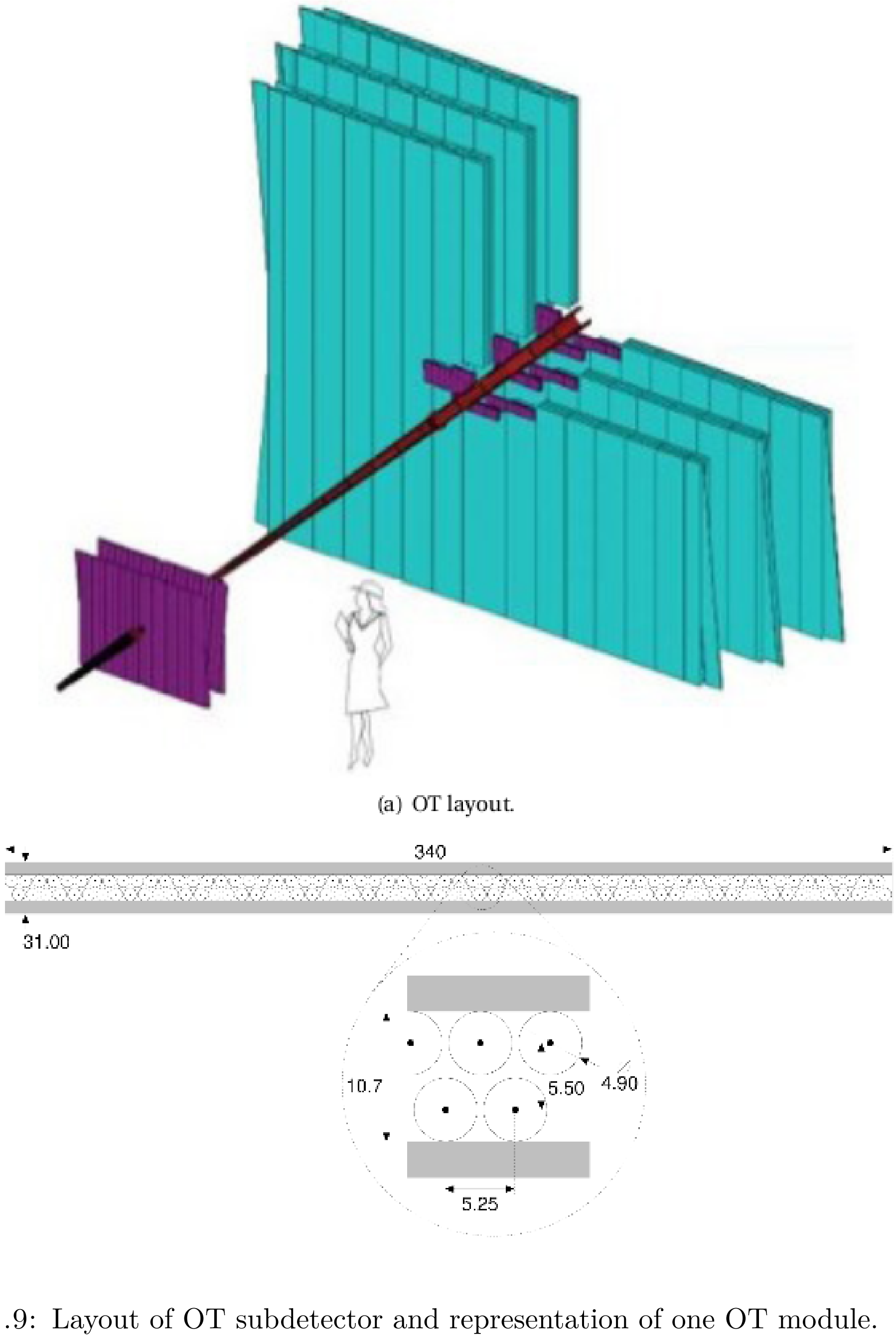

FIGURE 1.9: Layout of OT subdetector and representation of one OT module.

1.2.2 The particle identification system

Particle IDentification (PID) plays an important role in the selection of the decays studied in LHCb. PID information obtained from the Muon, RICH and Calorimeter systems are combined to provide a set of more powerful variables. Cherenkov detectors are able to separate charged kaons and pions, while calorimeter detectors allow the identification of electrons, photons and hadrons. Finally muons are identified by muon chambers.

The Ring Cherenkov detectors

Two Ring Cherenkov detectors, RICH1 and RICH2 [9], allow the identification of charged particles over a momentum range $1 - 100\,\mathrm{GeV}/c$. In particular, RICH1 aims to identify lower-momentum particles (between 1 and 60 GeV/c), while RICH2 is designed for particles with momenta between between 15 and 100 GeV/c. The coverage of different momentum ranges is made possible by filling the two detectors with different radiators: RICH1 uses separate aerogel and C_4F_{10} radiators, while RICH2 is filled with CF_4 radiators. In Fig. 1.10 the relation between the Cherenkov angle and particle momentum for different particles in the C_4F_{10} radiator of RICH1.

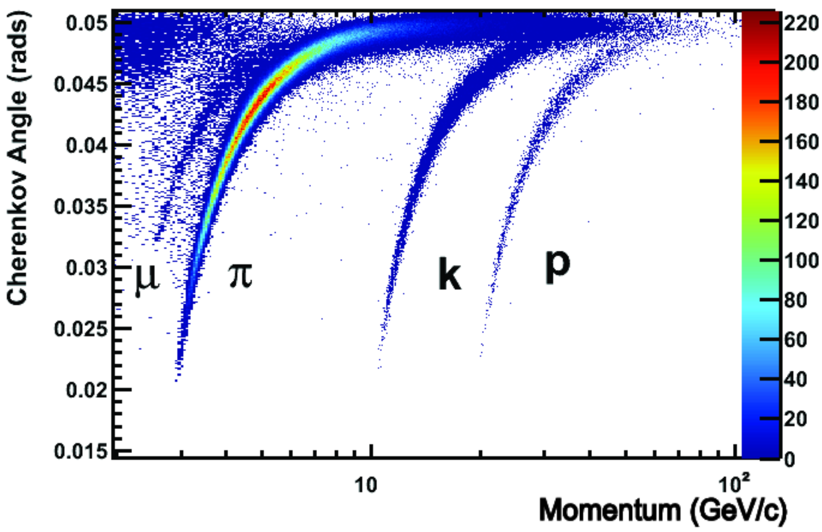

FIGURE 1.10: Cherenkov angle in the C_4F_{10} radiator of RICH1.

In Fig. 1.11 the RICHs geometry is shown. Each detector is composed of two kinds of mirrors: a spherical mirror for ring- imaging and a set of flat mirrors that guide photons onto the Hybrid Photon Detectors, located outside the detector acceptance. The RICHs are magnetically shielded in order to guarantee a proper activity of the hybrid photon detectors. These are used to detect Cherenkov photons with λ between 200 and 600 nm.

RICH1 is located upstream the magnet and covers the full detector acceptance, while RICH2 is downstream the magnet (after the last tracking station) and covers an angular acceptance from 15 to 120 (100) mrad in the bending (non–bending) plane. When averaging over the momentum range 2-100 GeV/c the kaon efficiency is approximately 90% with a pion misidentification rate of about 3% [6].

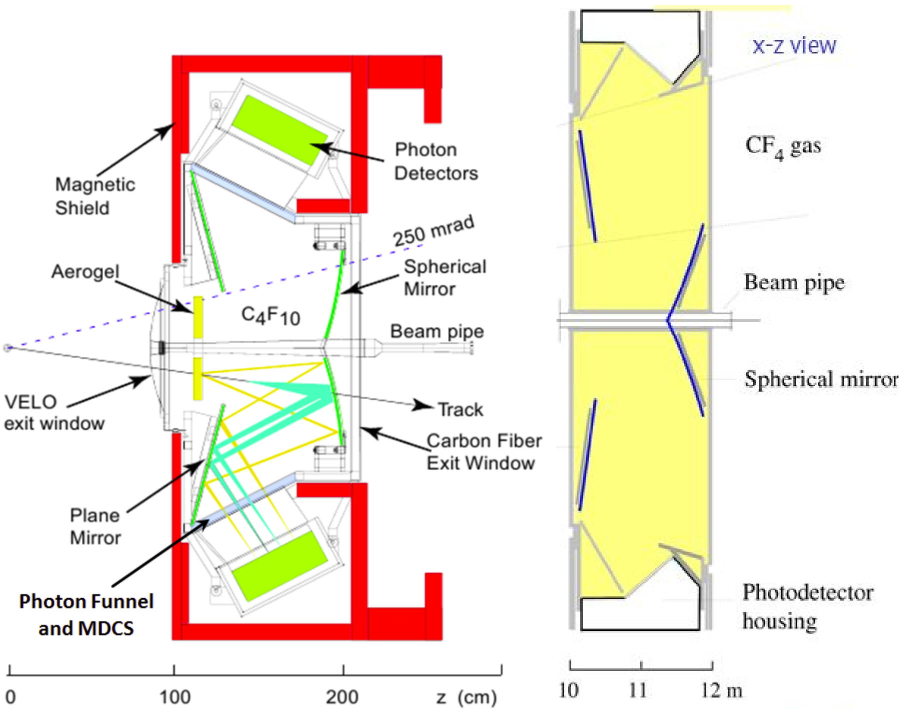

FIGURE 1.11: RICH1 (left) and RICH2 (right) geometry.

Calorimeter detectors

Calorimeter detectors provide fast information for the low level trigger and offer identification of electrons, photons, and hadrons, together with a measurement of their energies and positions.

The calorimetric system is formed by an electromagnetic calorimeter (ECAL) [10] and a hadron calorimeter (HCAL) [11]. Both are placed between the first and the second muon station and cover the angular acceptance from 25 to 300 (250) mrad in the bending (non bending) plane. The electromagnetic calorimeter employs "shashlik" technology of alternating 4 mm thick scintillators tiles and 2 mm thick lead plates arranged perpendicular to the beam pipe. The hadron calorimeter is structured in 4 mm thick scintillator tiles sandwiched between 16 mm iron sheets arranged parallel to the beam pipe. The ECAL is equipped with two additional sub-detectors, a scintillator pad detector (SPD) and a pre-shower detector (PRS), placed in front of it and separated by a 15mm thick lead converter. They are used by the low level electron trigger to better identify charged pions and photons, in order to improve electron identification. Charged pions are rejected by looking at the longitudinal development of the electromagnetic shower in the PRS, which is significantly smaller than the one produced by electrons. The last one is also used to measure the number of tracks per event, in order to veto online too crowded events.

The calorimeter detectors are subdivided in four quadrants that surround the beampipe. Each quadrant has a lateral segmentation in cells of different sizes, depending on the distance from the beam axis. The lateral segmentation is finer in the ECAL, PRS and SPD than in the HCAL, as shown in Fig. 1.12. The ECAL thickness corresponds to

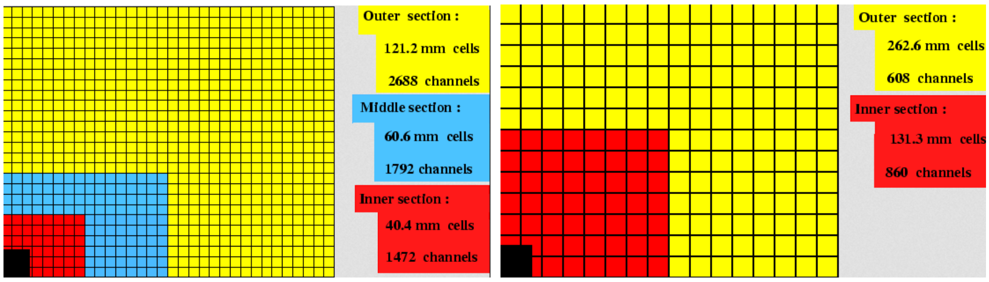

FIGURE 1.12: Segmentation of calorimeter detectors for a detector quadrant of ECAL (left) and HCAL (right).

25 radiation lengths to guarantee a nearly complete electromagnetic shower containment and a good energy resolution. The thickness of HCAL corresponds to 5.6 interaction lengths. The readout is common to all detectors: scintillation light is transmitted to photomultipliers using wavelength shifting fibers. The energy resolution of the ECAL is $\sigma_E/E(\text{ GeV}) \simeq 10\%/\sqrt{E(\text{ GeV})}$ while the energy resolution of the HCAL is $\sigma_E/E(\text{ GeV}) \simeq 70\%/\sqrt{E(\text{ GeV})}$. The Calorimeter is inclined with an angle of 3.601 mrad with respect to the xy plane. A more detailed description of the LHCb calorimeters is found in Chapter 3.

Muon detectors

The muon detectors [12] provide identification of muons for both low level and high level triggers, as well as for offline reconstruction. They also provide a stand-alone measurement of the muon transverse momentum with a resolution of about 20%, used in the low level trigger. They consist of five rectangular stations, referred to as M1-M5, placed along the beam axis and covering the angular acceptance from 20 (16) to 306 (258) mrad in the bending (non bending) plane. The M1 station, which is installed between the RICH2 and the calorimeter detectors, improves the transverse momentum measurements for muons that are detected also in the next stations. The M2-M5 stations are placed downstream of the calorimeter detectors. They are interleaved with 80 cm of iron absorbers that select penetrating muons and result in a total thickness of $\simeq$20 interaction lengths. In order to traverse the whole detector, a muon is typically required to have a minimum momentum of 6 GeV/c. A side view of the muon detectors and a station layout are shown in Fig. 1.13. Two technologies are used to detect muons: triple-GEM (Gas Electron Multipliers) are used in the innermost region of the first station (M1), where high particle density requires a radiation tolerant detector; instead, multiwire proportional chambers are used in the rest of the detectors. The gas mixture consists of Ar , CO_2, and CF_4 for both detectors, although in different proportions (40/55/5% for the MWPC and 45/15/40% for the triple-GEM). The first three stations (M1-M3) contribute to transverse momentum measurements, while the main purpose of the last two stations (M4 and M5) is the identification of penetrating particles. A careful setting of the chamber working point and a precise timing intercalibration allow to reach a muon detection efficiency, mainly determined by the chamber time resolution ($<$ 4ns), well above the design requirement of 99% in all the 5 muon stations.

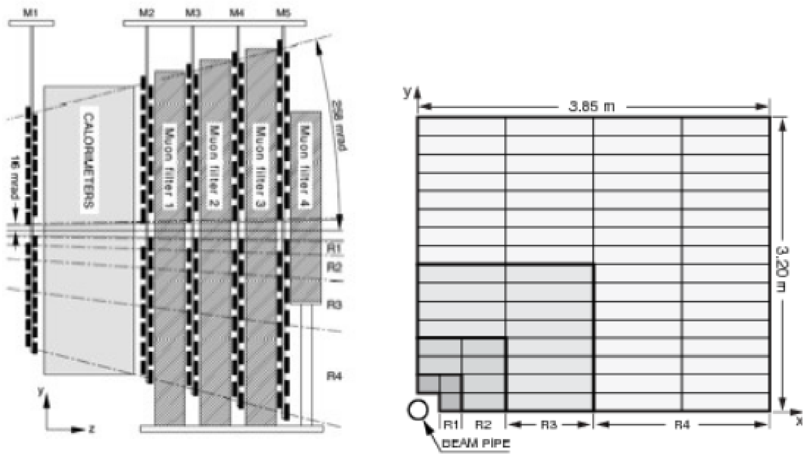

FIGURE 1.13: Side view of muon detectors (left) and geometrical representation of a M1 quadrant (right).

1.3 The LHCb trigger

The LHCb trigger [13] is designed to efficiently select heavy flavor decays among the large light quark background, sustaining the LHC bunch-crossing rate of 40 MHz and selecting up to 12.5 kHz of data to be stored. Events that contain a b-hadron decay, with all possible final states, represent a small fraction, approximately 15 kHz; the corresponding rate for c hadrons is nearly 20 times larger. The subset of interesting b hadron decays corresponds to only few Hz. Therefore, it is a crucial point for the trigger to reject background as early as possible in the data flow. The trigger is organized in two levels, that represent two consecutive stages in event processing: the Level-0 trigger (L0) and the High-Level trigger (HLT). This two-level structure allows coping with timing and selection requirements, with a fast and partial reconstruction at low level, followed by a more accurate and complex reconstruction at high level. The hardware-based L0 trigger operates synchronously with the bunch crossing. It uses information from calorimeter and muon detectors to reduce the 40 MHz bunch–crossing rate to below 1.1 MHz, which is the maximum value at which the detector can be read out by design. In the subsequent step, the asynchronous software-based HLT performs a finer selection based on information from all detectors and reduces the rate to 12.5 kHz, that is the maximum frequency at which events can be stored. In Fig. 1.14 the LHCb trigger flow is shown, with typical rates for the accepted events at each stage.

1.3.1 The Level-0 trigger

The Level-0 trigger consists of three independent trigger decisions: the L0 calorimeter, the L0 muon, and the L0 pileup, the latter being used only for the determination of the luminosity. The L0 decision unit provides the global L0 trigger decision, which is transferred to the readout supervisor board and, subsequently, to the front-end boards. This is necessary since the full detector information for a given bunch crossing is not read out from the front-end boards until the L0 decision unit has accepted it. Data from all detectors are stored in memory buffers consisting in an analog pipeline that is read out with a fixed latency of 4 μs; in this time a trigger decision must be made. To accomplish

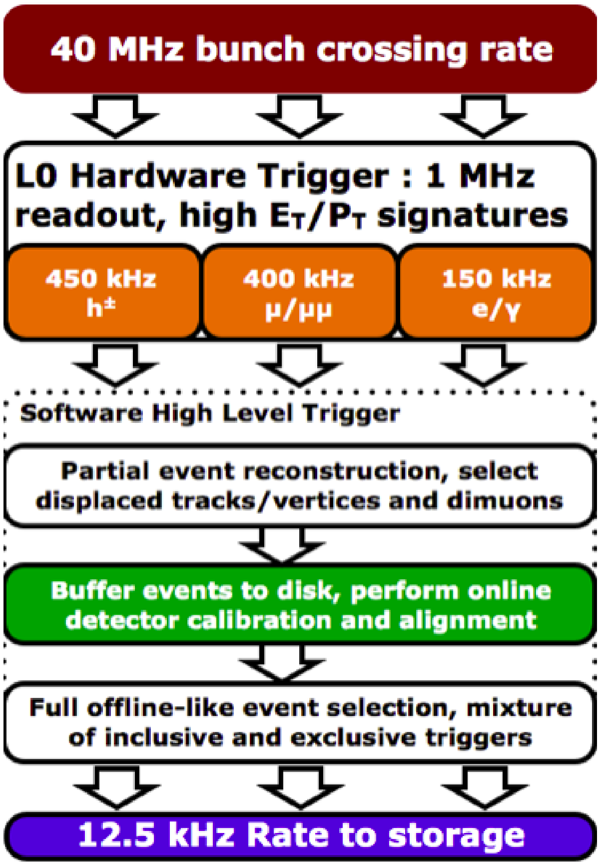

FIGURE 1.14: LHCb trigger flow and typical event-accept rate for each stage.

this task, the L0 trigger is entirely based on custom-built electronic boards, relying on parallelism and pipelining to make a decision within the fixed latency. At this stage, trigger requests can only involve simple and immediately available quantities, like those provided by the calorimeter and the muon detectors.

The L0 muon trigger uses the information from the five muon stations in order to identify the most energetic muons. Once the two highest transverse momentum muon candidates per quadrant are identified, the trigger decision is set depending on two thresholds: one on the highest transverse momentum $p_T^{largest}$ (L0 muon) and one on the product of the two highest transverse momenta $p_T^{largest} \times p_T^{2nd\,largest}$ (L0 dimuon). The p_T of the candidate muons are calculated from the slope of the projection in the bending plane of the trajectory reconstructed by the M1-M3 muon stations.

The L0 calorimeter trigger uses the information from ECAL, HCAL, PRS, and SPD. It calculates the transverse energy deposited in a cluster of 2x2 cells of the same section, for both the electromagnetic and hadron calorimeters. This quantity is combined with information on the number of hits on PRS and SPD in order to define three types of trigger candidates: photon, electron and hadron.

The L0 hadron trigger aims at collecting samples enriched in hadronic c and b particle decays. Final state particles from such decays have on average higher transverse momenta than particles originated from light quark processes. This property helps discriminate between signal and background.

The muon L0 trigger thresholds and the SPD hit multiplicity requirements for Run 1 are listed in Table 1.1.

TABLE 1.1: Typical L0 thresholds used in Run I.

	p_T or E_T		SPD
	2011	2012	2011 and 2012
single muon	1.48 GeV/c	1.76 GeV/c	600
dimuon $p_{T1} \times p_{T2}$	$(1.30\,\mathrm{GeV}/c)^2$	$(1.60\,\mathrm{GeV}/c)^2$	900
hadron	3.50 GeV/c	3.70 GeV/c	600
electron	2.50 GeV/c	3.00 GeV/c	600
photon	2.50 GeV/c	3.00 GeV/c	600

1.3.2 The High Level Trigger

Event accepted at L0 are transferred to the event filter farm, which consists of an array of computers, for the HLT stage. The HLT is implemented through a C++ executable that runs on each processor of the farm, reconstructing and selecting events in a way as similar as possible to the offline processing. The substantial difference between online and offline selection is the available time to completely reconstruct a single event. The offline reconstruction requires almost 2 s per event, while the maximum available time for the online reconstruction is typically 50 ms. The HLT consists of several trigger selections designed to collect specific events. Every trigger selection is specified by reconstruction algorithms and selection criteria that exploit the kinematic features of charged and neutral particles, the decay topology and the particle identities. If the accepted-event rate is too high, individual trigger selections can be prescaled by randomly selecting only a subset of events satisfying the requirements. The total HLT processing time is shared between two different levels: the first stage (HLT1) and the second stage (HLT2). The main differences between HLT1 and HLT2 are the complexity of the information that they are able to process and the available time to do this. Partial event reconstruction is done in the first stage in order to significantly reduce the accepted-event rate to 30 kHz. A more complete event reconstruction follows in the second stage. At the first level, tracks are reconstructed in the VELO and selected based on their probability to originate from heavy flavor decays. At the second level a complete forward tracking of all tracks reconstructed in the VELO is performed. Several trigger selections, either inclusive or exclusive, are available at this stage.

The time needed to store and process this data limits the maximum output rate of the LHCb trigger. So far, LHCb has written out a few kHz of events containing the full raw sub-detector data, which are passed through a full offline event reconstruction before being considered for physics analysis. Charm physics in particular is limited by trigger output rate constraints. A new streaming strategy includes the possibility to perform the physics analysis with candidates reconstructed in the trigger, thus bypassing the offline reconstruction. In the *Turbo stream* the trigger writes out a compact summary of physics objects containing the information necessary for analysis, and this allows an increased output rate and thus higher average efficiencies and smaller selection biases.

1.4 Track reconstruction

Trajectories of charged particles, here referred as tracks, are reconstructed in the LHCb using the hits of the tracking subdetectors [14] (VELO, TT and T-stations). Tracks reconstruction starts with the pattern recognition where a sequence of hits produced by the charged particle is identified. Different types of tracks are distinguished in LHCb according to the subdetectors crossed, as shown in Fig. 1.15:

- **Long tracks** require particles traversing the full tracking system. They are reconstructed combining hits from the VELO and the T-stations, and when possible hits from TT are added.
- **Downstream tracks** are reconstructed only in the TT and in the T-stations. These are mainly long-lived particles as K_s^0 decaying outside the VELO region.
- **VELO tracks** are tracks with only VELO hits. They are used in the primary vertex reconstruction and as seeds for reconstructing long and upstream tracks.
- **Upstream tracks** are low momentum tracks with hits only in the VELO and TT since they are swept out the LHCb acceptance by the magnetic field.
- **T tracks** are formed only using hits into the T-stations.

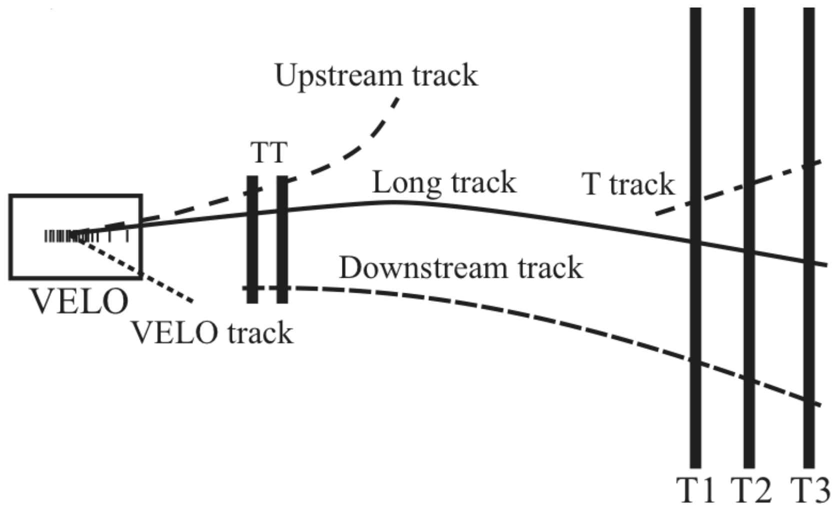

FIGURE 1.15: Track definition in LHCb tracking.

Chapter 2

Role of simulation in LHCb

The possibility to accurately simulate the experimental apparatus is of primary importance to design, build and run a high energy physics experiment. The term *simulation* is often used to generically indicate the generation of the physics event (i. e., in the specific case of LHCb, the generation and possible decay of the particles originating from the pp collision), the simulation of particle interactions with the detector and the simulation of the detector response (Figure 2.1). Since in this thesis I am particularly interested in addressing the time limitations of the simulation, and since in the standard LHCb simulation the event generation and the detector response simulation take less than 5% of the overall CPU time, in the following discussions I will usually refer to *simulation* as the computation of particle interactions with the detector, unless otherwise specified.
In this Chapter first I describe the role of the simulation in two LHCb measurements to give some examples of its possible applications and I discuss another important measurement whose main source of systematic uncertainty is associated to the limited size of the simulated samples. Then I introduce the problem of the large CPU resources needed by the LHCb simulation. Finally, I analyse the CPU time spent by the simulation in the different subdetectors and I identify the subsystem for which a fast simulation is more useful.

2.1 Monte Carlo simulations in LHCb physics analysis

The simulation is used, in one way or another, in most physics measurements performed by LHCb. For the sake of illustration, I will briefly describe in this section the role that the simulation has played in performing a couple of well-known, high-profile measurements performed recently: the measurement of the $B^0_{(s)} \to \mu^+\mu^-$ branching fractions and the measurement of the CP asymmetry in $D^0 \to K^0_S K^0_S$ decays.They are typical examples of situations occurring in many other measurements in similar ways.
Finally I discuss a symbolic example of a physics analysis whose main source of systematic uncertainty is associated to the limited size of the simulated samples.

2.1.1 Measurement of $B^0_s \to \mu^+\mu^-$ branching fraction and effective lifetime and search for $B^0 \to \mu^+\mu^-$ decays.

Within the Standard Model of particle physics, the $B_s \to \mu^+\mu^-$ and $B^0 \to \mu^+\mu^-$ decays are very rare, because they only occur through loop diagrams and are helicity suppressed. In addition their branching fractions are predicted very precisely. All these features make

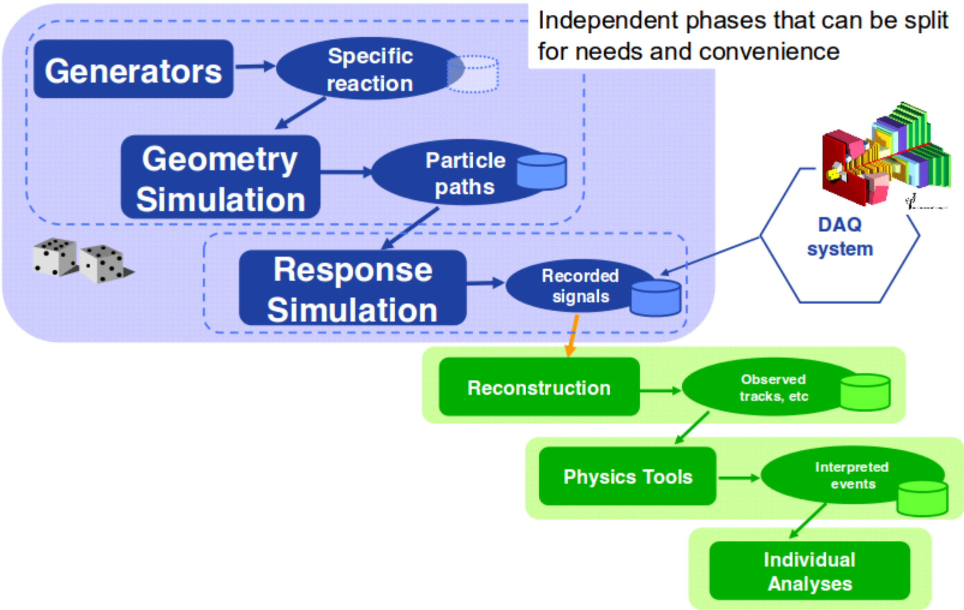

FIGURE 2.1: Generic scheme of the simulation (blue) and reconstruction and analysis (green) steps.

these decays one of the most interesting places to look for physics beyond the SM because a large class of theories, such as, for example, supersymmetry, allows significant modifications to their branching fractions. In a recent measurement based on Run 1 and part of Run 2 data [15], LHCb has reported the first observation of $B_s \to \mu^+\mu^-$ by a single experiment with a significance of 7.8 standard deviations and has measured $BF(B_s \to \mu^+\mu^-) = (3.0 \pm 0.6^{+0.3}_{-0.2}) \times 10^{-9}$, which is the most precise measurement of this quantity to date. No evidence for a $B^0 \to \mu^+\mu^-$ signal has been found and the upper limit $BF(B^0 \to \mu^+\mu^-) < 3.4 \times 10^{-10}$ at 95% confidence level was set. Figure 2.2 shows the mass distribution of the selected $B^0_{(s)} \to \mu^+\mu^-$ candidates. The effective lifetime of $B_s \to \mu^+\mu^-$ is sensitive to new physics in a way complementary to the branching fraction and it has been measured for the first time, $\tau(B_s \to \mu^+\mu^-) = 2.04 \pm 0.44 \pm 0.05$ ps. All results are consistent with the SM predictions and tighten the existing constraints on possible new physics contributions.

Simulated samples have been used in several parts of the measurement. The separation between signal and combinatorial background is achieved by means of a boosted decision tree classifier, optimised using simulated samples of $B_s \to \mu^+\mu^-$ events for signal and $b\bar{b} \to \mu^+\mu^- X$ events for background. The classifier combines the information of a number of variables, including two *isolation* variables which quantify the compatibility of the tracks in the event with originating from the same hadron decay as the two signal muon candidates. These variables can only be optimised using simulated events because it is necessary to identify the real nature of the tracks and this is only possible in simulated events where the *truth* information can be accessed.
Simulated events are also used to determine the detector acceptance, reconstruction and selection efficiencies of signal decays, except for the tracking and particle identification efficiencies which are obtained from control channels in data. In addition, simulated events

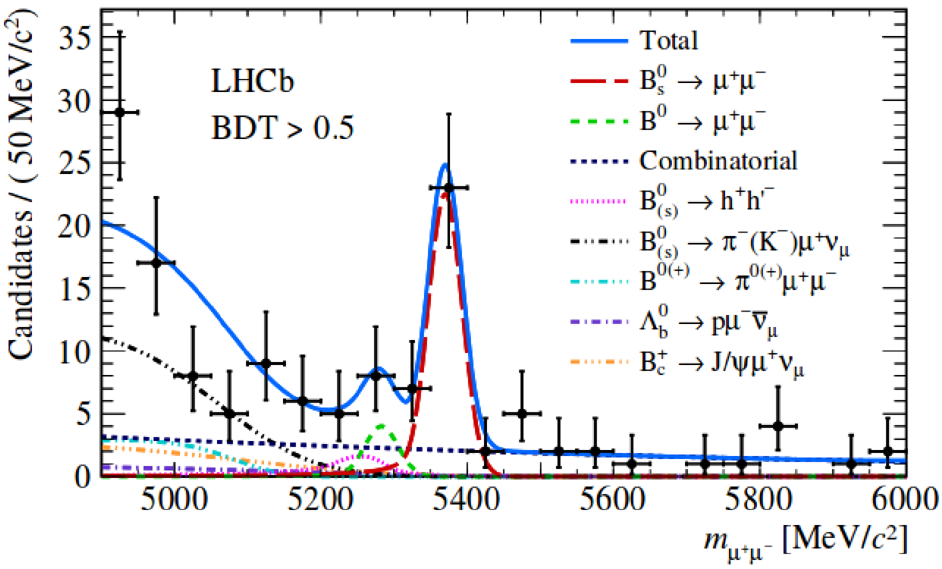

FIGURE 2.2: Mass distribution of the selected $B^0_{(s)} \to \mu^+\mu^-$ candidates (black dots) with BDT > 0.5. The result of the fit is overlaid, and the different components are detailed.

are used to determine the $\mu^+\mu^-$ mass distributions of some specific background sources and the non-Gaussian tails of the signal mass distributions.
Finally, to measure the $\tau(B_s \to \mu^+\mu^-)$ effective lifetime the variation of the selection efficiency as a function of the decay time is needed. The dependency is determined from simulated events.

2.1.2 Measurement of the CP asymmetry in $D^0 \to K^0_S K^0_S$ decays

CP violation in the charm quark sector has not been observed yet. The $D^0 \to K_s K_s$ decay is a promising discovery channel for CP violation because only loop-suppressed amplitudes and exchange diagrams, vanishing in the SU(3) flavour limit, contribute to this decay. LHCb has recently performed a measurement of the time-integrated CP asymmetry in this channel using a 2 fb^{-1} dataset collected in 2015 and 2016. The flavour of the D^0 meson at production is determined from the charge of the bachelor pion in $D^{*+} \to D^0\pi^+$ decays (charge conjugation is implied). The resulting CP asymmetry is $A^{CP}(D^0 \to K_s K_s) = (4.3 \pm 3.4 \pm 1.0)\%$, where the first uncertainty is statistical and the second is systematic [16]. Figure 2.3 shows the value of ΔA^{CP} obtained for each sample, where $\Delta A^{CP} = A^{CP}(D^0 \to K_s K_s) - A^{CP}(D^0 \to K^+K^-)$. The quantity $A^{CP}(K^+K^+)$ has been measured with a precision of 0.2%, thus allowing the determination of $A^{CP}(D^0 \to K_s K_s)$.

In the analysis of $D^0 \to K_s K_s$ decays an important source of background is due to $D^0 \to K_s\pi^+\pi^-$ decays where the $\pi^+\pi^-$ pair satisfies the K_s selection. This channel, whose branching fraction is quite large (about 3%, almost 200 times larger than the signal) is reduced by placing a requirement on the K_s flight distance and on the mass of the $\pi^+\pi^-$ candidates. Simulated signal and background events are used to optimise the cuts on these quantities. Simulated signal events are also used to train a multivariate classifier

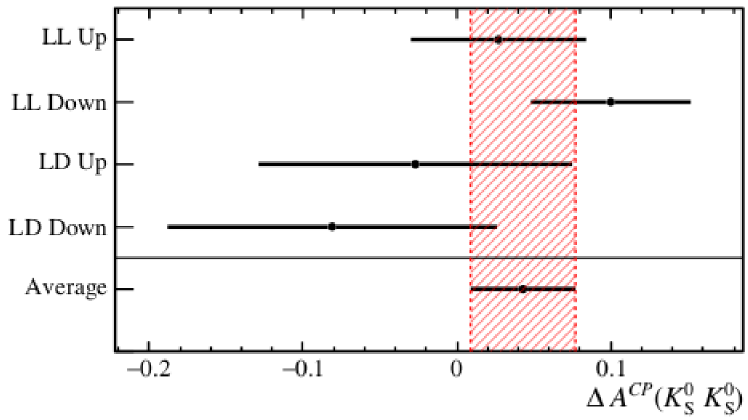

FIGURE 2.3: Values of ΔA^{CP} obtained for both magnet polarities on the LL and LD samples, along with the average of these measurements. LL sample: both K^0_S candidates are long and the other. LD: one K^0_S is long and the other is downstream (long and downstream tracks are defined in Section 1.4). Only statistical uncertainties are shown.

specifically developed to suppress the combinatorial background.
Events in which the D^{*+} meson is not produced in the primary interaction, but instead is the product of a b-hadron decay, are characterised by a different production asymmetry and are treated as background. As such, they are suppressed by exploiting the worse compatibility of the D^0 with originating from the primary vertex (the position of the pp collision). Simulated events are used to estimate the residual fraction of secondary D^{*+}, which allows to estimate the corresponding systematic uncertainty on the CP asymmetry. The uncertainty resulting from this use of the simulation is 20-30% of the total systematic uncertainty.

2.1.3 Test of lepton flavour universality with the measurement of $B^0 \to D^{*-}\tau^+\nu_\tau$

In some important physics analyses, the systematic uncertainty associated to the limited size of the simulated samples is dominant. An example is represented by the measurement of $B^0 \to D^{*-}\tau^+\nu_\tau$.
In the SM differences between the expected branching fraction of semileptonic decays into the three lepton families originate from the different masses of the charged leptons. Further deviations would be a signature of physics processes beyond the SM. The ratio $R(D^*) = BF(B^0 \to D^{*-}\tau^+\nu_\tau)/BF(B^0 \to D^{*-}\mu^+\nu_\mu)$ is predicted in the SM to be about 0.252 with a percent level uncertainty [17]. In recent years there has been a lot of interest on this measurement because different experiments operating either at pp (LHCb) or e^+e^- (BaBar [18], Belle [19]) colliders, using very different experimental techniques, measure values systematically above the SM prediction, resulting in a discrepancy between the average experimental value and the SM prediction of more than 3 standard deviations.
Recently, LHCb has performed a measurement of $R(D^*)$ [20] based on the Run 1 dataset using for the first time $\tau^+ \to \pi^+\pi^-\pi^+\bar{\nu_\tau}$ and $\tau^+ \to \pi^+\pi^-\pi^+\pi^0\bar{\nu_\tau}$ decays, while the D^{*-} was reconstructed through the $D^{*-} \to \overline{D}^0(\to K^+\pi^-)\pi^-$ decay chain. The $B^0 \to D^{*-}\tau^+\nu_\tau$

signal yield is normalized to that of the exclusive $B^0 \to D^{*-}\pi^+\pi^-\pi^+$ decay which has the same charged particles in the final state. This choice minimizes the experimental systematic uncertainties. In practice, the ratio $K(D^{*-}) = \frac{B(B^0 \to D^{*-}\tau^+\nu_\tau)}{B(B^0 \to D^{*-}3\pi)}$ is measured, and the absolute branching fraction is obtained as $B(B^0 \to D^{*-}\tau^+\nu_\tau) = K(D^{*-}) \times B(B^0 \to D^{*-}3\pi)$. The systematic uncertainties on $K(D^{*-})$ are subdivided into four categories: the knowledge of the signal model, including τ decay models; the modeling of the various background sources; possible biases in the fit procedure due to the limited size of the simulated samples; and trigger selection efficiencies, external inputs and particle identification efficiency. Table 2.1 summarizes the most relevant systematic uncertainties of each category. The limited size of the simulation sample determines the largest contribution to the uncertainty (4.1%), with the total being 9.1%.

TABLE 2.1: List of the most relevant individual systematic uncertainties for the measurement of the ratio $R(D^{*-})$.

Contribution	Value in %
$B \to D^{**}\tau^+\nu_\tau$	2.3
$D_s^+ \to 3\pi X$	2.5
D_s^+, D^0 and D^+	2.9
$B \to D^{*-}D_s^+(X)$ and $B \to D^{*-}D^0(X)$ decay model	2.6
$D^{*-}3\pi X$ from B decays	2.8
Size of simulation samples	**4.1**
Online selection	2.0
Offline selection	2.0
Normalization channel efficiency (modeling of $B^0 \to D^{*-}3\pi$)	2.0
Total uncertainty	9.1

Using the branching fraction $B(B^0 \to D^{*-}\pi^+\pi^-\pi^+) = (7.21 \pm 0.29) \times 10^{-3}$ a value of the absolute branching fraction of the $BF(B^0 \to D^{*-}\tau^+\nu_\tau)$ decay is obtained.

$$BF(B^0 \to D^{*-}\tau^+\nu_\tau) = (1.42 \pm 0.094(stat) \pm 0.129(syst) \pm 0.054(ext)) \times 10^{-2}$$

where the third uncertainty originates from the limited knowledge of the branching fraction of the normalization mode. The first determination of $R(D^{*-})$ performed by using three-prong τ decays is obtained by using the measured branching fraction of $BF(B^0 \to D^{*-}\mu^+\nu_\mu)$ and the result is $R(D^*) = 0.291 \pm 0.019(stat) \pm 0.029(syst)$, one of the most precise single measurements performed so far and the one with the best statistical uncertainty. The central value is higher than the SM prediction, although consistent with it at one standard deviation. Figure 2.4 shows a comparison of different measurements of $R(D^*)$. It is interesting to note that the systematic uncertainty associated to the limited size of the simulated samples (0.012) is very close to the statistical uncertainty (0.019).

Data collected in Run 2 already provide a sample twice as large, and it will be of great importance to see if the update of this study will confirm the discrepancy.
As I have shown, the systematic uncertainty associated to the limited size of the simulated samples represents the single most important contribution to the systematic uncertainty

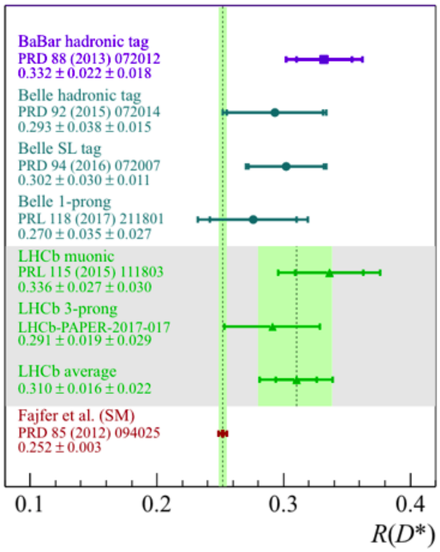

FIGURE 2.4: Measurements of R_{D^*} in LHCb, BaBar and Belle compared to the SM prediction.

of this measurement. In the next section I explain why it was not possible to simulate more events and why the development of a faster detector simulation would help to solve the problem.

2.2 Computing resources used by the simulation

For the first two LHC runs, LHCb has so far produced, reconstructed, recorded and analysed tens of billions of simulated events. As an example, Figure 2.5 shows the number of simulated events as a function of time in 2017 on a weekly basis, categorised by physics working group.

The simulation in Run 2 already accounts for more than 85% of the distributed computing resources available to LHCb, as can be seen from Figure 2.6. Nonetheless, for some analyses the amount of Monte Carlo events that can be produced is already insufficient so that the uncertainty due to the size of the simulated samples is the dominant contribution to the overall systematic uncertainty, as discussed in the case of the $R(D^*)$ measurement in Section 2.1.3. Furthermore, the speed of the standard simulation combined with the limitation of the computing resources implies waits of several months from the time when a simulated sample is requested and the time when it becomes available to the analysts. Eventually, this can cause delays to the publication of the measurements.

In Run 3 the luminosity will increase by a factor five and in addition the trigger efficiency for fully hadronic channels is expected to increase by a factor two. This, in turn, implies an increase in the number of simulated events needed to fulfill the analysis requirements after the trigger selection. The computing budget that can be available by extrapolating the provisions of the last years is unlikely to meet the growing needs of simulated samples with improved accuracy. In this scenario it is essential to optimise the simulation with the ideal goal of simulating all the events needed for the different

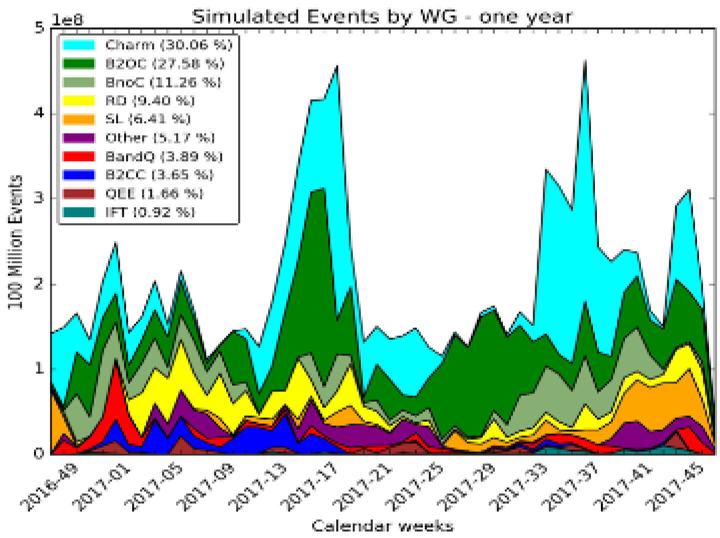

FIGURE 2.5: Number of simulated events per week in 2017, split by physics working group.

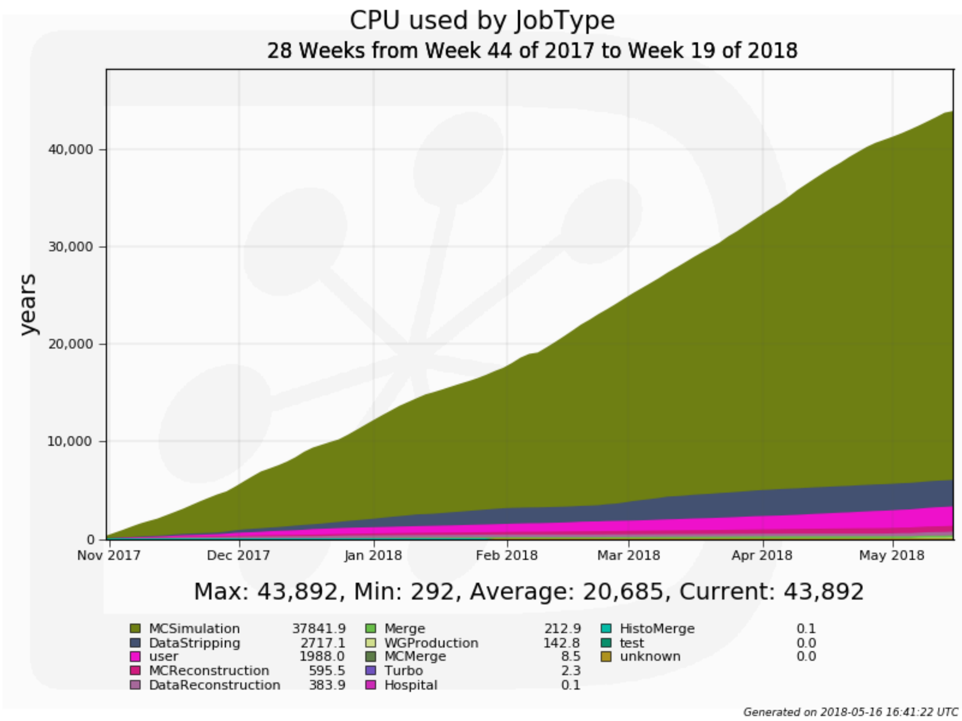

FIGURE 2.6: Computing time usage in LHCb divided by Job type (MC simulation, MC reconstruction, Data reconstruction, stripping, etc.)

analyses.
With this purpose in mind, LHCb has now started a program of accelerating its simulation software, which includes creating new simplified simulation procedures. The goal is to attain an acceleration of the simulation software by at least an order of magnitude,

and this thesis is one of the first efforts in this direction.

2.3 The need of a calorimeter fast simulation

The existing simulation infrastructure needs to be extended to allow the users to choose among alternative simulation options for specific subdetectors. Figure 2.7 shows the distribution of CPU time spent by the standard simulation in different subsystems for simulating 100 minimum bias events [21]. The calorimeter system requires about 55% of the overall CPU time, followed by the RICH detectors with about 25%. Therefore, in the effort of developing a faster detector simulation it is natural to start from the calorimeter.

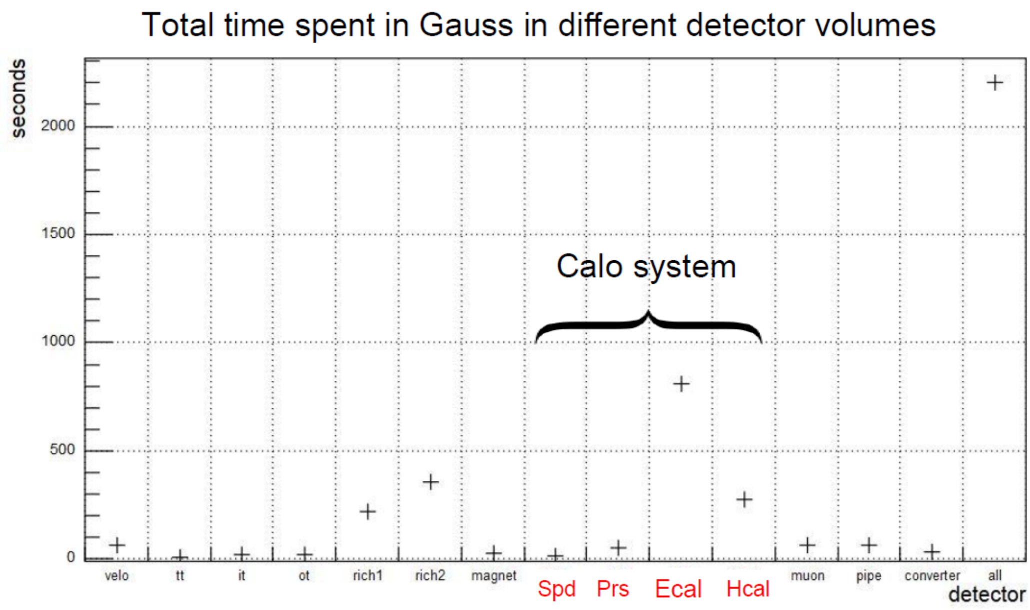

FIGURE 2.7: Distirbution of CPU time spent by the standard simulation in different subsystems for simulating 100 minimum bias events.

The development of a fast simulation of the calorimeter is the subject of this thesis. In Chapter 4 I will describe the development of the interface in the LHCb simulation framework to manage different simulation options for a given subdetector. The interface is designed to give the possibility of selecting different simulation options for different particles depending on their properties. In Chapter 5 I will describe the development of the calorimeter fast simulation. To conclude, in Chapter 6 I will discuss the results.

Chapter 3

The LHCb calorimeter

In particle physics, calorimetry refers to the detection of particles, and measurements of their properties through total absorption in a block of instrumented material, the calorimeter. It was initially invented for the study of cosmic-ray phenomena. This method was then developed and perfected for high energy physics and calorimeters are currently widely used in accelerator-based particle physics experiments in order to measure mainly the energy of electrons, photons and hadrons. Particles to be measured are fully absorbed in the calorimeter and their released energy transformed into a measurable quantity. The electromagnetic or strong interactions of the incident particle with the detector produce a shower of secondary particles with progressively degraded energy. The energy deposited by the charged particles of the shower in the active part of the calorimeter are detected in the form of charge or light and serves as a measurement of the energy of the incident particle.
In this Chapter I describe the physics principles which are the basis of high energy physics calorimetry, the different types of calorimeters and the specific LHCb calorimeter system in detail.

3.1 The physics principles of the calorimetry

The charged particles of a shower release energy through electromagnetic or strong interactions depending on the particle's type and energy. Because of the strength and long range of the Coulomb force relative to the other interactions, for charged particle and photons, the most common processes are the electromagnetic interactions, in particular inelastic collisions with the atomic electrons. The electronic interactions of fast charged particles with speed $v = \beta c$, where β is the ratio of the projectile relative speed to the speed of light c, occur in single collisions with energy losses E, leading to ionization, atomic, or collective excitation. Obviously, the inelastic collitions are statistical in nature, but, because their number per macroscopic pathlength is large, the average energy loss per unit path length (or stopping power) dE/dx can be meaningfully used. For particles with charge ze, where z is the projectile electric charge in electric charge unit, more massive than electrons ("heavy" particles) processes like Cherenkov radiation, nuclear reactions and the emission of electromagnetic radiation arising from scattering in the electric field of a nucleus (bremsstrahlung) are extremely rare and their effects can be ignored. The stopping power for "heavy" particles is well described by the Bethe formula:

$$\left\langle -\frac{dE}{dx} \right\rangle = 2\pi r_e^2 n_{el} m_e c^2 \frac{z^2}{\beta^2}[\ln \frac{2m_e c^2 \beta^2 \gamma^2 T_{max}}{I^2} - 2\beta^2 - K]$$

where

r_e is the classical electron radius
$m_e c^2$ is the electron mass in MeV
$n_e = \frac{N_{av} Z \rho}{A}$ is the material electron density
N_{av} is the Avogadro's number
Z is the material atomic number
A is the material molar mass
I is the mean excitation potential
K is the sum of various corrections
ρ is the material density in $\frac{g}{cm^3}$
$T_{max} = \frac{2 m_e c^2 \beta^2 \gamma^2}{1 + 2 m_e / m_p \gamma + (m_e/m_p)^2}$ is the maximum energy transferred to a single electron
m_p is the proton mass

If the material is a compound, $n_e = \sum_i \frac{N_{av} Z_i w_i \rho}{A_i}$, where w_i is the mass proportion of the i^{th} element, with molar mass A_i and atomic number Z_i.
The K term includes: the shell correction ($2C_e/Z$), due to the interactions between the atomic electrons and nuclei, relevant at low energies ($\simeq 10\%$ for protons with kinetic energy of $T < 2$ MeV) and for heavy projectile ions; density corrections (δ) which take into account the energy loss due to the so-called density-effect, relevant at high $T(\simeq 1GeV)$; Barkas and Bloch corrections.
The energy loss caused by nuclear interactions increases with decreasing projectile speed, but in any case is $< 1\%$ of the energy loss determined by interactions with electrons, so it is usually neglected. Figure 3.1 shows the stopping power for positive muons in copper. Note that at typical energies of muons at LHCb (≈ 10 GeV) radiative effects are $\approx 1\%$ of the total energy loss, which results in few interactions and a very low signal in the calorimeters.

Like heavy charged particles, electron and positrons also loose energy from inelastic collisions when passing through matter, but, because of their small mass, the energy loss by bremsstrahlung radiation cannot be ignored anymore. In fact, at few 10's MeV of the electron energy (called critical energy E_c), the loss of energy from radiation is comparable to or greater than the collision-ionization loss. An approximate formula for E_c is $E_c = 1600 m_e c^2 / Z$. Above E_c, bremsstrahlung dominates completely. The total energy loss for electron and positron is therefore:

$$\left(\frac{dE}{dx}\right)_{tot} = \left(\frac{dE}{dx}\right)_{rad} + \left(\frac{dE}{dx}\right)_{coll}$$

The collision term is the Bethe formula modified to take into account the indistinguishability between the projectile and atomic electrons and the fact that the incident particle doesn't remain undeflected during the collision process. These considerations change some terms in the formula, in particular, $T_{max} = T_e/2$, where T_e is the kinetic energy of the incident electron or positron. The radiative term is:

$$-\left(\frac{dE}{dx}\right)_{rad} = N E_0 \phi_{rad}$$

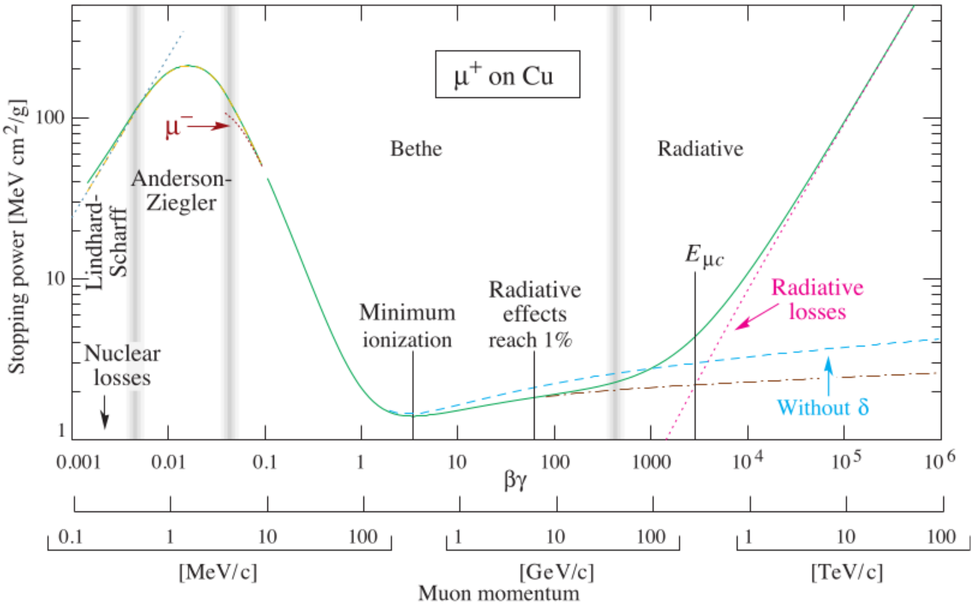

FIGURE 3.1: Stopping power for positive muons in copper as a function of $\beta\gamma = p/Mc$ over nine orders of magnitude in momentum (12 orders of magnitude in kinetic energy). Solid curves indicate the total stopping power. Vertical bands indicate boundaries between different approximations mentioned in the text.

, where

$$\phi_{rad} = \frac{1}{E_0} \int h\nu \frac{d\sigma}{d\nu}(E_0, \nu) d\nu,$$

E_0 the initial electron or positron energy, σ the bremsstrahlung cross section and ν, $h\nu$ the frequency and energy of the emitted photon, respectively.
Contrary to charged particles, photons can't inelastically collide with atomic electrons and, for this reason, have a much smaller interaction cross section and are many times more penetrating in matter than charged particles. The main interactions of high energy photons are the photoelectric effect, the Compton scattering and the pair production. Among these processes, the latter is the most interesting in the high energy physics calorimetry, because is one of two main interactions, the other one being the bremsstrahlung radiation of electrons and positrons, which produce an electromagnetic cascade. The process of pair production involves the transformation of a photon into an electron-positron pair ($\gamma \rightarrow e^+e^-$). In order to conserve momentum, this can only occur in the presence of a third body, usually a nucleus. To create the pair, the photon must have at least an energy $E_{c_{pair}}$ of 1.022 MeV. The cross section is very closely related to that for bremsstrahlung, since the Feynman diagrams are variants of one another. The increasing domination of pair production as the energy increases is shown in Figure 3.2.

As above, high-energy electrons predominantly lose energy in matter by bremsstrahlung, while high-energy photons by pair production. The characteristic amount of matter traversed for these related interactions is called the radiation length X_0, usually measured in g/cm^2. It is both the mean distance over which a high-energy electron loses all but $1/e$

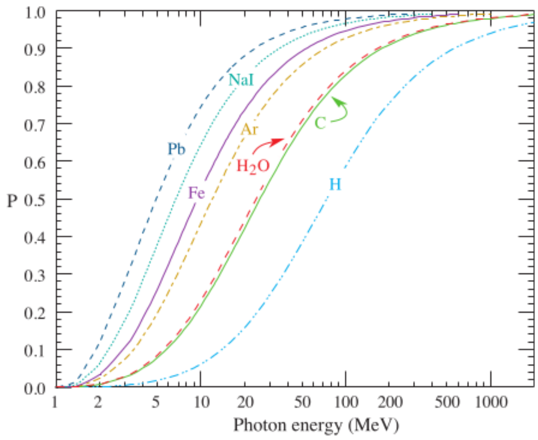

FIGURE 3.2: Probability P that a photon interaction will result in conversion to an e^+e^+ pair. Except for a few-percent contribution from photonuclear absorption around 10 or 20 MeV, essentially all other interactions in this energy range result in Compton scattering off an atomic electron.

of its energy by bremsstrahlung, and 7/9 of the mean free path for pair production by a high-energy photon. It is also the appropriate scale length for describing high-energy electromagnetic cascades. X_0 has been calculated and tabulated by Y.S. Tsai [22]:

$$\frac{1}{X_0} = 4\alpha r_e^2 \frac{N_A}{A}\{Z^2[L_{rad} - f(Z)] + ZL'_{rad}\}$$

For 1 g/mol, $4\alpha r_e^2 N_A/A = (716.408\, g/cm^2)^{-1}$. L_{rad} and L'_{rad} are given by Table 3.1

The function $f(Z)$ is an infinite sum, but for elements up to uranium can be represented to 4-place accuracy by

$$f(Z) = a^2[(1+a^2)^{-1} + 0.20206 - 0.0369a^2 + 0.0083a^4 - 0.002a^6]$$

where $a = \alpha Z$.
The radiation length in a mixture or compound may be approximated by

$$1/X_0 = \sum w_j/X_j$$

where w_j and X_j are the fraction by weight and the radiation length for the jth element.

TABLE 3.1: Tsai's L_{rad} and L'_{rad}, for use in calculating the radiation length in an element.

Element	Z	L_{rad}	L'_{rad}
H	1	5.31	6.144
He	2	4.79	5.621
Li	3	4.74	5.805
Be	4	4.71	5.924
Others	>4	$\ln(184.15Z^{-1/3})$	$\ln(1194Z^{-2/3})$

3.1.1 The electromagnetic cascades

When a high-energy electron or photon is incident on a thick absorber, it initiates an electromagnetic cascade as pair production and bremsstrahlung generate more electrons and photons with lower energy. A high energy photon in matter converts into an electron and positron pair which then emit energetic bremsstrahlung photons. These, in turn, will convert into further e^+e^- pairs, and so on. The result is a cascade or shower of photons, electron and positrons. Electron energies eventually fall below the critical energy and then dissipate their energy by ionization and excitation rather than by the generation of more shower particles. Figure 3.3 shows a schematic of a EM shower.

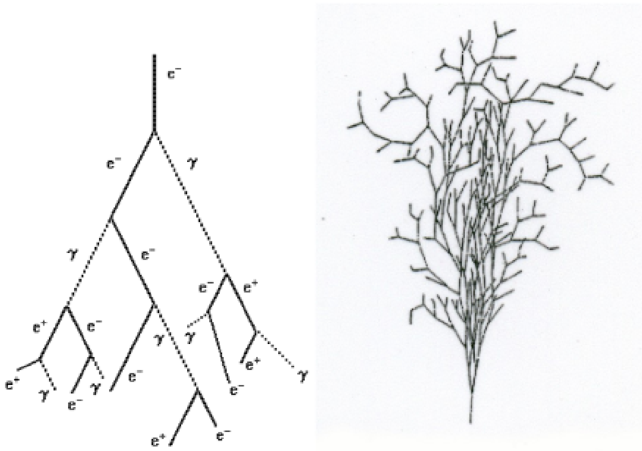

FIGURE 3.3: Schematic of an electromagnetic shower generated from a high energy electron.

The longitudinal development is governed by the high-energy part of the cascade, and therefore scales as the radiation length in the material. In describing shower behavior, it is therefore convenient to introduce the scale variables

$$t = x/X_0$$

$$y = E/E_c$$

so that distance is measured in units of radiation length and energy in units of critical energy.
The mean longitudinal profile of the energy deposition in an electromagnetic cascade is reasonably well described by a gamma distribution:

$$\frac{dE}{dt} = E_0 b \frac{bt^{a-1}e^{-bt}}{\Gamma(a)}$$

Where a and b are the distribution parameters, whose value can be obtained by fitting the gamma distribution to simulated shower profiles in different elements and at different energies. The transverse development of electromagnetic showers in different materials scales fairly accurately with the Molière radius R_M, given by

$$R_M = X_0 E_s / E_c$$

where $E_s \approx 21$ MeV. In a material containing a weight fraction w_j of the element with critical energy E_{cj} and radiation length X_j, the Molière radius is given by $\frac{1}{R_M} = \frac{1}{E_s} \sum \frac{w_j E_{cj}}{X_j}$ On the average, only 10% of the energy lies outside the cylinder with radius R_M. About 99% is contained inside of $3.5 R_M$, but at this radius and beyond composition effects become important and the scaling with R_M fails.

3.1.2 The hadron cascades

If the projectile particle is a high energy hadron, the probability of nuclear interaction is not negligible. When the primary hadron interacts with a nucleus of the target material, it produces secondary particles which, in turn, can interact with other nuclei, and so on. This series of inelastic hadronic interactions creates a hadron cascade (or shower). In detail, in an inelastic hadronic collision a significant fraction f_{em} of the energy is removed from further hadronic interaction by the production of secondary π^0's and η's, whose decay photons generate high-energy electromagnetic showers. Charged secondaries ($\pi^{\pm}$, p, ...) deposit energy via ionization and excitation, but also interact with nuclei, producing spallation protons and neutrons and evaporation neutrons. The charged collision products produce detectable ionization, as do the showering γ-rays from the prompt de-excitation of highly excited nuclei. The recoiling nuclei generate little or no detectable signal. The neutrons lose kinetic energy in elastic collisions, thermalize on a time scale of several μs, and are captured, with the production of more γ-rays usually outside the acceptance gate of the electronics. Between endothermic spallation losses, nuclear recoils, and late neutron capture, a significant fraction of the hadronic energy (20%-40%, depending on the absorber and energy of the incident particle) is used to overcome nuclear binding energies and is therefore lost or "invisible", that is undetectable. In contrast to EM showers, hadronic cascade processes are characterized by the production of relatively few high-energy particles. By definition, $0 \leq f_{em} \leq 1$. Its variance $\sigma^2_{f_{em}}$ changes only slowly with energy, but $\langle f_{em} \rangle \rightarrow 1$ as the projectile energy increases. An empirical power law of the form $\sigma_{f_{em}} = (E/E_1)^{(1-l)}$ (where $l < 1$) describes the energy dependence of the variance adequately.
The hadron shower dimensions are described by the nuclear interaction length , i.e. the mean distance travelled by a hadronic particle before undergoing an inelastic nuclear interaction, $\lambda_I = \frac{A}{N_A \sigma_{int}}$, where σ_{int} is the nuclear interaction cross section. In fact, 95% of a shower is contained in approximately 7.6 λ_I and 95% of the total energy is deposited in a cylinder with radius λ_I. Figure 3.4 shows the longitudinal and transversal hadron shower development for pions in tungsten and iron at different energies.

3.2 The calorimeters in high energy physics

A calorimeter is designed to measure a particle's (or jet's) energy and direction for an (ideally) contained electromagnetic (EM) or hadronic shower. The radiation length X_0 ranges from 13.8 g/cm^2 in iron to 6.0 g/cm^2 in uranium. Similarly, λ_I varies from 132.1 g/cm^2(Fe)

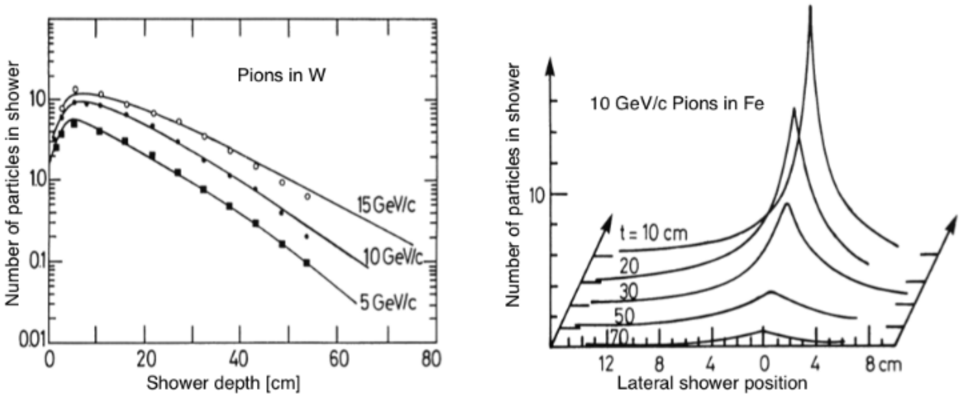

FIGURE 3.4: (Left) Longitudinal hadron shower development for projectile charged pions in W for 3 energies. (Right) Longitudinal and transversal hadron shower development for 10 GeV/c energy π^- in Fe.

to 209 g/cm^2(U). EM calorimeters tend to be 15-30 X_0 deep, while hadronic calorimeters are usually compromised at 5-8 λ_I. In real experiments there is likely to be an EM calorimeter in front of the hadronic section, which in turn has less sampling density in the back, so the hadronic cascade occurs in a succession of different structures. Figure 3.5 shows a typical detector layout in high energy physics experiments and their corresponding response depending on the particle type and charge.

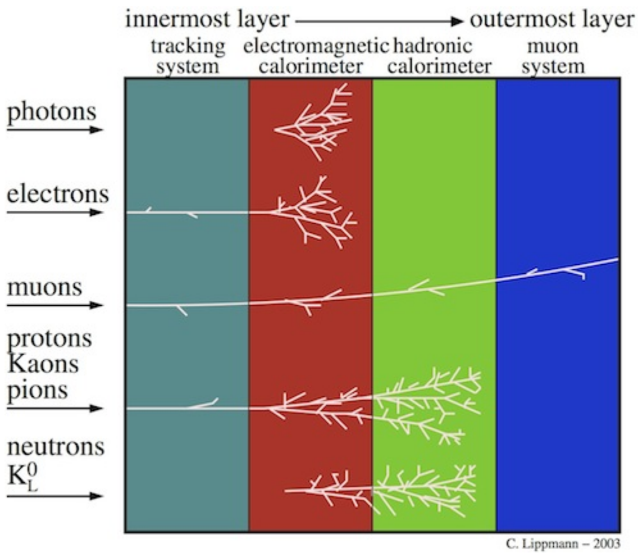

FIGURE 3.5: Typical detector layout in a high energy physics experiment from innermost to outermost layer and the signals left by different particle species.

There are two types of calorimeters:

- sampling calorimeters, consisting of metallic absorbers sandwiched or (threaded) with an active material which generates the signal. The active medium may be a scintillator, an ionizing noble liquid, a gas chamber, a semiconductor, or a Cherenkov radiator. The average interaction length is thus greater than that of the absorber alone, sometimes substantially so.

- homogeneous calorimeters, in which the entire volume is sensitive, i.e., contributes to the signal. Homogeneous calorimeters (usually electromagnetic) may be built with inorganic heavy (high density, high $\langle Z \rangle$) scintillating crystals, non-scintillating Cherenkov radiators such as lead glass and lead fluoride, or noble liquids.

3.2.1 The electromagnetic calorimeters

There are homogeneous and sampling electromagnetic calorimeters. Homogeneous electromagnetic calorimeters may be built with inorganic heavy (high-Z) scintillating crystals such as BaF_2, BGO, CsI, $LYSO$, NaI and PWO, non-scintillating Cherenkov radiators such as lead glass and lead fluoride (PbF_2), or ionizing noble liquids. In a sampling calorimeter, the passive medium is usually a material of high density, such as lead, tungsten, iron, copper, or depleted uranium. The energy resolution σ_E/E of a calorimeter can be parameterized as $a/\sqrt{E} \bigoplus b \bigoplus c/E$, where $\bigoplus$ represents the addition in quadrature and E is in GeV. The stochastic term a represents statistics-related fluctuations such as intrinsic shower fluctuations, photoelectron statistics, dead material at the front of the calorimeter, and sampling fluctuations. Its value is a few percent for a homogeneous calorimeter and typically 10% for sampling calorimeters. The main contributions to the systematic, or constant, term b are detector non-uniformity, calibration uncertainty and radiation damage for the active medium, for calorimeters built for modern high-energy physics experiments. In the case of the hadronic cascades discussed below, non-compensation also contributes to the constant term. The constant term b can be reduced to below one percent. The term c is due to electronic noise summed over readout channels within a few Molière radii.
The position resolution depends on the effective Molière radius and the transverse granularity of the calorimeter. It can be factored as $a/\sqrt{E} \bigoplus b$, where a is a few to 20 mm and b can be as small as a fraction of mm for a dense calorimeter with fine granularity. Electromagnetic calorimeters may also provide direction measurement for electrons and photons. This is important for photon-related physics when there are uncertainties in the event origin (or primary vertex) position, since photons do not leave information in the particle tracking system. Typical photon angular resolution is about 45 mrad$/\sqrt{E}$, which can be provided by implementing longitudinal segmentation for a sampling calorimeter or by adding a preshower detector for a homogeneous calorimeter without longitudinal segmentation. Novel technologies have been developed for electromagnetic calorimetry. In particular the "shashlik" structure, used in the LHCb ECAL, has been developed for sampling calorimetry with wavelength shifting fibers functioning as both the converter and transporter for light generated in the sensitive medium.

3.2.2 The hadron calorimeters

Hadronic calorimetry is considerably more difficult than EM calorimetry. For the same cascade containment fraction of an EM calorimeter, the hadron calorimeter would need to be ∼30 times deeper. Electromagnetic energy deposit from the decay of a small number of π^0's are usually detected with greater efficiency than are the hadronic parts of the cascade, themselves subject to large fluctuations in neutron production, undetectable energy loss to nuclear disassociation, and other effects. At present these are sampling calorimeters: plates of absorber (Fe, Pb, Cu, or occasionally U or W) alternating with plastic scintillators (plates, tiles, bars), liquid argon (LAr), or gaseous detectors. The ionization is measured directly, as in LAr calorimeters, or via scintillation light observed by photodetectors (usually photomultipliers or silicon photodiodes). Wavelength-shifting fibers are often used to solve difficult problems of geometry and light collection uniformity.

Ideally the calorimeter is segmented in ϕ and θ (or $\eta = -\ln\tan(\theta/2)$). Fine segmentation, while desirable, is limited by cost, readout complexity, practical geometry, and the transverse size of the cascade. For an incident hadron, the lost energy and f_{em} are highly variable from event to event. Until there is a more detailed knowledge of both the EM fraction and the invisible energy loss, the energy resolution of a hadron calorimeter will remain significantly worse than that of its EM counterpart. The efficiency e with which EM deposit is detected varies from event to event, but because of the large multiplicity in EM showers the variation is small. In contrast, because a variable fraction of the hadronic energy deposit is detectable, the efficiency h with which hadronic energy is detected is subject to considerably larger fluctuations. It thus makes sense to consider the ratio h/e as a stochastic variable. Most energy deposit is by very low-energy electrons and charged hadrons. Because so many generations are involved in a high-energy cascade, the hadron spectra in a given material are essentially independent of energy except for overall normalization. For this reason $\langle h/e \rangle$ is a robust concept, independently of hadron energy and species. For $\langle h/e \rangle \neq 1$(noncompensation), fluctuations in f_{em} significantly contribute to or even dominate the resolution. Since the f_{em} distribution has a high-energy tail, the calorimeter response is non-Gaussian with a high-energy tail if $f_{em} < 1$. Noncompensation thus seriously degrades resolution and produces a nonlinear response. It is clearly desirable to compensate the response, i.e., to design the calorimeter such that $f_{em} = 1$. This is possible only with a sampling calorimeter, where several variables can be chosen or tuned, as for example decreasing the EM sensitivity and increasing the hadronic sensitivity. However, given geometrical and cost constraints, the calorimeters used in modern collider detectors are not compensating.

Although the usually-dominant contribution of the f_{em} distribution to the resolution can be minimized by compensation or the use of other techniques, there remain significant contributions to the resolution, such as incomplete corrections for leakage, differences in light collection efficiency, electronics calibration, readout transducer shot noise (usually photoelectron statistics), electronic noise, sampling fluctuation and intrinisic fluctuation.

Except in a sampling calorimeter especially designed for the purpose, sampling and intrinsic resolution contributions cannot be separated. Sums and differences of the variances were used to separate sampling and intrinsic contributions. The fractional energy resolution can be represented by

$$\frac{\sigma}{E} = \frac{a_1(E)}{\sqrt{E}} \bigoplus \left|1 - \left\langle \frac{h}{e} \right\rangle\right| \left(\frac{E}{E_1}\right)^{1-l}$$

The coefficient a_1 is expected to have mild energy dependence.

After the first interaction of the incident hadron, the average longitudinal distribution rises to a smooth peak. The peak position increases slowly with energy. The distribution becomes nearly exponential after several interaction lengths. The transverse energy deposit is characterized by a central core dominated by EM cascades, together with a wide "skirt" produced by wide-angle hadronic interactions. While the average distributions might be useful in designing a calorimeter, they have little meaning for individual events, whose distributions are extremely variable because of the small number of particles involved early in the cascade.
Particle identification, primarily $e - \pi$ discrimination, is accomplished in most calorimeters by depth development. An EM shower is mostly contained in $15X_0$ while a hadronic shower takes about $4\lambda_I$. In high-A absorbers such as Pb, X_0/λ_I ∼0.03. In a fiber calorimeter, such as the RD52 dual-readout calorimeter, $e - \pi$ discrimination is achieved by differences in the Cerenkov and scintillation signals, lateral spread, and timing differences, ultimately achieving about 500:1 discrimination.

3.3 The LHCb calorimeters

As we already discussed in Chapter 1 the LHCb calorimeter system is composed of the SPD, PRS, ECAL and HCAL detectors. It selects transverse energy hadron, electron and photon candidates for the first trigger level (L0), which makes a decision 4 µs after the interaction. It provides the identification of electrons, photons and hadrons as well as the measurement of their energies and positions. The reconstruction with good accuracy of π^0 and prompt photons is essential for flavour tagging and for the study of b-meson decays and therefore is important for the physics program. The constraints resulting from these requirements define the general structure and the main characteristics of the calorimeter system and its associated electronics.
The most demanding identification is that of electrons. Within the bandwidth allocated to the electron trigger the electron Level 0 trigger is required to reject 99% of the inelastic pp interactions while providing an enrichment factor of at least 15 in b events. This is accomplished through the selection of electrons with large transverse energy E_T.
All detectors follow the same basic principle: scintillation light is transmitted to a Photo-Multiplier (PMT) by wavelength-shifting (WLS) fibres. The single fibres for the SPD/PRS cells are read out using multianode photomultiplier tubes (MAPMT), while the fibre bunches in the ECAL and HCAL modules require individual phototubes. In order to have a constant E_T scale the gain in the ECAL and HCAL phototubes is set in proportion to their distance from the beampipe. Since the light yield delivered by the HCAL module is a factor 30 less than that of the ECAL, the HCAL tubes operate at higher gain.

3.3.1 The pad/preshower detectors

The SPD/PRS detector consists of a 15 mm lead converter 2.5 X_0 thick, that is sandwiched between two almost identical planes of rectangular scintillator pads of high granularity with a total of 12032 detection channels. The SPD/PRS detector uses scintillator pad readout by WLS fibres that are coupled to MAPMT via clear plastic fibres. The choice of a 64 channel MAPMT allowed the design of a fast, multi-channel pad detector with an affordable cost per channel. The sensitive area of the detector is 7.6 m wide and 6.2 m high. Due to the projectivity requirements, all dimensions of the SPD plane are smaller than those of the PRS by $\sim$ 0.45%. The detector planes are divided vertically into two halves. Each can slide independently on horizontal rails to the left and right side in order to allow service and maintenance work. The distance along the beam axis between the centres of the PRS and the SPD scintillator planes is 56 mm. In order to achieve a one-to-one projective correspondence with the ECAL segmentation, each PRS and SPD plane is subdivided into inner (3072 cells), middle (3584 cells) and outer (5376 cells) sections with approximately 4×4, 6×6 and 12×12 cm^2 cell dimensions. The cells are packed in $\sim 48 \times 48$ cm^2 boxes (detector units) that are grouped into supermodules. Each supermodule has a width of $\simeq$ 96 cm, a height of $\simeq$ 7.7 m and consists of detector units that form 2 rows and 13 columns.

The square structure of a pad is cut out from a 15 mm thick scintillator plate, and the scintillator surface is polished to reach the necessary optical quality. In order to maximize the light collection efficiency, WLS fibres are coiled and placed into a ring groove that is milled in the body of the cell. The rectangular cross section of the groove is 4.1 mm deep and 1.1 mm wide. The groove contains 3.5 loops of WLS fibre. The number of loops was chosen to achieve an overall optimization of the light collection efficiency and the signal formation. Light produced by an ionizing particle in the scintillator is guided by the WLS fibre to the exit of the detector box. At this point optical connectors join the WLS fibres to long clear fibres. The two clear fibres connected to the two ends of the WLS fibre of a given pad are viewed by a single MAPMT pixel. The length of clear fibres varies from 0.7 to 3.5 m but all the fibres connected to a particular PMT have the same length in accordance with the front-end electronics specification. The clear fibre allows the transport of the scintillator light from the SPD/PRS planes over a few metres to the multi-anode PMT without significant attenuation.

The detector units are designed to be mounted on a supermodule support plate. All supermodules of the SPD/PRS planes have identical design. Each consists of 26 detector units mounted on a long aluminium strip in two columns. The photomultiplier tubes are located on both the top and bottom ends of the supermodule support outside the detector acceptance. The detector units are optically connected to the PMTs by bundles of 32 clear fibres, enclosed in a light-tight plastic tube, by means of a photo-tube coupler. The PMT is a (8-stage) R5900-M64 manufactured by Hamamatsu and has a bialkali photocatode segmented into 64 pixels of 2×2 mm^2 . The High Voltage (HV) is provided by a Cockroft-Walton voltage multiplier. The PMT gain is set to 10^4, which gives stable conditions of operation. Prior to the installation all the SPD and PRS modules were tested using a cosmic ray facility. Using a reference LED the average number of photoelectrons per Minimum Ionizing Particle (MIP) was measured to be 26, 28 and 21 for the PRS and SPD cells of the inner, middle and outer regions respectively.

The e/π separation performance of the PRS prototype was measured in the X7 test beam at the CERN SPRS with electrons and pions between 10 and 50 GeV/c momentum. The energy deposited in the PRS for 50 GeV/c electrons and pions is shown in Figure 3.6. The measurements show that with a threshold of 4 MIPs (about 100 ADC channels), pion rejection factors of 99.6%, 99.6% and 99.7% with electron retentions of 91%, 92% and 97% are achieved for 10, 20 and 50 GeV/c particle momentum, respectively.

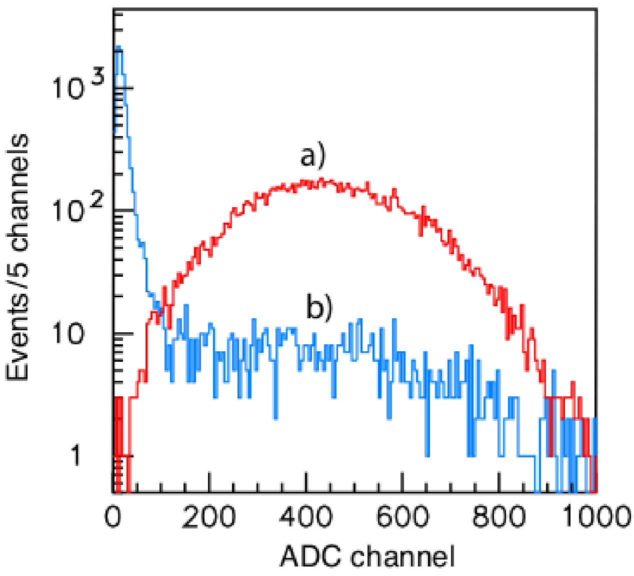

FIGURE 3.6: Energy deposition of (a) 50 GeV electrons and (b) pions in the PRS.

In order to separate photons and electrons at Level 0 of the ECAL trigger, the information from the SPD positioned in front of the lead absorber is used. Charged particles deposit energy in the scintillator material, while neutrals particles do not interact. However, several processes can lead to an energy deposit in the scintillator and result in the misidentification of photons. The dominant one is the photon conversion in the detector material before the SPD. Two other sources are interactions that produce charged particles inside the SPD, and backwards moving charged particles, "back splash", that are generated in the lead absorber or in the electromagnetic calorimeter. The latter two effects have been studied with the prototype in both a tagged photon beam and beams of electrons and pions of different energies, in the CERN X7 test beam area. The results were compared with simulation. The measurements for photon energies between 20 and 50 GeV show that the probability of photon misidentification due to interactions in the SPD scintillator is $(0.8 \pm 0.3)\%$, when applying a threshold of 0.7 MIPs. The probability to pass this threshold due to backward moving charged particles was measured to be $(0.9 \pm 0.6)\%$ and $(1.4 \pm 0.6)\%$ for 20 and 50 GeV photons, respectively. All these numbers are in very good agreement with Monte Carlo simulation study.

3.3.2 The electromagnetic calorimeter

The shashlik calorimeter technology refers to a sampling scintillator/lead structure read out by plastic WLS fibres. It has been chosen for the electromagnetic calorimeter not only by LHCb but by a number of other experiments. This decision was made taking into account modest energy resolution, fast time response, acceptable radiation resistance and reliability of the shashlik technology. Specific features of the LHCb shashlik ECAL are an improved uniformity and an advanced monitoring system. The design energy resolution $\sigma_E/E = 10\%/\sqrt{E} \bigoplus 1\%$ (E in GeV) results in a B mass resolution of 65 MeV/c^2 for the $B^+ \to K^{*+}\gamma$ penguin decay with a high-E_T photon and of 75 MeV/c^2 for $B \to \rho\pi$ decay with the π^0 mass resolution of $\sim 8MeV/c^2$.

Figure 3.7: (Left) Downstream view of the ECAL installed (but not completely closed) with the exception of some detector elements above the beam line.(Right) Outer, middle and inner type ECAL modules.

The electromagnetic calorimeter, shown in Figure 3.7 (left), is placed at 12.5 m from the interaction point. The outer dimensions of the ECAL match projectively those of the tracking system, $|\theta_x| < 300$ mrad and $\theta_y < 250$ mrad; the inner acceptance is mainly limited by $|\theta_{x,y}| > 25$ mrad around the beampipe due to the very high radiation dose level. The hit density is a steep function of the distance from the beampipe, and varies over the active calorimeter surface by two orders of magnitude. The calorimeter is therefore subdivided into inner, middle and outer sections with decreasing cell size, as shown in Figure 3.7(right). A module is built from alternating layers of 2 mm thick lead, 120 μm thick, reflecting 16 paper and 4 mm thick scintillator tiles. In depth, the sixty-six lead and scintillator layers form a 42 cm stack corresponding to 25 X_0, with a Moliere radius of 3.5 cm. The stack is wrapped with black paper, to ensure light tightness, pressed and fixed from the sides by the welding of 100 μm steel foil. The light from the scintillator tiles is absorbed, re-emitted and transported by 1.2 mm diameter WLS Kuraray Y-11(250)MSJ fibres traversing the entire module. The light is read out with Hamamatsu R7899-20 phototubes. The ECAL, the SPD and the PRS are segmented transversely into square cells of size 40.4 mm, 60.6 mm and 121.2 mm in the inner, middle and outer section, respectively. Readout cells of different sizes are defined by grouping together different sets of fibres onto one photomultiplier tube that is fixed to the back of the sampling structure. The lateral dimensions of the inner, middle and outer sections are ± 969.6, ± 1939.2 mm and ± 3878.4 mm in x and ± 727.2 mm, ± 1212.0 mm and ± 3151.2 mm in y, respectively. The standard deviations of the mean energy deposition by a MIP in the ECAL module was measured to be 7.4%, 4.4% and 6.0% for the outer, middle and inner sections respectively.
The performance of photon energy measurement with ECAL can be characterized by the

π^0 and η reconstruction. For high p_T di-photons ($p_T(\gamma) > 0.25$ GeV, $p_T(\gamma\gamma) > 1$ GeV) the effective mass resolution is $\approx 8MeV/c^2$ at π^0 and $\approx 20MeV/c^2$ at η. The $\gamma\gamma$ effective mass spectrum with π^0- and η-meson peaks is shown in Figure 3.8a, while the $\pi^+\pi^-\pi^0$ spectrum with η^0- and ω-meson peaks is shown in Figure 3.8b.

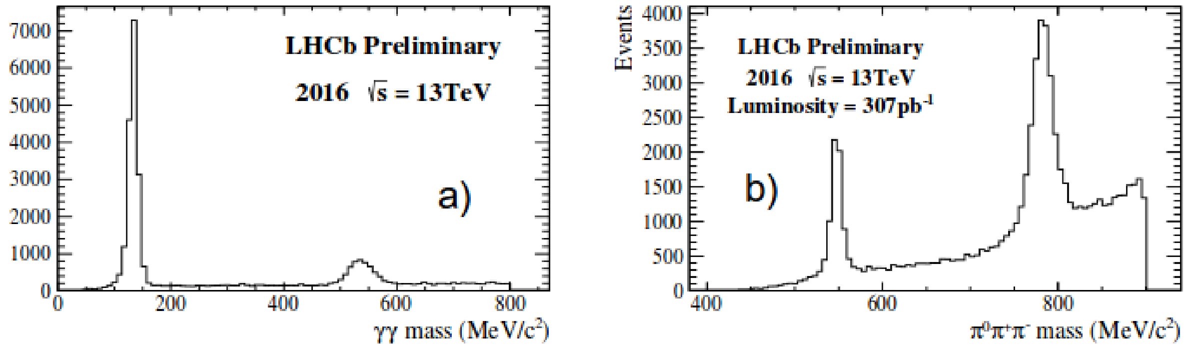

FIGURE 3.8: The effective mass spectra of $\gamma\gamma$ (a) and $\pi^+\pi^-\pi^0$ (b).

The global nonuniformity of response was measured to be negligible for all module types.
Depending on the type of module and test beam conditions the stochastic and constant terms were measured to be 8.5% < a < 9.5% and b ∼0.8%.

3.3.3 The hadron calorimeter

The LHCb hadron calorimeter is a sampling device made of iron and scintillating tiles as absorber and active material, respectively. The special feature of this sampling structure is the orientation of the scintillating tiles that run parallel to the beam axis. In the lateral direction tiles are interspersed with 1 cm of iron, whereas in the longitudinal direction the length of tiles and iron spacers correspond to the hadron interaction length in steel. The light in this structure is collected by WLS fibres running along the detector towards the back side where PMTs are housed. As shown in Figure 3.10, three scintillator tiles arranged in depth are in optical contact with 1.2 mm diameter fibre (Kuraray 20 Y-11(250)MSJ) that run along the tile edges. The total weight of the HCAL is about 500 tons.

The HCAL is segmented transversely into square cells of size 131.3 mm and 262.6 mm in the inner and outer section, respectively. Readout cells of different sizes are defined by grouping together different sets of fibres onto one photomultiplier tube that is fixed to the back of the sampling structure. The lateral dimensions of the inner and outer sections are ±2101 mm and ±4202 mm in x and ±1838 mm and ±3414 mm in y, respectively. The optics is designed such that the two different cell sizes can be realized with an absorber structure that is identical over the whole HCAL. The overall HCAL structure is built as a wall, positioned at a distance from the interaction point of z=13.33 m with dimensions of 8.4 m in height, 6.8 m in width and 1.65 m in depth.

The front view of the HCAL is shown in Figure 3.9. The absorber structure, shown in Figure 3.10, is made from laminated steel plates of six different dimensions that are glued together. Each module is composed of 216 identical periods of 20 mm thickness.

FIGURE 3.9: View from upstream of the HCAL detector installed behind the two retracted ECAL halves in the LHCb cavern.

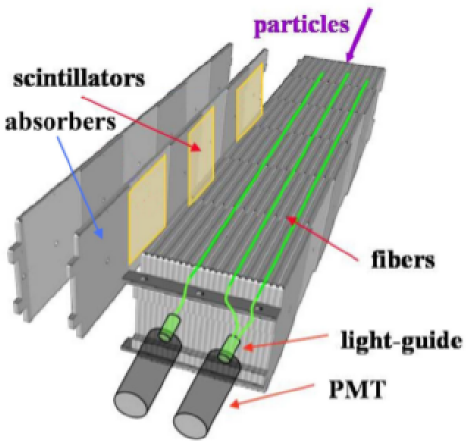

FIGURE 3.10: A schematic of the internal cell structure. The exploded view of two scintillator-absorber layers illustrates the elementary periodic structure of a HCAL module.

One period consists of two 6 mm thick master plates with a length of 1283 mm and a height of 260 mm that are glued in two layers to several 4 mm thick spacers of 256.5 mm in height and variable length. The space is filled with 3 mm scintillator.
The optics of the tile calorimeter consists of three components: the scintillating tile, the WLS fibre and a small square light mixer just in front of the photo-multiplier entrance window. The scintillating light propagates through the 3 mm thick tile to its edges where it is collected by 1.2 mm diameter WLS fibres. All fibres were measured to have a mirror reflectivity in the range of $(85 \pm 10)\%$. Each cell is read out by one photomultiplier tube that is attached to the rear mechanical structure of the module. The optical connection

between the fibre bundle and the photomultiplier is ensured by a 35 mm long light mixer of square shape.
The moderate requirements for the HCAL energy resolution allow the ratio between the active material volume and the passive material volume in the detector to be as low as 0.18. Furthermore, owing to the limited space available, the length of the HCAL has been chosen to be 5.6 λ_I. The upstream ECAL adds a further 1.2 λ_I. Beam-test measurements were compared in detail with results using different software packages for the simulation of the hadronic shower development. The energy response to 50 GeV pions is shown in Figure 3.11 for data and simulated events.

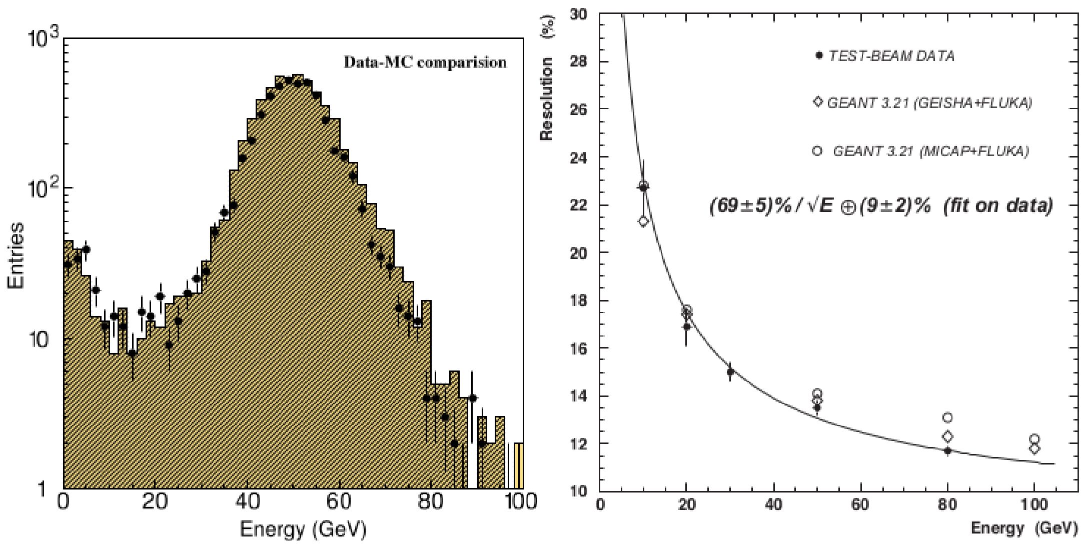

FIGURE 3.11: Left: energy response for 50 GeV pions from test-beam data (hatched) and from simulation (dots). Right: HCAL energy resolution, both for data and for simulation with three different hadronic simulation codes. The curve is a fit to the data.

The resolution extracted from a fit to the data at several energies is consistent with $\sigma_E/E = (69 \pm 5)\%/\sqrt{E} \bigoplus (9 \pm 2)\%$ (E in GeV) as shown in the right-hand plot of Figure 3.11. Another important feature of the HCAL is its signal timing properties. A precise signal shape measurement has been done with an electron beam of 30 GeV hitting layers of tiles at different depths. For this purpose the HCAL modules have been rotated by 90° and moved transversely with respect to beam line. Average pulse shapes of the detected signals are shown in Figure 3.12. The variation of the shape is due to light reflection from the mirror at the end of the fibre opposite to the PMT. For layer 1, for example, the direct and reflected light reach the PMTs simultaneously, but for layer 6, closest to the PMT, the direct light reaches the photocathode earlier than the reflected one by the propagation delay in the 1.2 m long WLS fibre.

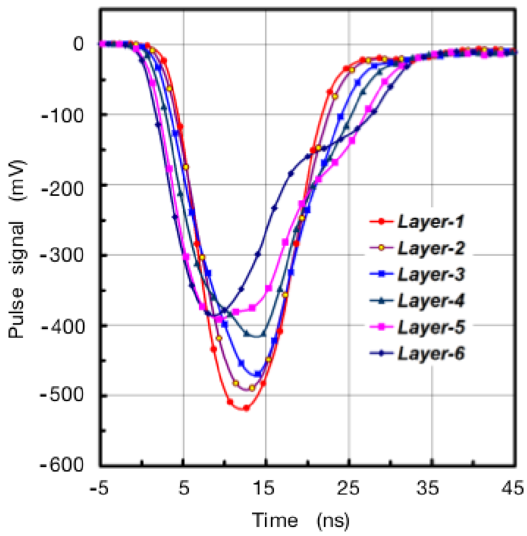

FIGURE 3.12: The average signal pulse shape of 30 GeV electrons in tile layers at different depths.

Chapter 4

Development of the fast simulation interface in the LHCb simulation framework

In this Chapter I introduce the software framework used at LHCb to simulate the physics events and I describe the changes that I developed to allow the replacement of the calorimeter full simulation with faster simulation options. The actual development of the calorimeter fast simulation is the subject of the next chapter.

4.1 LHCb simulation applications, reconstruction and selection

The LHCb software is composed of five main applications, each taking care of a specific task and each having *Gaudi* as the common framework (more details on *Gaudi* will be given in section 4.4): *Gauss* handles the physics event generation and the simulation of the particle interactions with the detector. *Boole* takes care of the simulation of the detector response. *Moore* runs the trigger selection on the stored data (simulated or real), while *Brunel* reconstructs the trigger selected events. Finally *DaVinci* is the physics analysis application, which is also run to apply a first filter on the data through a set of selections (stripping). Figure 4.1 shows the relations between these applications, the objects they need as input as well as the ones they create as output. In the following section I briefly describe *Gauss*, the application I had to work on to develop the fast simulation interface.

4.2 *Gauss*, the application for the event generation and particle transport

Gauss [23] is structured in two main independent phases, the event generation and the detector simulation, that can be run together or separately. Normally they are run in sequence as a single job since the first phase is much faster than the second one. A schematic view of the application phases is shown in Figure 4.2.

The first phase consists of the event generation of *pp* collisions and the decay of particles in the channels of interest for the LHCb physics program. The generation phase itself is structured as an algorithm that delegates specific tasks to dedicated tools ("physics generators"), like for example the number of collisions per bunch crossing, the setting of

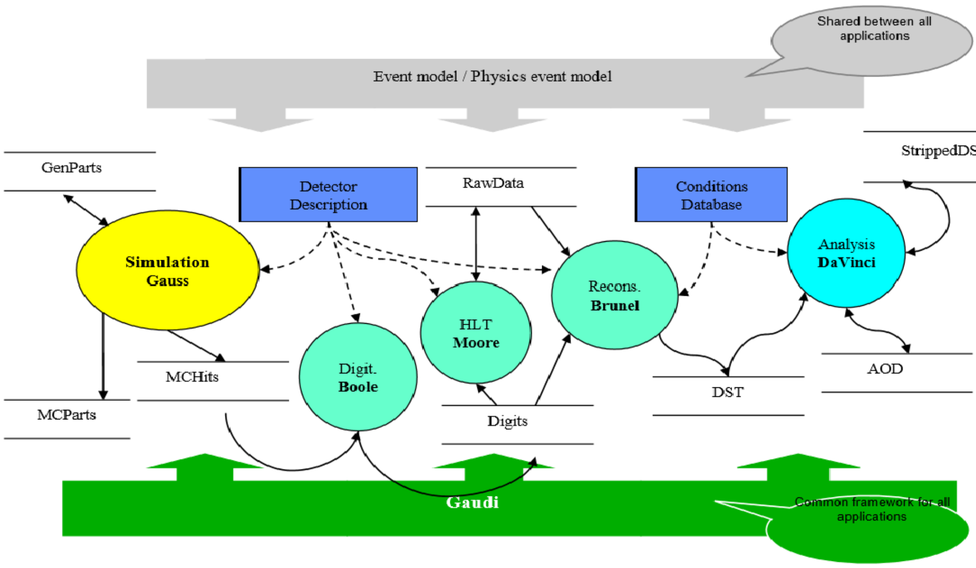

FIGURE 4.1: Schematic view of the LHCb simulation, reconstruction and analysis applications.

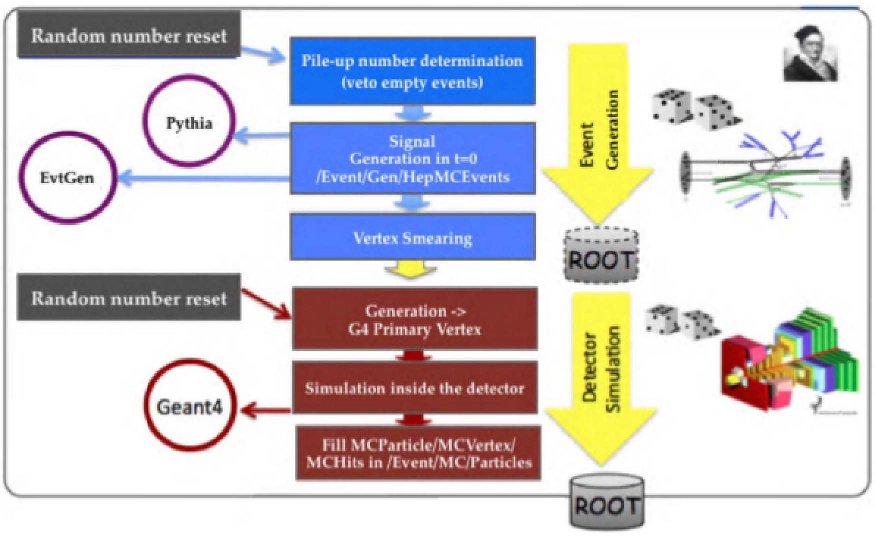

FIGURE 4.2: *Gauss* event processing sequence, divided in the generation phase and in the propagation of the generated particles.

the beam parameters for the collision, the smearing of the position of the collision, the generation of a given collision, the decay of particles after the hadronization and the selection of decay channels of interest. The set of generators integrated in *Gauss* via dedicated adaptors is increasing to match the widening of the physics program of the experiment. The majority of them are well established libraries, usually provided by groups of theorists, that are available to the high energy physics community at large (e.g. Pythia, EPOS) while a few others have been developed and are maintained by the experimental community (e.g. EvtGen). Different generators can be used in the same event (i.e. bunch crossing) for each of the concurrent collisions (pileup) and to handle the production and decay of particles.
The second phase of *Gauss* consists in the tracking of generated particles through the

LHCb detector. The simulation of the physics processes, which the particles undergo when they travel through the experimental setup, is currently delegated to the *Geant4* toolkit, which is briefly described in the next section. *Geant4* interacts with *Gauss* using a set of interfaces and encapsulated converters in a *Gaudi* specialised framework (GiGa). A sketch of the dependencies of the current version of *Gauss* from the underlying projects and libraries is given in Figure 4.3.

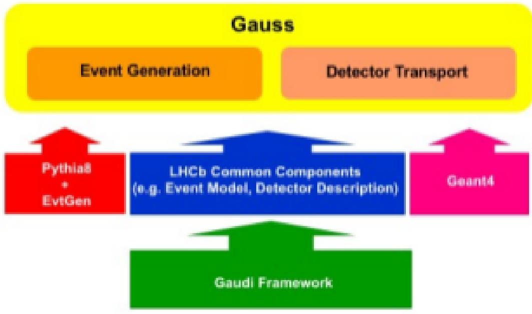

FIGURE 4.3: Dependencies on LHCb and external software for *Gauss*.

The output of *Gauss* is a set of collections of C++ objects called `MCHits`, which are used as input for the digitization phase handled by *Boole*.
Boole is the software which simulates the detector readout electronics. It produces an output identical in format to the real detector one.

4.2.1 The *Geant4* toolkit

The GEometry ANd Tracking (*Geant4*) toolkit [24] is a free platform developed by CERN and a worldwide collaboration of physicists and software engineers for the simulation of the passage of particles through matter which uses Monte Carlo methods and object oriented programming (C++). It is mainly employed in high energy physics, nuclear experiments, medical and space physics studies. It includes a complete range of functionality including tracking, geometry, physics models and detector hits. The offered physics processes cover a comprehensive range, including electromagnetic, hadronic and optical processes. *Geant4* can simulate a large set of long-lived particles over a wide particle's energy range starting, in some cases, from 250 eV and extending in others to the TeV energy scale. The toolkit offers the user the ability to create a geometrical model with a possibly large number of components of different shapes and materials, and to define "sensitive" elements that record information ("hits") needed to simulate detector responses (digitisation). *Geant4* simulations have been thoroughly verified by experimental data. The primary particles of the events can be derived from internal and external sources, like it is done in *Gauss* through the use of the generators. In *Geant4*, each particle trajectory is simulated in segments of variable length called steps which are represented by the `G4Step` class.
The user is able to choose from different approaches and implementations of physics processes to model the behaviour of particles, and can also modify or add to the set provided. The implementations of the physics processes must be defined in the base class `G4VProcess`.
In addition, objects of class `G4Track` represent the particles whose propagation in the

detector is being simulated. Each object holds information particular to each step of a particle, for example the current position, the time since the start of stepping, the identification of the geometrical volume where the particle is, etc.

4.3 Calorimeter simulation in *Gauss*

Geant4 simulates particles one at a time, and, as explained in section 4.2.1, it divides their trajectory in steps. In each step *Geant4* computes the deposited energy and the probability that secondary particles are created. In the LHCb calorimeter, if the step position falls into a cell volume, the "hit" information is added to a temporary object called `CaloHit`, containing the total energy released by every particle in the given cell. The `CaloHit` class is a collection of `CaloSubHit` objects, each one representing the total energy deposited by a single particle in the given cell.
At the end of each simulated event the `CaloSubHit` objects are converted into `MCCaloHits`, the specific `MCHit` objects for the calorimeter. The `MCCaloHit` object contains information on the activated calorimeter cell, the energy deposited in it and the corresponding time slot, in units of 25 ns, at which the energy was deposited. It also contains the information on the corresponding MCParticle. This object type is the input for the digitization (*Boole*) and, as such, is the final object we want to obtain from a fast simulation too.

4.4 The common framework for the LHCb applications, *Gaudi*

Gaudi [25] is an object oriented software architecture and framework that is used to facilitate the development of data processing applications for High Energy Physics experiments. It was designed and implemented before the start of the LHC and the LHCb experiment data taking, and it has been in production without major modification ever since. The aim of *Gaudi* is to provide a flexible software framework applicable by the entire LHCb collaboration for the simulation, reconstruction and analysis of *pp* interaction. In detail, it provides common generic tools, algorithms and interfaces underlying the specific ones of the LHCb applications such as *Gauss*. Although *Gaudi* has been developed in the context of the LHCb experiment, it has been designed to be easily customizable, so that it can be adapted to the different tasks and integrated with components from other frameworks.
An architecture consists of the specification of a number of components and their interaction with each other. A component is a "block" of software which has a specified interface(pure abstract class in C++) and functionality. The main components of the GAUDI software architecture can be seen in the object diagram shown in Figure 4.4.

The essence of the event data processing applications are the physics algorithms, which are encapsulated into a set of components that are called algorithms. The principle functionality of an algorithm is to take input data, manipulate it and produce output data. A complex algorithm can be implemented by using a set of simpler ones. At the top of the hierarchy of algorithms sits the application manager, which knows which algorithms to instantiate and when to call them. A complex algorithm schedules directly the execution of the sub-algorithms in the proper order to produce the desired results.
The data objects needed by the algorithms are organized in several transient data stores

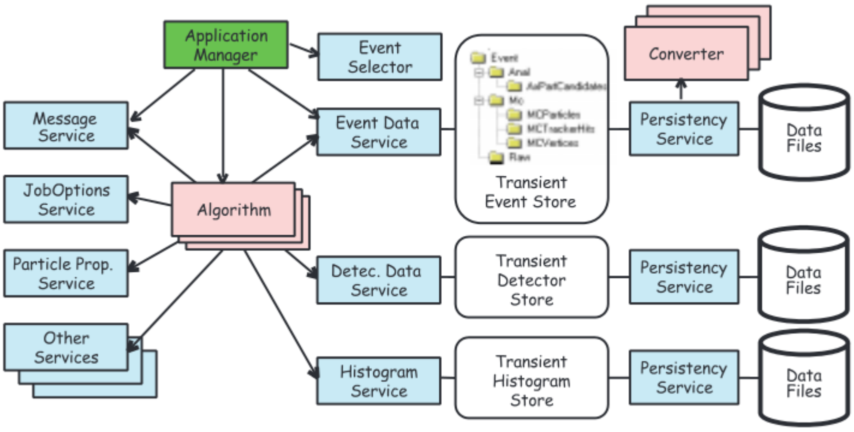

FIGURE 4.4: Object diagram of the *Gaudi* architecture.

(TES), depending on the nature of the data itself and its lifetime. The TES contains event data that are valid only for the time it takes to process one event. An algorithm can deposit some piece of data into the transient store, and these data can be picked up later by other algorithms for further processing without the need of information on how they were created. The transient data store also serves as an intermediate buffer for any type of data conversion to another representation of the data, in particular the conversion into persistent objects or graphical objects.
The organisation of the data within the transient data stores is "tree-like", similar to a Unix file system. This allows data items that are logically related, such as Monte Carlo "truth" information, to be structured and grouped at run-time. As in a directory structure, each node is the owner of everything below it and will delete all these items when it gets deleted.
Since all the LHCb applications have *Gaudi* as the common framework, the users have access to the algorithms and tools needed in physics analysis and in the software development. Moreover, the TES provides a common environment to store data objects used in different applications.

4.5 Development of the fast simulation interface in *Gauss*

In this section I will first describe the properties of the interface which calls the calorimeter fast simulation code, then I will explain how I implemented the interface through the creation of specific C++ classes in the LHCb simulation framework.
My implementation fast simulation interface allows to:

- choose the detector to which the fast simulation is applied.
- the particle species which have to be fast simulated.
- the dynamic properties (such as energy, transverse momentum, etc.) which a particle must own to trigger the fast simulation.

If the fast simulation interface is applied to the LHCb calorimeter, when a particle simulated by *Geant4* reaches the front face of the SPD, the calorimeter fast simulation code checks if the type and dynamic requirements are fulfilled. If so, the *Geant4* simulation of the particle stops and the fast simulation is called; otherwise, the particle keeps being simulated by *Geant4*.
Figure 4.5 shows a realistic example of the fast simulation interface applied to the LHCb calorimeter, whose envelope is represented by the `G4Region`. In this example the interaction of the photon with the calorimeter is fast simulated and the corresponding `G4Track` is stopped ("killed"), while the muons are propagated by *Geant4*, as their simulation in the calorimeter takes much less CPU-time ($\leq 2\%$ of the total calorimeter simulation time on average) than photons and electrons.

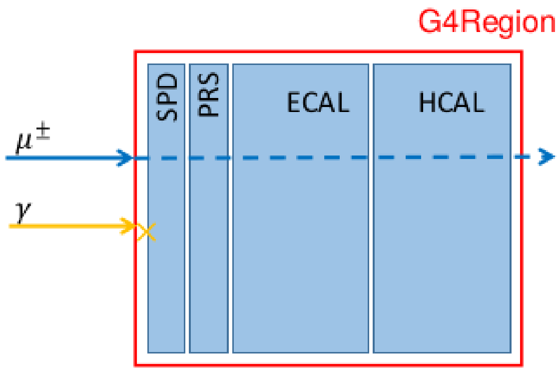

FIGURE 4.5: Scheme of an example application of the fast simulation interface to the LHCb calorimeter.

4.5.1 Implementation of the fast simulation interface

The actual implementation of the fast simulation interface is based on the *Geant4* parameterization framework which make use of the `G4Region` C++ class. Some needed *Geant4* base classes, described below, have been properly modified to be implemented in the *Gaudi* framework, and to make them fitted for the specific needs and to ensure flexibility of use. These *Geant4* C++ classes are:

- `G4LogicalVolume`; represents a detector element of a certain shape that can hold other volumes inside it and can have other attributes. It has also access to other general information, such as material and the behaviour of the sensitive detector. The `G4LogicalVolume` is responsible for retrieval of the physical and tracking attributes of the physical volume that it represents: shape of the element, material, magnetic field and, optionally, sensitive detectors regions.

- `G4Region`; this class represents an object composed of `G4LogicalVolumes` in the detector geometry setup, sharing properties associated to materials or production cuts which may affect or bias specific physics processes. It can also be associated to a `G4FastSimulationManager`, the object which manages all the fast simulation processes that the particles can undertake in the `G4Region`.

- `G4VFastSimulationModel`; this is the abstract class for the implementation of the actual fast simulation. The concrete class which applies the fast simulation must inherit from it. It has three virtual methods:

  1) `ModelTrigger(const G4FastTrack&)`. Returns `True` when the dynamics conditions to trigger the parameterisation are fulfilled. The `G4FastTrack` reference provides access to the current `G4Track`, gives simple access to envelope related features (`G4LogicalVolume`, `G4VSolid`, `G4AffineTransform` references between the global and the envelope local coordinates systems) and simple access to the position and momentum expressed in the region coordinate system.
  2) `IsApplicable(const G4ParticleDefinition&)`. Returns `True` when the model is applicable to the G4ParticleDefinition passed to this method. The `G4ParticleDefinition` provides all intrisic particle information (mass, charge, spin, name etc.) of the `G4Track` which *Geant4* is simulating. In the LHCb calorimeter fast simulation, `ModelTrigger` and `IsApplicable` are called when a particle reaches the front face of the SPD and then they select the particles to be fast-simulated.
  3) `DoIt(const G4FastTrack&, G4FastStep&)`. This method is called if both ModelTrigger and IsApplicable return `True` and it is the actual fast simulation. The `G4FastTrack` reference provides input information of the incident particle, while its final state after the fast simulation (for example the particle is killed or has a given final energy, position and momentum direction, etc.) can be returned through the `G4FastStep` reference. In the LHCb calorimeter fast simulation developed by me, the different algorithms which are used to fast-generate the "hits" for the fast-simulated particle and then kill the corresponding `G4Track` are implemented in this method. The creation of these algorithms is the subject of Chapter 6.

When simulating a step of a track, if the corresponding position is in a `G4LogicalVolume` which is part of a `G4Region`, *Geant4* checks if the `G4Region` has a `G4VFastSimulationModel` associated to it, and if so, this `G4VFastSimulationModel` is called before the standard physics processes are applied. Then, if the corresponding `IsApplicable` and `ModelTrigger` methods return `True`, the fast simulation is called through `DoIt` and subsequently the `G4Track` is killed. Otherwise, *Geant4* takes care of the `G4Track` simulation.

4.5.2 *Gauss* implementation

The implementation of the fast simulation interface in the *Gaudi* framework required some steps:

- the creation of the `G4Region` by a vector `G4LogicalVolume` names.
- the creation of the *Gauss* specific class derived from `G4VFastSimulationModel`.
- the creation of the specific calorimeter fast simulation, also called fast simulation model.
- the convertion of the fast-generated `CaloSubHit` into `MCCaloHits`.

I completed the first and last goals through the use of *Gaudi* based tools. The `GiGaFastRegionTool` builds the `G4Region` during the simulation setup, while also initializing the associated `G4VFastSimulationModel`. In more detail, it takes as input a vector of `G4LogicalVolume` names from which the calorimeter `G4Region` is built. Then the fast simulation is initialized and associated to the `G4Region`.
The convertion of the fast-generated `CaloSubHit` into `MCCaloHits` is executed at the end of each simulated event by the `GetFastCaloHitAlg` class. This class takes the hit collections created by the fast simulation, converts them into `MCCaloHits` which finally are it added to the ones generated by the standard *Geant4* simulation. The `MCCaloHits` created from the fast generated hits are indistiguishable from the standard ones, as they serves as input for the digitization phase.
Finally, the implementation of a specific calorimeter fast simulation required the creation of a more generic virtual class derived from `G4VFastSimulationModel` and inserted into the *Gaudi* framework. To achieve this, I had to define some interfaces and methods in *Gauss*, which are needed to correctly initialize a fast simulation model and to allow it to call necessary *Gaudi* tools. Each specific fast simulation model needs to inherit from this new class, which I have called `GiGaFastSimulationModel`. The model must also create objects of the `CaloSubHit` type, which are the input for the `GetFastCaloHitAlg` class. The creation of two fast simulations models is the subject of Chapter 5.
After the implementation of the interface in *Gauss*, the fast simulation interface has been tested to verify its proper functioning and to estimate the lower speed-up percentage limit achievable. To do this, a test simulation have been performed using the interface to stop all the particles but the muons as they enter the calorimeter without generating hits. The resulting simulation time is then confronted with the one of a standard *Geant4* simulation to obtain the lower speed-up percentage limit. The muons are always simulated as their impact on the simulation computing time is negligible in the calorimeter.
The results showed that the lower speed-up percentage limit obtainable with the fast simulation interface is 41.5%, as it could be expected from Figure 2.7 shown in Chapter 2. This result, together with the absence of simulated particles in the calorimeter with the exception of the muons, proved the fast simulation interface works as intended.

Chapter 5

Development of the calorimeter fast simulation

Once the fast simulation interface is implemented, the actual calorimeter fast simulation must be created and tested. The first step is the identification of the most time-consuming particles to simulate in the calorimeter and the study of their properties. Then the calorimeter fast simulation can be developed, bearing in mind that the procedure must be reproducible for all particles of interest. In this Chapter I present the study of the nature of the particles reaching the calorimeter and the development of two fast hit generator, suitable for complementary energy ranges of the particles.

5.1 Nature and energy distribution of particles reaching the calorimeter

Preliminary studies have been performed to characterize the properties of the particles reaching the calorimeter. The particle types of tracks which reach the SPD front face and their energy spectrum have been obtained for minimum bias simulated events through the use of some specific tools. In total, about 400 particles reach the calorimeter for every collision event. The distribution of particle species is summarised in Table 5.1.

TABLE 5.1: Population at the calorimeter entrance in minimum bias events.

Particle	Fraction (%)
γ	69.6
$e^{\pm}$	14.9
$\pi^{\pm}$	6.5
n	5.4
$p/\bar{p}$	1.9
$\mu^{\pm}$	0.6
$K^{\pm}$	0.4

The photons are the most abundant particles and for this reason they are the first candidates for the development of a fast simulation of the calorimeter. The typical energy spectrum is very soft, as it can be seen in Table 5.2 where the fraction of photons below a given threshold is shown.

For instance 55% of photons have $E < 16$ MeV. When hitting the calorimeter, a significant fraction ($\approx 90\%$) of these low-energy photons produce a visible signal only in

TABLE 5.2: Fraction of photons at the calorimeter entrance with energy below the given value in minimum bias events.

Energy (MeV)	Fraction (%)
10000	99.7
1000	92.9
100	75.9
32	64.4
16	55.2
8	44.1
4	16.0

the single calorimetric tower they have impacted upon. This large number of low energy photons led to the development of a simple single-hit engine, described in the next section, which also served as a overall test of the correct operation of the complete software chain before the creation of a more complex one.
However, typical photons generated from b and c decays have much larger energy than the ones generated from minimum bias events. To determine the energy range of these photons, $D^+ \to \eta' \pi^+$ decays, with $\eta' \to \pi^+\pi^-\gamma$, have been generated using the PYTHIA8 physics generator software. Figure 5.1 shows the resulting distributions of the photon's energy E and transverse momentum p_T.

Therefore, it can be concluded that the energy range which we need to cover in a fast simulation model extends from a few MeV up to O(100) GeV.

5.2 The single-hit engine

In this model, the total energy released by the particle in a given subdetector (SPD, PRS, ECAL, HCAL) is deposited in a single calorimeter cell hit located at the expected entrance point of the particle in that subdetector. The position of this point is obtained from the intersection of the linear extrapolation of the particle trajectory with the corresponding subdetector front plane.
When a photon enters the calorimeter[1], the total energy deposited by the photon E_{dep}, the number of hits N and the probability that the photon creates at least one hit are function of the photon energy E and the incident angle θ, defined as the angle between the particle's trajectory and the axis perpendicular to SPD face. Two dimensional histograms have been used to parameterize these dependencies. In particular, these *maps* plot the mean ($\mu_{E_{frac}}$) and standard deviation ($\sigma_{E_{frac}}$) of the fractionary deposited energy $E_{frac} = E_{dep}/E$ and also the mean total number of hits (μ_N) for each subdetector as function of E and θ. These *maps* are accessed at simulation run time to obtain N and E_{dep} with a MC method explained below and then the fast hits are generated from these values.
Geant4 simulations of single photons have been performed to obtain the parameters plotted by the *maps*. In this type of simulation, a single photon is generated in a given position

[1]During the simulation of a particle `G4Track`, when a `G4Step` position is for the first time inside the calorimeter's `G4Region` volume, the particle is said to be entering the calorimeter.

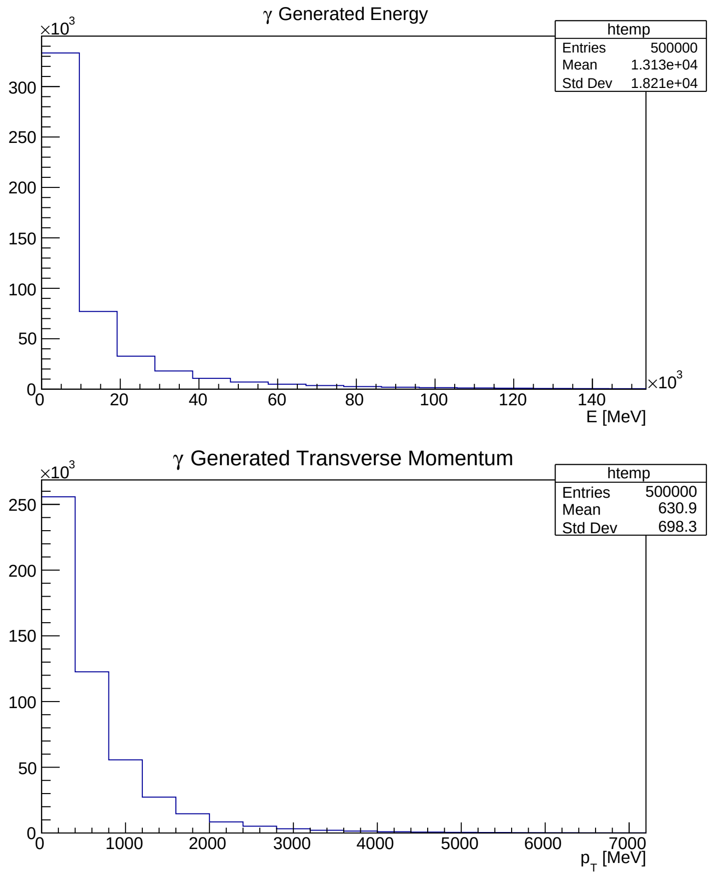

FIGURE 5.1: Generated E, p_T distributions for photons of $D^+ \to \eta' \pi^+$ decays, with $\eta' \to \pi^+ \pi^- \gamma$.

of the SPD face with different values of E and θ. As the low energy photons usually don't come from the primary vertex, the generated θ covers the range from 0 rad to $\pi/2$ rad. The E and θ ranges have been divided in a number of intervals and, for each of them, the distributions of the photon's E_{frac} and N distributions have been obtained. The dependency of $\mu_{E_{frac}}$ and $\sigma_{E_{frac}}$ parameters on E and θ has been determined by fitting the total photon's released energy with a Gaussian distribution for each E, θ interval. Similarly, the N distributions has been fitted with Poisson distribution to obtain the μ_N dependency. Examples of these fits for photon simulated with E = 428 MeV and $\theta = 0.42$ rad are shown in Figure 5.2. The parameters obtained with this procedure have then been used to build the *maps* whose E,θ binning and range are consequently determined by the number and length of the intervals used in the fitting procedure. The resulting binning of the *maps* is: 20 bins of logarithmically variable width for E in the range [0, 8]GeV, and 20 bins for θ in the range [0, $\pi/2$]rad. Figure 5.3 shows an example of such *maps*. In the $\mu_{E_{frac}}$ *map*(top-left), white colored bins have z-values lower than the minimum z value of the scale. Low values of $\mu_{E_{frac}}$ ($\mu_{E_{frac}}$ <0) can result from the Gaussian fit for E,θ bins which have a mean $N \leq 1$ (that means low statistic) and a E_{frac} distribution similar to the right tail of a Gaussian. Therefore the fit returns a mean $\mu_{E_{frac}}$ <0.

During a simulation, when a photon with a given E and θ enters the calorimeter, the fast simulation code determines if this photon has the appropriate E, θ to be fast-simulated with the single-hit engine. If so, it identifies the cells in each subdetectors whose

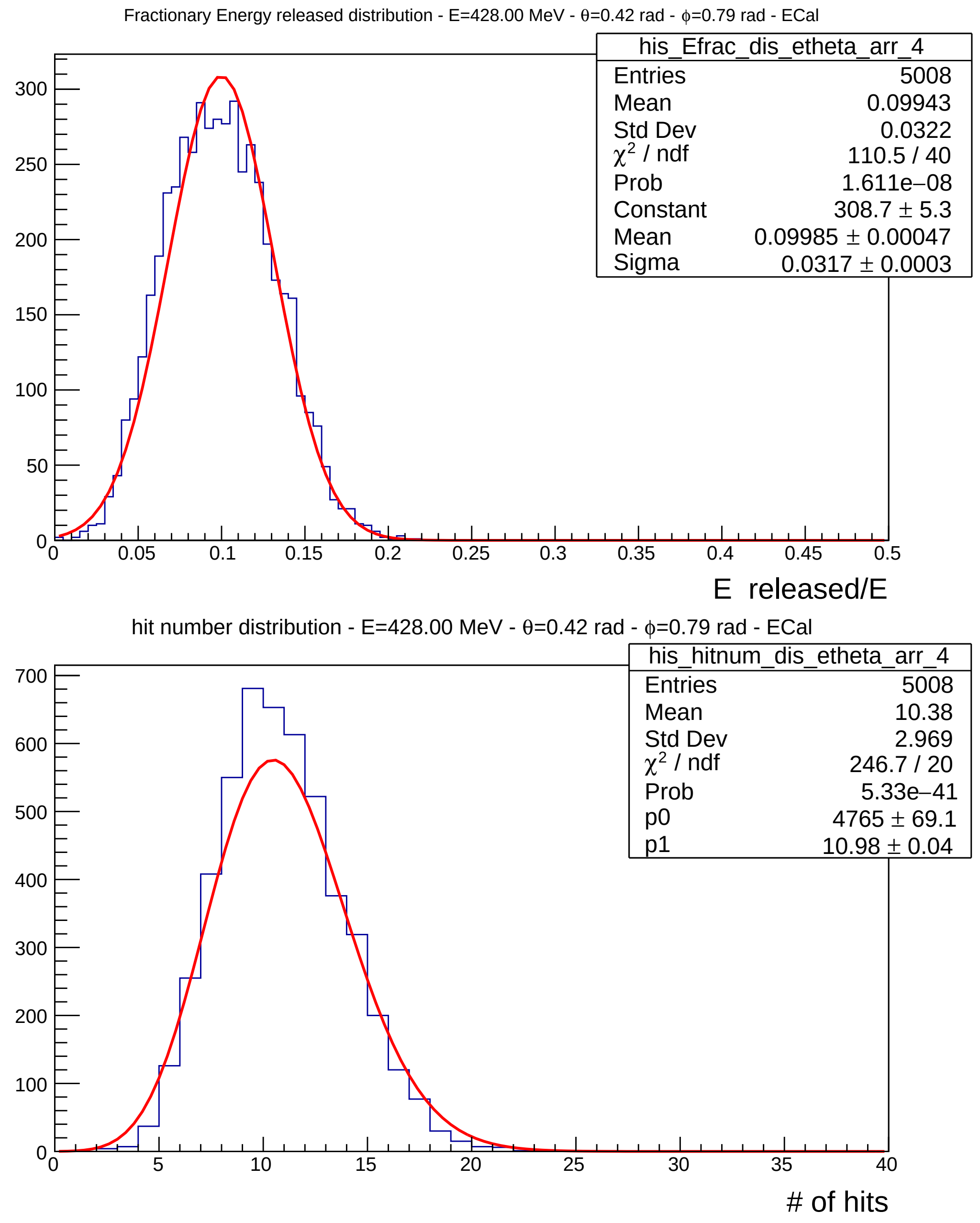

FIGURE 5.2: Examples of fractionary deposited energy distribution fitted with a Gaussian pdf(top), and of the total number of hits distribution fitted with a Poisson pdf(bottom).

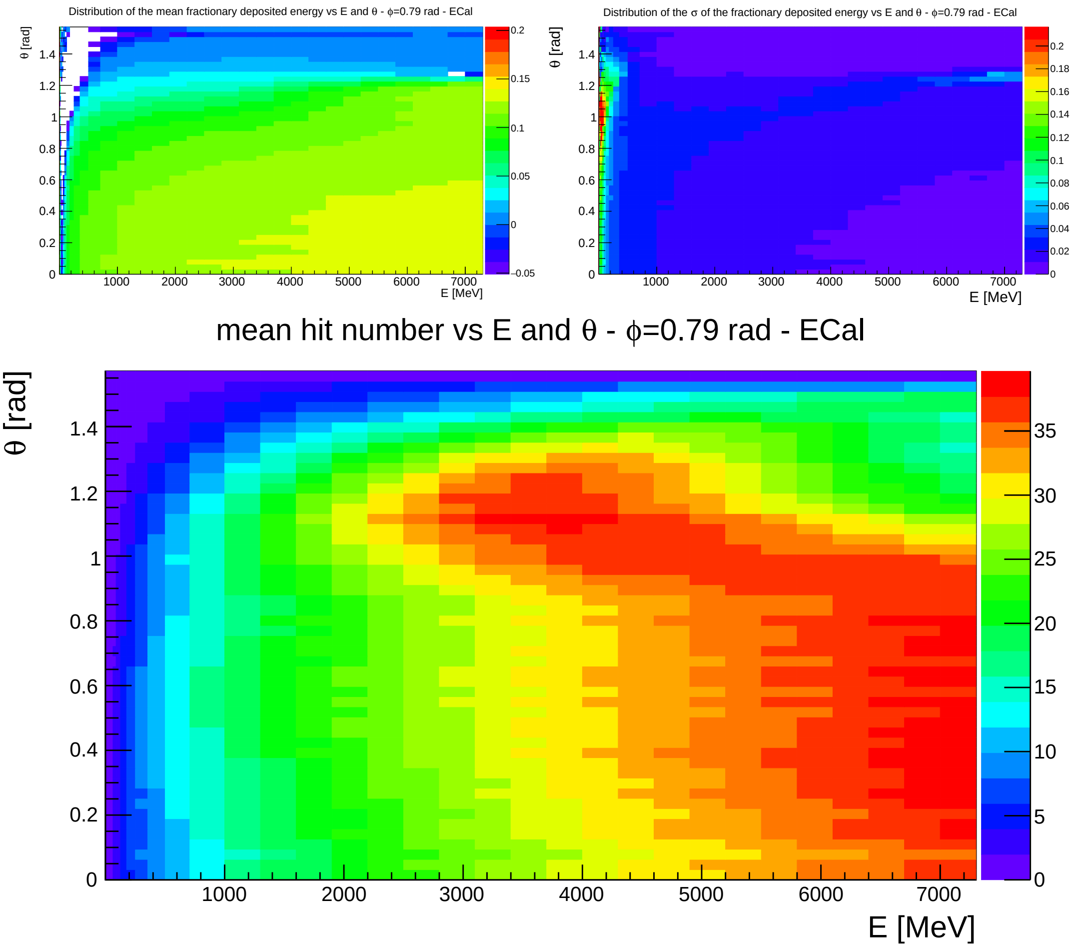

FIGURE 5.3: 2D *maps* of $\mu_{E_{frac}}$(top-left), $\sigma_{E_{frac}}$(top-right) and μ_N (bottom) as a function of the incident photon E and θ for the ECAL. White colored bins have z-values lower than the minimum z value of the scale.

position corresponds to the entrance point of the photon (otherwise it is propagated by *Geant4*). Then for each of these cells it generates a random number N of hits from a Poisson distribution with mean μ_N extracted from the correponding map. If $N \geq 1$ the hit is created and, in this case, the fractionary deposited energy E_{frac} is randomly generated from a Gaussian distribution with mean $\mu_{E_{frac}}$ and width equal to $\sigma_{E_{frac}}$. The total deposited energy is then obtained from $E_{dep} = E_{frac}E$ and the information added to the hit.
Test simulations of $D^+ \to \eta'\pi^+$ decays, with $\eta' \to \pi^+\pi^-\gamma$ have been performed to evaluate the physics performance. The results are described in Chapter 6. As a first iteration of the model, the time associated to the energy releases have been fixed as if the fast-simulated photons came from the primary vertex to allow this signal reconstruction test.

5.3 Development of the *point library*

The single-hit model well describes the interaction of low energy photons with the calorimeter, but is bound to fail in describing higher energy photons that most often produce signal in multiple cells. While this might not be a real problem for isolated energy deposits, it may become a significant limiting factor in more crowded events, where the correct description of the spread of the calorimetric signals over multiple cells might significantly affect the results of the event reconstruction algorithms, causing a loss of reliability of the simulations' results.
For this reason, we also designed a separate algorithm for dealing with distributed energy deposits. Due to the large increase of dimensionality of the problem and the strength of internal correlation of the variables involved in the electromagnetic cascade development (see Chapter 3), an analytical approach is very difficult in this case, and we prefer a template-based approach ("shower library").

5.3.1 The shower library: definition and limitations

The shower library concept has been taken as a basis to build a more precise fast simulation, described in the next section, for the LHCb calorimeter. In the standard approach of the shower library, the detector response is simulated using a collection of stored hits for different particle types. Each stored collection correponds to a set of input variables, usually E, θ, ϕ and x, y position of the particle's entrance point in the calorimeter. This approach requires the phase space of these variables to be divided in a grid of nodes, each node representing a set of E, θ, ϕ (the azimuthal angle) and x,y position values. Each node is associated with a set of N_{sim} stored hit collections. The stored hit collections are created from single particle simulations generated at the calorimeter face with the E, θ, ϕ and x,y position values of the corresponding node.
During a simulation, when a particle to be fast simulated enters the calorimeter, it is stopped, then a hit collection is randomly selected from the N_{sim} collections of the node "closest" to the particle's E, θ, ϕ and x,y position values in the variable phase space and finally this hit collection is substituted. N_{sim} has to be large enough to ensure statistical variety to the fast simulation of the particle.
The precision of the simulation increases with the number of the library nodes. However, the size of the library increases with the number of the library variables (five in our example), the number of nodes and N_{sim}, and therefore it could exceed the computational

constraints of the enviroments where the simulation jobs are expected to run. The goal is to keep the size of the library within few 100 MB. To avoid exceeding this size limit while maintaining an acceptable precision level, the number of variables should be reduced by exploiting appropriate symmetries. Finally, to achive a good compromise between simulation precision and library size, the number nodes and N_{sim} should be properly adjusted.

5.3.2 The *point library*

A new technique based on the concept of shower library has been developed to solve the library size under control while maintaining a good simulation precision. This technique has been called *point library*. In the shower libraries, the hit position is usually identified with the position of the cell activated by the energy released in it. In a *point library*, instead, the hit position matches with the position of small sub-cell region of a given subdetector (for instance, 25 sub-cell regions for each cell of the inner section). This procedure increases the information granularity of the *point library* and, as a consequence, the simulation precision. However the information stored in the *point library* is quite larger than that stored in a standard shower library, causing a significant increase in the file size. To mitigate this increase in the library size, it is necessary to reduce the number of the library variables by exploiting possible symmetries of the system, such as the rotation around the z-axis and the translation over the x-y plane. If these symmetries are verified, the *point library* can be build using only the E and θ variables, leading to a significant reduction of the library size. Moreover, hits in the same cell and under a given energy threshold (E_{thr}) are merged locally, their energies summed and the position equal to the barycenter defined as $x(y)_{sub} = \frac{\sum E_i x(y)_i}{\sum E_i}$, with $x(y)_i$ and E_i position and energy of the i-th hit, respectively. The position of the hit in this case is identified with the center of the relative subcell. This procedure further reduce the library size. To be noted, the greater the threshold, the lesser the number of hits stored and the smaller the library file size, at the cost of the simulation precision. Figure 5.4 (top) shows a visual representation of the shower hits in the ECAL x-y plane, which is divided in cells. Figure 5.4 (bottom) shows the new hits distribution after the merging of the hits under threshold during the library creation procedure.

The rotation around the z-axis simmetry, if verified, avoids using the ϕ variable in the library, which leads to a significant reduction of the library's size. Therefore, I need to check if the rotation can be exploited by verifying that the calorimeter response is symmetrical about ϕ.
For this purpose, the distributions of the cluster centroid position $X(Y)_c$ and of the cluster width σ have been compared for photons with generated $\phi = 0$ rad and $\phi = \pi/2$ rad. Test simulations of single photons generated at the SPD face with $E = 125$ MeV, $\theta = [0.31, 0.62]$ rad and $\phi = [0, \pi/4, \pi/2, 3\pi/4, \pi, 5\pi/4, 3\pi/2]$ rad. The photon's vertex position (X_T, Y_T) is generated at the SPD z position and in a x,y range corresponding to a inner section cell's area (646.4 mm$\leq X_T \leq$686.8 mm and 484.8 mm$\leq Y_T \leq$525.2 mm, while the cell center position is $X_{cell3} = 666.6$ mm, $Y_{cell3} = 505.0$ mm). If the rotation symmetry is good enough, I expect a similar behaviour for the same θ and for couples of ϕ angles relative to the exchanges x↔y, x↔-x and y↔-y.

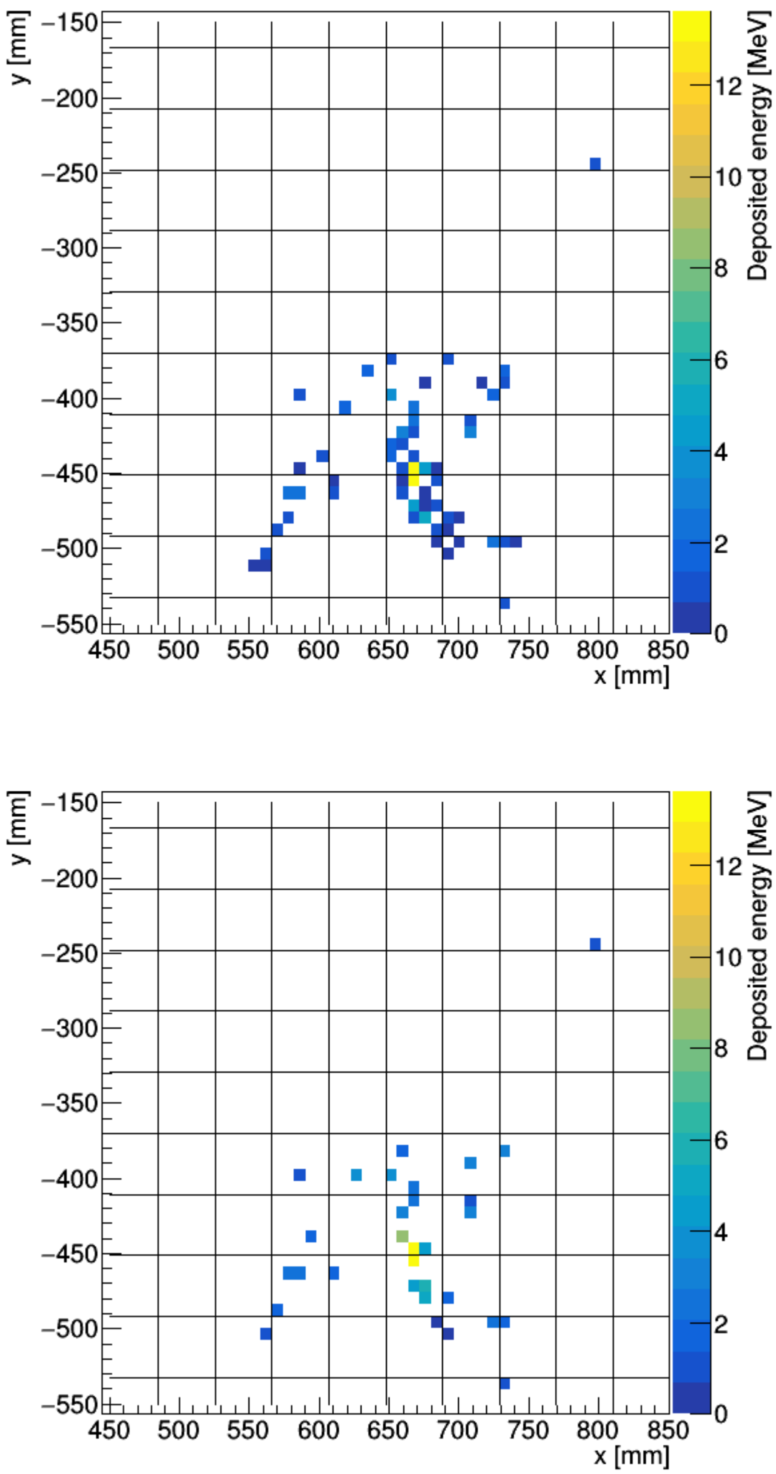

FIGURE 5.4: Visual example of subcells and of hits distribution before (top) and after (bottom) the merging. The black lines represent the division between ECAL cells, while the colored dots are the subcell hits. The hits energy is on the z axis.

The cluster centroid position and the cluster width parameters are defined as:

$$X(Y)_c = \frac{\sum E_i x(y)_i}{\sum E_i}, \qquad \sigma^2_{X(Y)} = \frac{(\sum E_i (x(y)_i - X(Y)_c)^2)}{\sum E_i}, \tag{5.1}$$

where $x(y)_i$ and E_i position and energy of the i-th hit, respectively. The position of the hit in this case is identified with the center of the activated cell.

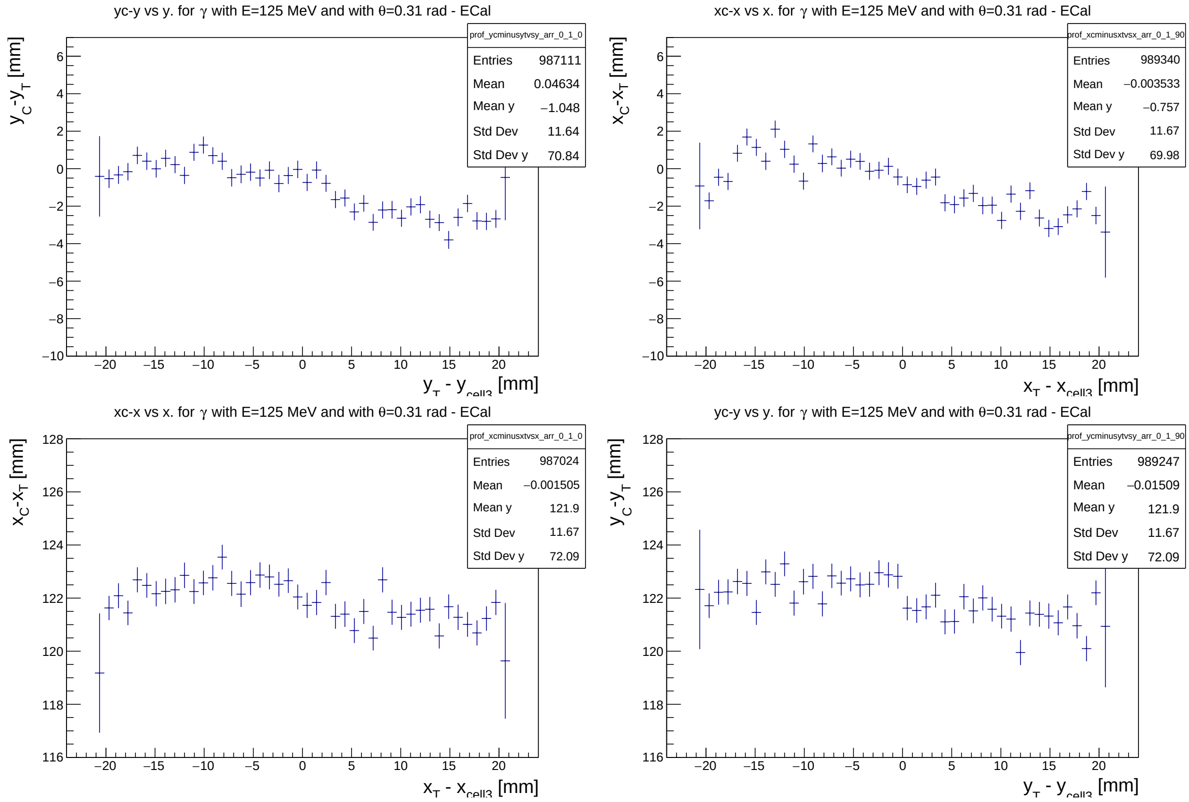

FIGURE 5.5: Comparison of the dependency of $X(Y)_c - X(Y)_T$ on $X(Y)_T$ in the ECAL for particles generated with E=125 MeV, $\theta = 0.31$ rad and $\phi = 0$ rad(left plots), $\phi = \pi/2$ rad (right plots). The top-left plot shows the $Y_c - Y_T$ distribution to be compared with the top-right plot which shows the $X_c - X_T$ distribution. The bottom-left plot shows the $X_c - X_T$ distribution to be compared with the bottom-right plot which shows the $Y_c - Y_T$ distribution.

Some example results of the comparisons between simulations at $\phi = 0$ rad and $\phi = \pi/2$ rad (x↔y exchange) are shown in Figure 5.5 and in Figure 5.6. It can be concluded that the x-y simmetry is approximated quite well. Therefore, the rotation of the shower can be applied and the ϕ variable removed from the library.

Another symmetry to test is the one under a translation over the x-y plane. If this symmetry were true, the dependency of the *point library* on x and y could be removed with a consequent reduction of the library size. In this case, the only remaining variables will be E and θ, and it will be possible to build the library using photons generated with the same vertex position outside the SPD face and, at simulation run time, translate the hit collections in the x-y plane according to the actual position of the photon's entrance point in the calorimeter. To check this symmetry validity, I tested the detector response by looking at the cluster barycenter position for photons generated at different points at the calorimeter front face. In detail, the dependency of $X(Y)_c - X(Y)_T$ on $X(Y)_T$ has been obtained from simulations of single photon simulations.
The photons have been simulated with E= 125 MeV and θ = [0, 0.31, 0.63] rad and

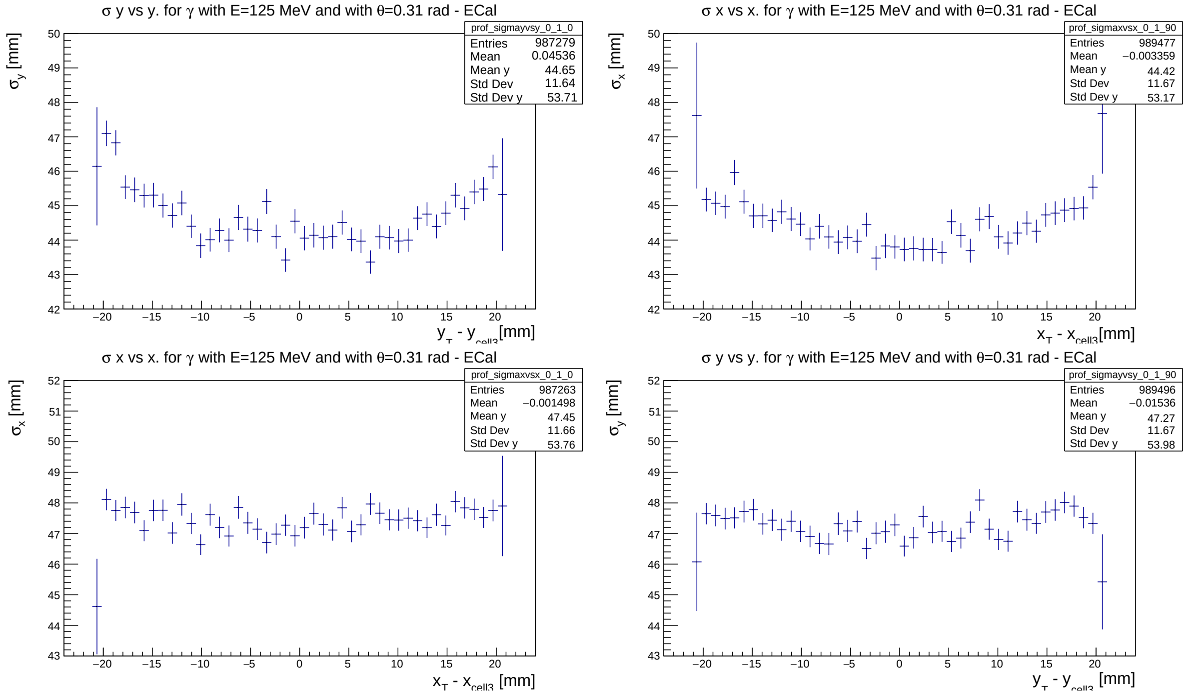

FIGURE 5.6: Comparison of the dependency of $\sigma_{X(Y)}$ on $X(Y)_T - X(Y)_{cell3}$ in the ECAL for particles generated with E=125 MeV, $\theta = 0.31$ rad and $\phi = 0$ rad (left plots), $\phi = \pi/2$ rad (right plots). The top-left plot shows the σ_Y distribution to be compared with the top-right plot which shows the σ_X distribution. The bottom-left plot shows the σ_X distribution to be compared with the bottom-right plot which shows the σ_Y distribution.

$\phi = \pi/2$ rad. $X(Y)_T$ have been generated in ranges corresponding to four different inner section cell's positions:

- cell1: 323.2 mm $\leq X_T \leq$ 363.6 mm ; 484.8 mm$\leq Y_T \leq$525.2 mm
- cell2: 484.8 mm $\leq X_T \leq$ 525.2 mm ; 484.8 mm$\leq Y_T \leq$525.2 mm
- cell3: 646.4 mm $\leq X_T \leq$ 686.8 mm ; 484.8 mm$\leq Y_T \leq$525.2 mm
- cell4: 808.0 mm $\leq X_T \leq$ 848.4 mm ; 484.8 mm$\leq Y_T \leq$525.2 mm

If $X(Y)_c$ is independent on $X(Y)_T$ for every cell, the translation symmetry on the x-y plane can be assumed.
Figure 5.7 and Figure 5.8 show the dependency of $X_c - X_T$ on X_T for the four cells and for photons with $\theta = 0$, 0.63 rad, respectively. The mean $X_c - X_T$ values for the four cells differ by about 1 mm for every θ value, to compare with the smallest calorimeter cell side length of 40.4 mm in the inner section. The same can be said for the response in the same cell, as the maximum difference between $X_c - X_T$ values is of about 1 mm. So, to first approximation, $X(Y)_c - X(Y)_T$ does not depend on $X(Y)_T$ and the translation symmetry on the x-y plane is assumed.

Finally, after some tests, it has been decided to create 25 sub-cell regions for each cell of the inner section, while N_{sim} has been decided to be 20. The E, θ phace space has been divided in 21 nodes in E from 1 to 100 GeV, and in 21 nodes from 0 to 0.436 rad. E_{thr}

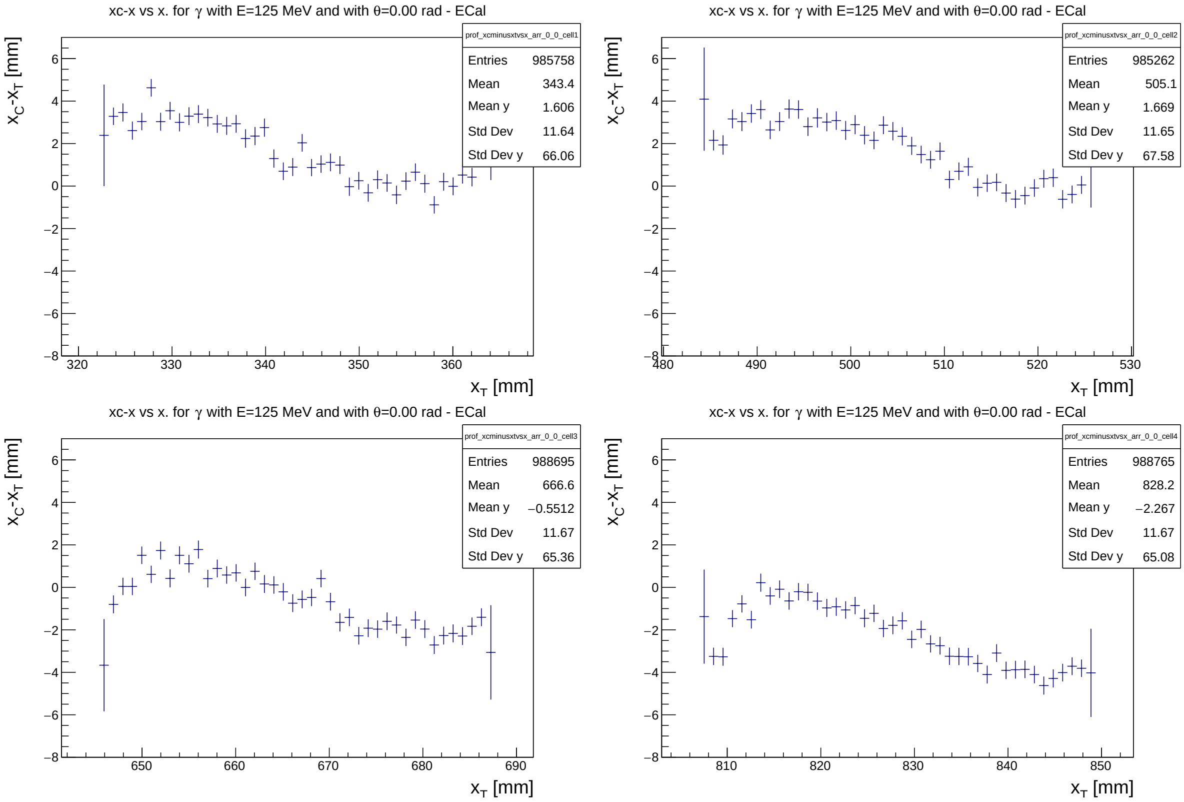

FIGURE 5.7: Comparison of the dependency of $X_c - X_T$ on X_T in the ECAL for particles generated with E=125 MeV, $\theta = 0.0$ rad and $\phi = \pi/2$ rad. X_T is generated in ranges corresponding to cell1(top-left), cell2(top-right), cell3(bottom-left) and cell4(bottom-right).

value has been set to 4 MeV, while the simulated ϕ is equal to $\pi/2$ rad.
During a simulation setup, the library file is loaded. When a particle is fast-simulated, a shower is randomly selected as explained above and then the shower hits positions are translated in the x-y plane to match the actual calorimeter entering point of the incident particle, and finally rotated around the z-axis to obtain the same ϕ angle of the incident particle. The resulting hit distribution is then transformed in `CaloHits` through the use of specific classes which translate the hit position in the actual cell position, which is needed to create the `CaloHit`. As a first iteration of the model, the time slot of the energy releases have been fixed as if the photon came from the primary vertex.

Figure 5.9 shows a visual representation of the hit rotation when a particle is fast-simulated(top) and of the hits conversion in cell hits(bottom). Single photons simulations have been performed to evaluate the agreement of the *point library* model with the standard simulation. The results are described in Chapter 6.

5.3.3 Next steps of development

To further improve the agreement between the output of the rotated *point library* and of the full simulation, it is necessary to implement some corrections to the position x_i,y_i

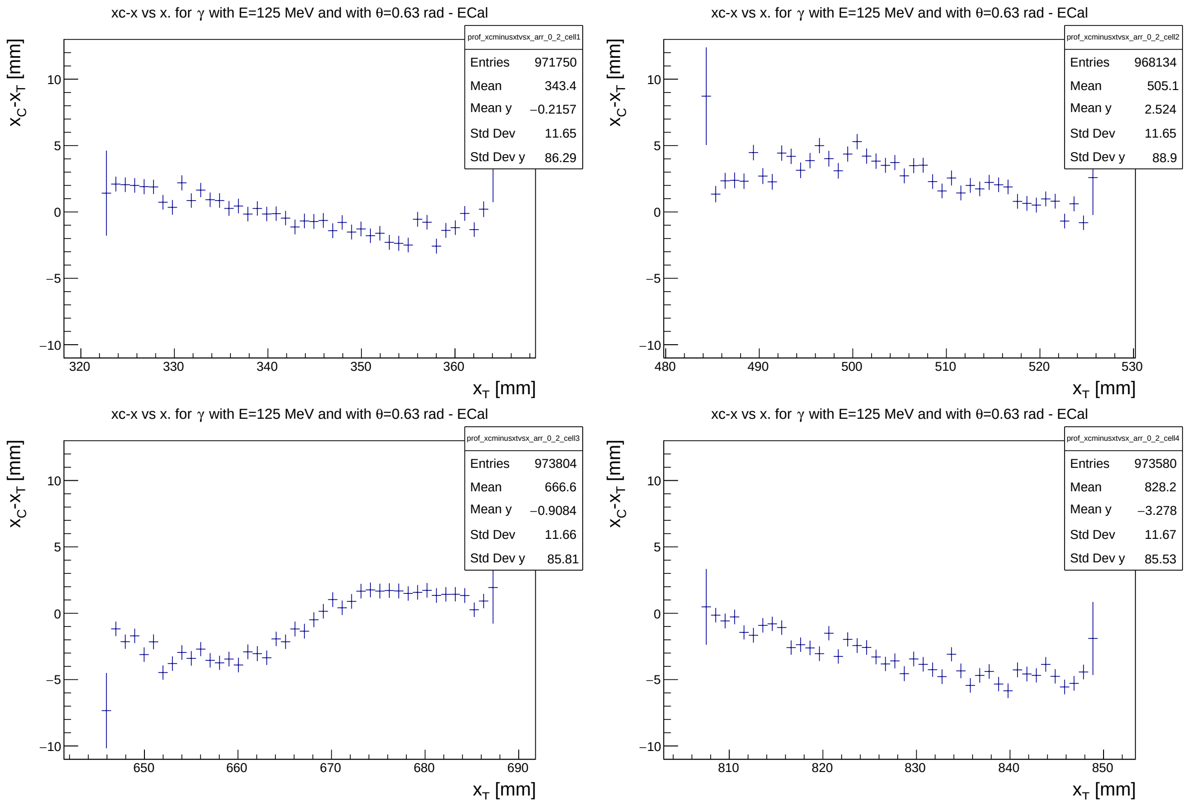

FIGURE 5.8: Comparison of the dependency of $X_c - X_T$ on X_T in the ECAL for particles generated with E=125 MeV, $\theta = 0.63$ rad and $\phi = \pi/2$ rad. X_T is generated in ranges corresponding to cell1(top-left), cell2(top-right), cell3(bottom-left) and cell4(bottom-right).

and energy E_i of the shower hits to take into account the difference between the actual particle E, θ and the nearest node's E_{node}, θ_{node} value.

It has been verified that $X(Y)_c$ has a very low dependency on E and almost a linear one on θ, as one could expect. Therefore, a possible energy correction is, to a first approximation, $E'_i = E_i \frac{E}{E_{node}}$, where E'_i is the corrected energy of the hit. The hit position should be modified with $x(y)'_i = x(y)_i + f(\Delta\theta)$, where $x(y)'_i$ is the corrected hit position and $\Delta\theta = \theta - \theta_{node}$.
As a first step, this procedure ignores the dependency of some parameters (σ, ρ_{XY}, E_{frac}, N_{hit}) on the distance between E-θ nodes that are closest to each other. The approximation is obviously more precise as the density of nodes increases and the distance between them decreases.
In addition, a correction of the hit time will have to be implemented to properly take into account the arrival time of the particle on the calorimeter face.

5.4 Hybrid simulation technique

Since the single-hit engine can be used to simulate photons lower than a given threshold E'_{thr} with a sufficient precision, a new model which uses the *point library* technique to simulate photons with energy $E > E'_{thr}$ and the single-hit engine for energies under this threshold has been created. This model should reduce the simulation time, as the very

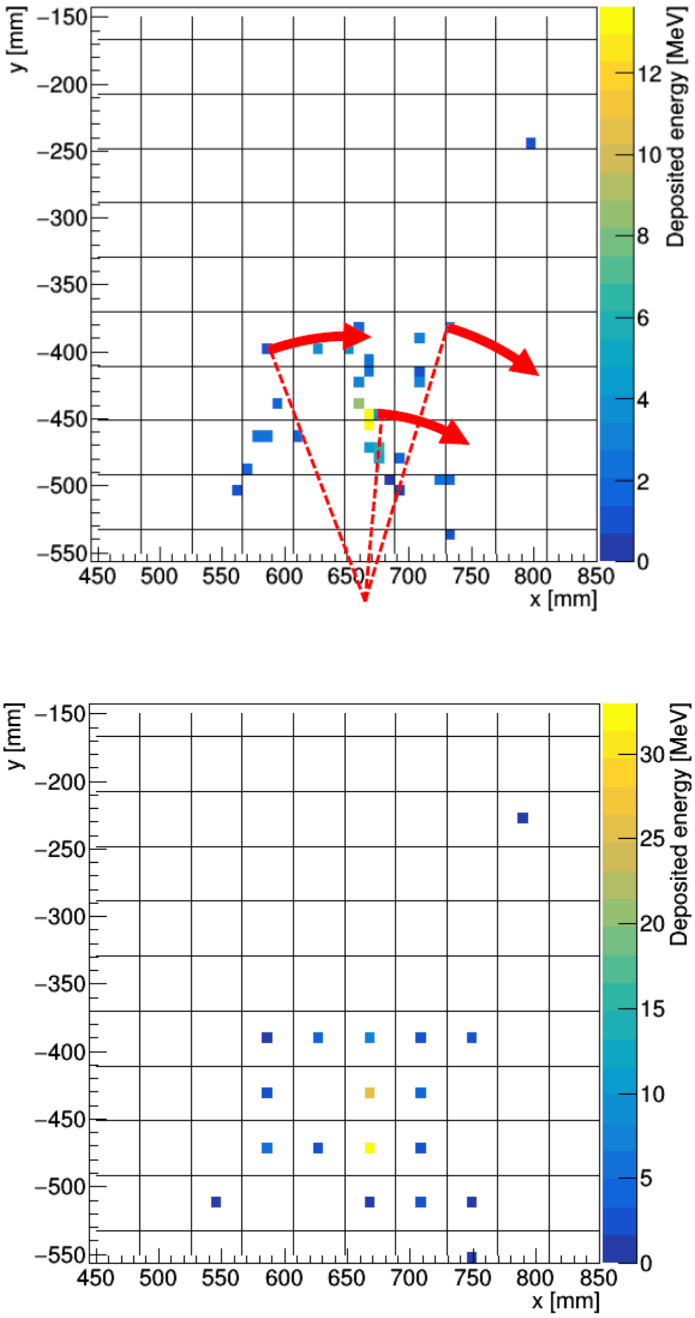

FIGURE 5.9: The shower hits are rotated during the simulation (top) and finally converted in cell hits (bottom). The black lines represent the division between ECAL cells, while the colored dots are the subcell hits. On the z axis is the hits energy.

large number of low energy photons is simulated with a simpler and faster model.
The single-hit engine and the *point library* have been built to simulate particles which enter the calorimeter from the SPD front face, but usually they can enter from other direction, as for example from the beam pipe. The fast simulation of the particles which enter the calorimeter not from the SPD face can be performed with properly modified version of the single-hit engine, but this procedure adds a not negligible degree of complexity

to the development of the engine. For this reason, as a firt step, I want to determine the relevance of the energy deposited in the calorimeter by the particles which enter the calorimeter not from the SPD face. If this energy is negligible with respect to the total energy deposited in the detector, as a first approximation the particles which enter the calorimeter not from the SPD face can be killed and a proper fast simulation for these particles may be developed in the future.With this goal in mind, some studies have been performed to measure the lost energy if the `G4Tracks` of the particles which enter the calorimeter not from the SPD face are killed without generating the CaloHits. As a first check the sum of energy depositions has been compared between three simulations (one thousand minimum bias events per simulation option) that have been performed using three different simulation methods (or options) specifically created by me with dedicated fast simulation models:

- *full* = standard *Geant4* simulation.
- *killpipe* = Particles entering the calorimeter not from SPD face are killed.
- *killspd* = Particles entering the calorimeter from SPD face are killed. With good approximation, *killspd* is the complement of *killpipe*.

If the energy deposited in the calorimeter for the *killspd* simulation is much less than the energy deposited for the *full* simulation, we can conclude that the effect of killing the `G4Tracks` which enter the calorimeter not from the SPD face is negligible. The released energy distributions for the *full* and *killspd* options in the ECAL and in the HCAL are plotted in Figure 5.10.

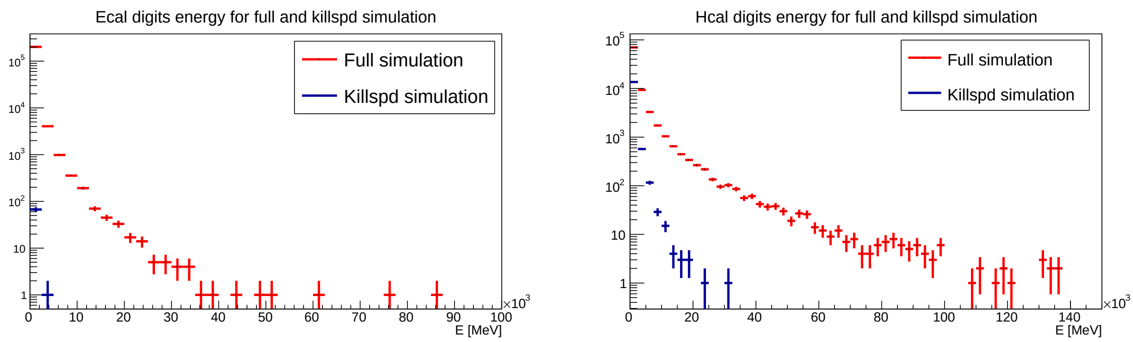

FIGURE 5.10: Distribution of the Energy deposited in the ECAL (left) and in the HCAL (right) after the reconstruction phase for the *full* (red) and *killspd* (blue) options.

Table 5.3 shows a negligible effect on the total energy released in the ECAL when particles entering the calorimeter not from the SPD face are killed, while a effect of $\simeq 5\%$ is observed in the HCAL (Table 5.4).

A more specific check has been performed to evaluate the impact on the reconstruction of $D^+ \to \eta' \pi^+$ decays, with $\eta' \to \pi^+\pi^-\gamma$ by comparing two simulations, consisting of 100k events each, of the signal for the *full* and *killpipe* options. If the energy released in the calorimeter by particles entering the detector not from the SPD face is negligible, we expect the distributions of reconstructed quantities for the *full* and *killpipe* options to be compatible.

TABLE 5.3: Table of energy deposited in the ECAL (after the reconstruction phase) for the *full* and *killspd* options.

measured quantities	total # of hits	mean Energy per hit	total E / total E for *full* [%]
full	207820	618.2	100
killspd	68	593.6	0.03

TABLE 5.4: Energy deposited in the HCAL (after the reconstruction phase) for the *full* and *killspd* options.

measured quantities	total # of hits	mean Energy per hit	total E / total E for *full* [%]
full	88122	2371.0 MeV/c^2	100
killspd	14356	702.1 MeV/c^2	4.8

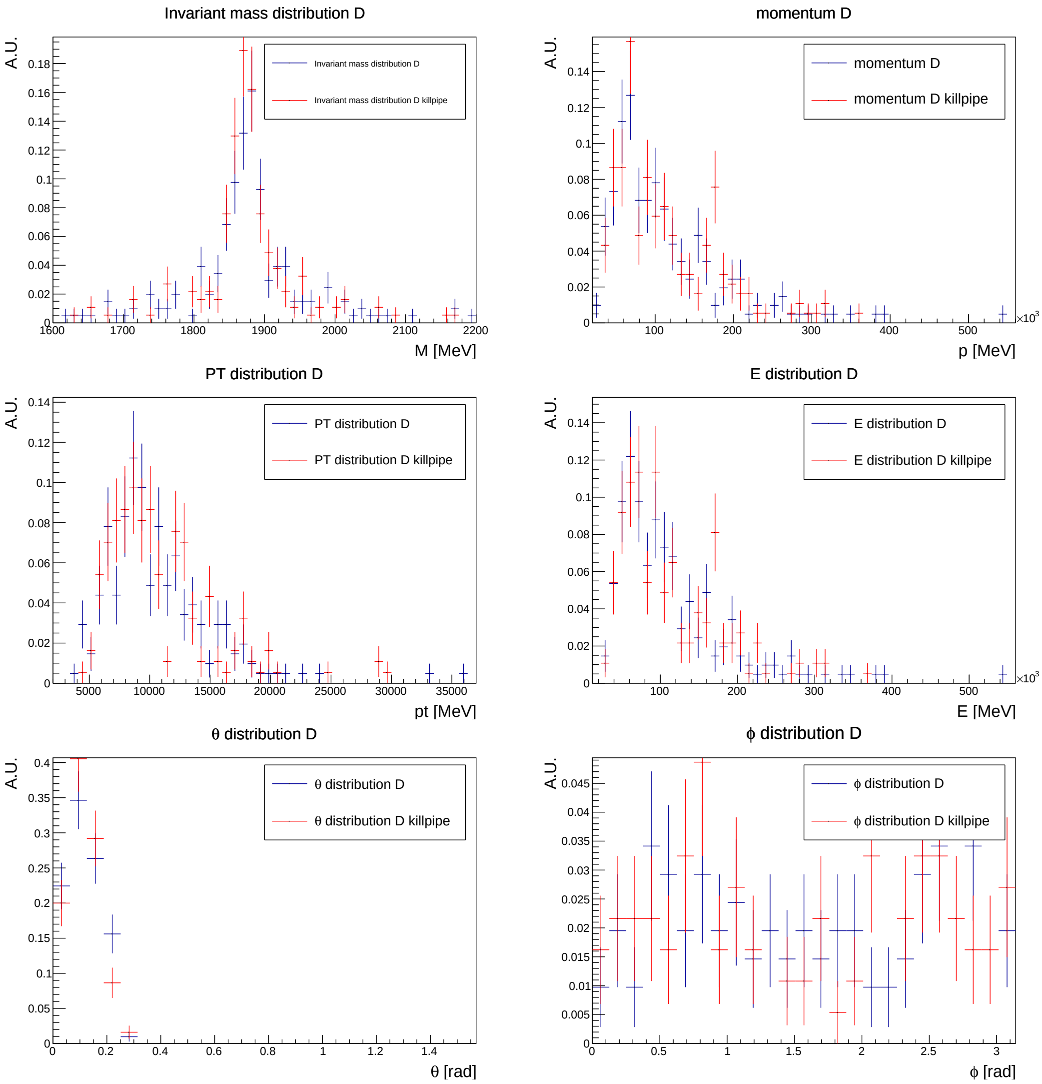

FIGURE 5.11: Comparison between *full* (blue) and *killpipe* (red) options for the D^+ reconstructed quantites: M, p, p_t, E, θ, ϕ.

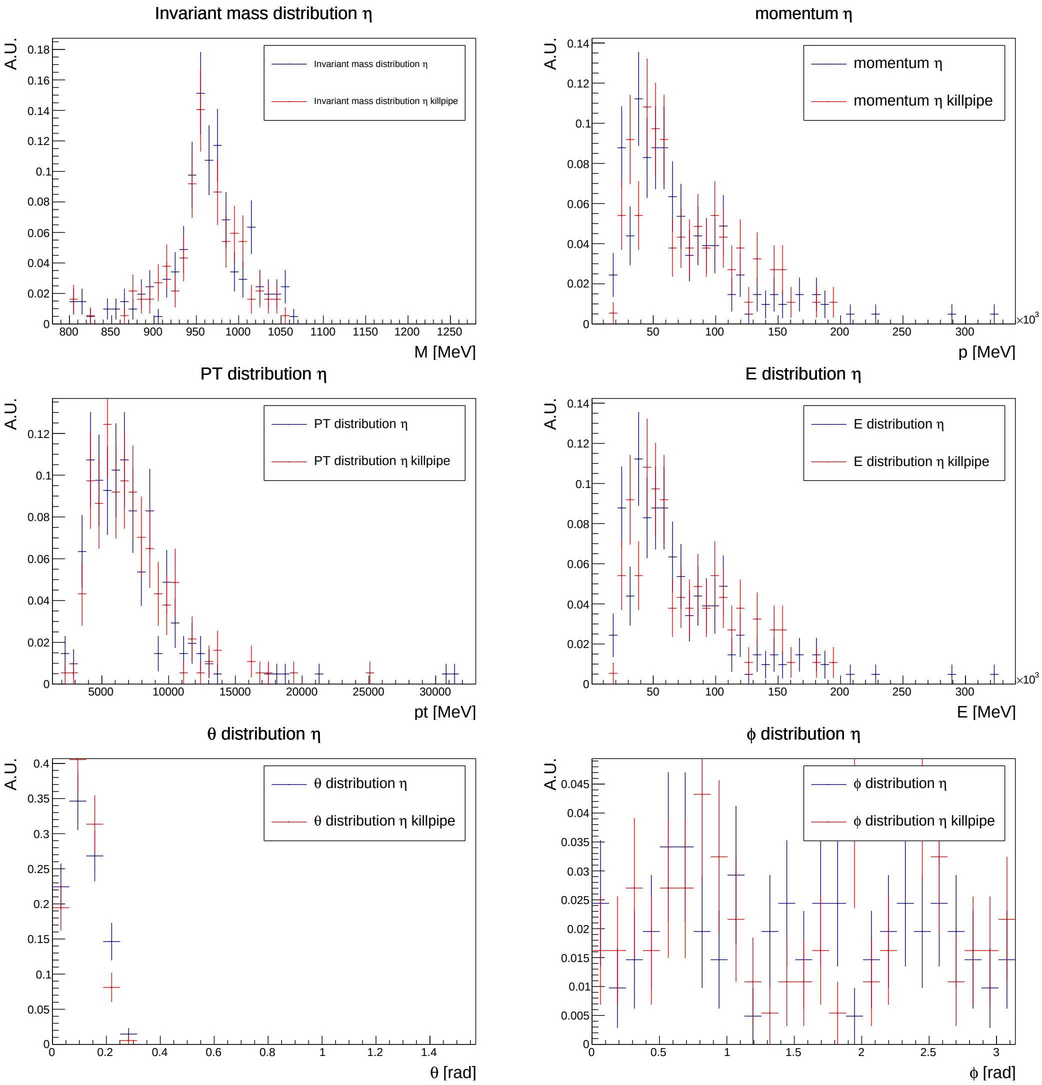

FIGURE 5.12: Comparison between *full* (blue) and *killpipe* (red) options for the η reconstructed quantites: M, p, p_t, E, θ, ϕ.

Figure 5.11 shows the comparison between *full* and *killpipe* options for the distributions of invariant mass M, momentum p, p_t, E, θ and ϕ of the D^+. Figure 5.12 and Figure 5.13 display the same quantities' distributions for the η and the γ, respectively. The plots show good agreement within the statistical errors, which are quite large, due to the low statistic sample. It can be conluded that, to a first approximation, the energy released in the calorimeter by tracks entering from the pipe hole is negligible. A further study with a larger simulated sample is needed to confirm this result. A possible future solution for this issue is the implementation of special "hit maps".

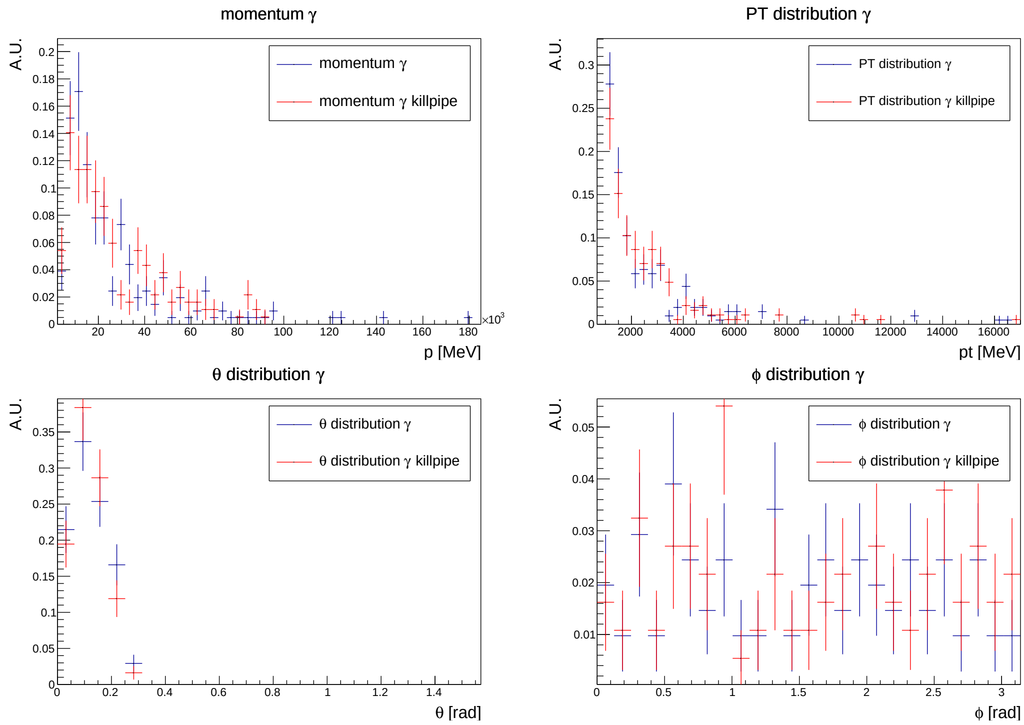

FIGURE 5.13: Comparison between *full* (blue) and *killpipe* (red) options for the γ reconstructed quantites: p, p_t, θ, ϕ.

Chapter 6

Results

After the implementation of the single-hit engine and the development of the first version of the *point library*, their performances in terms of accuracy and speed must be evaluated. Moreover, it is also important to estimate how well the current standard simulation based on *Geant4* reproduces the real data to set the required level of agreement between the fast and the standard simulations. To this end, I performed a dedicated physics analysis of the $D^+ \to \eta'\pi^+$ and $D_s^+ \to \eta'\pi^+$ decays, with $\eta' \to \pi^+\pi^-\gamma$, for real data and MC samples. Simulations of $D^+ \to \eta'\pi^+$ decays, with $\eta' \to \pi^+\pi^-\gamma$, have been performed to test the single-hit engine by comparing the results with a standard simulation. I observed a gain of about a factor 50 in the computing time required to simulate photons with energy of the order of 1 GeV in the calorimeter with the single-hit engine compared to the standard *Geant4* simulation.
A similar type of timing test has been run for the *point library*. The results showed a gain of at least a factor 20 in the computing time required to simulate $O(1)$ GeV photons in the calorimeter compared to standard *Geant4* simulation. The difference between the gain factors achieved with the single-hit and the *point library* methods arises from the higher number of calorimeter cell hits *C++ objects* created and stored in memory when the *point library* is used. These results imply a gain in the overall event simulation time of about 50% compared to the standard simulation.

6.1 Data analysis and comparison with Monte Carlo sample

An important goal for the next steps of development of the fast simulation models is the estimate of the needed level of agreement between these models and the standard simulation. For this reason, it is interesting to study the current level of precision with which the *Geant4*-based simulation reproduces the real data.
With this goal in mind, I performed a study of the $D^+ \to \eta'\pi^+$ and $D_s^+ \to \eta'\pi^+$ decays, with $\eta' \to \pi^+\pi^-\gamma$, for the data collected by LHCb in 2016. The MC sample consists of 10M simulated $D_s^+ \to \eta'\pi^+$, with $\eta' \to \pi^+\pi^-\gamma$, decays.
The $\eta' \to \pi^+\pi^-\gamma$ channel is the second most abundant decay mode of the η' meson and its choice is motivated by the good reconstruction efficiency associated to a single photon compared to decays where multiple neutral objects appear in the final state. Two opposite-charge tracks with pion mass hypothesis and a photon candidate are first combined to form an η' candidate. The η' candidate is then combined with the bachelor pion to form a $D_{(s)}^+$ meson candidate.

As mentioned in Chapter 1, the LHCb trigger is organized in two levels: the Level 0 trigger and the High Level trigger. For every event available to offline processing, the information about the trigger chain responsible for accepting the event is stored and can be used to restrict the analysis to the events satisfying a well-defined set of trigger lines. A trigger line is a sequence of algorithms returning a decision to accept or reject an event according to a particular event topology. Given a trigger line and a track (or a combination of tracks), the events are classified into two categories:

- Trigger On Signal (TOS) events. These are events triggered on the signal decay chain independently of the presence of other tracks. This condition is satisfied if the information used to reconstruct the signal tracks is sufficient to satisfy the selection criteria of the respective trigger line.
- Trigger Independent-of-Signal (TIS) events. These events are triggered independently of the presence of the signal. A candidate is considered to be TIS with respect to a trigger selection if removing it from the event would still cause the trigger selection to accept the event, i.e. if the other particles in the event are sufficient to satisfy the trigger selection.

Before discussing the selection cuts, it is useful to define some relevant quantities used.

- Primary Vertex (PV): the space-point of the reconstructed primary pp interaction.
- Impact Parameter (IP): magnitude of the three-dimensional impact parameter vector of a particle. Generally, given a vertex $\vec{v}_0$ and a particle trajectory that can be parametrised as a straight line $\vec{v}(t) = \vec{v}_p + \vec{p}t$, where $\vec{p}$ is the particle momentum and $\vec{v}_p$ is a generic point of the trajectory, the impact parameter vector is defined as the vector formed by the point of the track closest to $\vec{v}_0$

$$\vec{IP} = (\vec{v}_p - \vec{v}_0) - \frac{\vec{p} \cdot (\vec{v}_p - \vec{v}_0)}{|\vec{p}|^2}\vec{p}$$

  For example, D_s^+ daughters have in general large impact parameters with respect to the PV because of the displaced vertex of the D_s^+ meson. Instead, the IP of the D_s^+ meson with respect to the PV tends to be consistent with zero within the experimental uncertainty, in the assumption of "prompt" decays (i.e. coming from the PV).
- IP χ^2: defined as the difference in χ^2 of the primary vertex fit with and without considering the particle in the fit. For a particle not coming from the PV, IP χ^2 assumes larger values than a prompt particle.
- $\mathcal{P}_{ghost}$: the probability for a track to be a "ghost" track, that is a misidentified track.
- χ^2_{trk}/n_{dof}: chi-square of the reconstructed track fit, normalized to the degrees of freedom.
- $PIDK(e)$: is the Delta Log Likelihood variable between the kaon (electron) and pion hypothesis

$$DLL_{K(e)\pi} = \log \mathcal{L}_{K(e)} - \log \mathcal{L}_\pi = \log \frac{\mathcal{L}_{K(e)}}{\mathcal{L}_\pi}$$

Larger values of $DLL_{K(e)\pi}$ indicate a larger likelihood for the kaon (electron) hypothesis over the pion hypothesis.

The η' candidates are reconstructed by combining pairs of oppositely charged particles with a photon of $p_T > 1$ GeV/c. The η' charged decay products must not be identified as kaons by the particle identification system, and must be displaced from the PV. For this reason it is required that $PIDK < -5$ and the cut IP $\chi^2(\pi^\pm) > 25$ is applied to remove η' candidates which come from the PV. To calculate the $D^\pm_{(s)}$ mass, the η' candidate mass is required to satisfy $0.934 < M(\eta') < 0.982$ GeV/c^2, without placing constraints on the origin of the $D^\pm_{(s)}$ meson. The bachelor pion must be identified as a pion rather than as an electron, muon or kaon by setting cuts to the $PIDK(e)$ and *isMuons* variables. Candidate $D^\pm_{(s)}$ mesons are required to have $p_T > 2$ GeV/c in all decay modes, and mass in the range $1.82 < M(\eta'\pi^\pm) < 2.03$ GeV/c^2. The scalar sum of the transverse momenta of charged decay products ($\sum_{\pi' s} p_T$) must exceed 2.8 GeV/c. In events with multiple $D_{(s)}$ candidates only one randomly selected candidate is kept. This procedure removes less than 2% of the original candidates.
A combinatorial background contribution is present. Background from partially reconstructed $D^\pm_{(s)} \to \eta'\rho^\pm$ decays is suppressed by requiring $M(\eta'\pi^\pm) > 1.82$ GeV/c^2. Background from $D^\pm_{(s)} \to \pi^\mp\pi^\pm\pi^\pm$ decays, paired with a random photon, is suppressed by requiring the invariant mass of the three charged hadrons to be less than 1.8 GeV/c^2.
A summary of selection cuts is provided in Table 6.1. The same selection criteria have been applied to the data and MC samples.

In the fit to the data [26], the signal model is a JohnsonSU function [27] for both D^+ and D_s^+ (only D_s for the MC sample):

$$f(x) = \frac{1}{2\pi\sqrt{1+z^2}}\frac{1}{\tau\chi}\exp\left\{-\frac{1}{2}\left[-\nu+\frac{1}{\tau}\sinh^{-1}(z)\right]^2\right\}$$

where

$$\chi = \sigma\sqrt{\frac{1}{2}(e^{\tau^2}-1)[e^{\tau^2}\cosh(-1\nu\tau)+1]}$$

and

$$z = \left(\frac{x-\mu}{\chi}\right) - e^{\frac{1}{2}\tau^2}\sinh^{-1}(-\nu\tau)$$

This distribution models experimental data that are approximately gaussian. The parameters μ and σ represent the mean value and width of the distribution, while the shape parameters ν and τ describe the asymmetry (due, e.g., to radiative effects) and sharpness of the distribution, respectively.
The background is modeled with a Chebychev polynomial of the 4th order. A Chebychev polynomial of the n-th order is defined by:

$$T(x; C_0, ..., c_n) = \frac{1}{N}\cdot\left(T^0(x) + \sum_{k=1}^{n} c_k T^k(x)\right)$$

where $T^k(x)$ is a Chebychev polynomial of k-th order, c_k is the related coefficient and N is a normalization factor. The peaking background is mainly composed of $D^+ \to \phi\pi^+$ and

TABLE 6.1: Summary of selection cuts for the $D \to \eta'\pi$ channel.

Variable	Cut
Stripping	
$p(\gamma)$	> 1000 MeV/c
$p_T(\gamma)$	> 1000 MeV/c
$\mathcal{P}_{ghost}(\pi_{bach})$	< 0.5
$hasRich(\pi_{bach})$	True
$\eta(\pi_{bach})$	$\in [2, 5]$
IP $\chi^2(\pi_{bach})$	> 25
$\chi^2_{trk}/n_{dof}(\pi_{bach})$	< 3
$p_T(\pi_{bach})$	> 350 MeV/c
$p_T(\pi^\pm)$	> 350 MeV/c
$p(\pi^\pm)$	> 1000 MeV/c
$\mathcal{P}_{ghost}(\pi^\pm)$	< 0.5
$\chi^2_{trk}/n_{dof}(\pi^\pm)$	< 3
$\eta(\pi^\pm)$	$\in [2, 5]$
IP $\chi^2(\pi^\pm)$	> 25
$hasRich(\pi^\pm)$	True
$PIDK(\pi^\pm)$	< -5
$M(D)$	$\in [1600, 2200]$ MeV/c^2
$\mathcal{P}(\chi^2, n_{dof})$	> 0.03
$M(\eta')$	$\in [934, 982]$ MeV/c^2
$M(\eta'\pi^\pm)$	$\in [1820, 2030]$ MeV/c^2
$p_T(D)$	> 2000 MeV/c
$M(3\pi)$	< 1800 MeV/c^2
$\sum_{\pi's} p_T$	> 2800 MeV/c
$isPhoton(\gamma)$	> 0.6
$P(\pi_{bach})$	$\in [3000, 60000]$ MeV/c
$PIDK(\pi_{bach})$	< 3
$PIDK(\pi_{bach})$	< 0
$PIDe(\pi_{bach})$	< 0
$isMuon(\pi_{bach})$	False
$p_T(\pi_{bach})$	> 450 MeV/c
$p(\pi_{bach})$	$\in [4500, 55000]$ MeV/c
Remove multiple candidates	

$D_s^+ \to \phi\pi^+$, with $\phi \to \pi^+\pi^-\pi^0_{\gamma\gamma}$, decays. Their contributions are modeled with the so-called Cruijff PDF. The Cruijff function is a Gaussian with different left-right resolutions and non-Gaussian tails [28].
The mass distribution fits for data and MC samples (integrated over charge and magnet polarity) are shown in Figure 6.1.

Table 6.2 shows the mean and width of the $D_s^\pm$ mass distribution parameters resulting from the fit for the TIS and TOS sample sets. The data and MC parameters are in agreement within 3 σ for both TIS and TOS cases. This corresponds to a mass agreement within 1 MeV/c^2, and an agreement to better than 10% on the mass resolution. It must be noted that the statistical uncertainty associated to the MC sample is large due to the low statistic, which in turn is caused by the very low total reconstruction and selection efficiencies (~800 total candidates out of 10M total simulated decays), thus preventing comparisons at greater levels of precision.

TABLE 6.2: Fitted D_s parameters for the TIS and TOS samples.

	mean $M(D_s^\pm)$ [MeV/c^2]	width $M(D_s^\pm)$ [MeV/c^2]
	TIS	
Data	1968.70 ± 0.04	8.6344 ± 0.0783
MC	1968.10 ± 0.51	8.8591 ± 1.0879
	TOS	
Data	1968.60 ± 0.04	9.7345 ± 0.0850
MC	1970.0 ± 0.6	9.7766 ± 0.7653

To further study the accuracy of the MC simulation, it is interesting to compare the η' invariant mass distributions, as it should be more sensitive to the γ reconstruction. For this reason, η' mesons in the range $0.850 < M(\eta') < 1.05$ GeV/c^2 have been selected after the requirement $1.945 < M(D_s) < 1.995$ GeV/c^2. Figure 6.2 shows the comparison between the data and MC distributions of $M(\eta')$. These distributions have then been fitted with a Gaussian for the η' signal and a constant for the background to estimate the mean and width of the η' mass distribution. The results are shown in Table 6.3. The mean $M(\eta')$ values of the MC and data samples are consistent within 2-3 MeV/c^2.
These results give an idea of the accuracy that a fast simulation must achieve with respect to a standard *Geant4* simulation. It can be concluded that the requested precision with which a fast simulation must reproduce the $M(\eta')$ distribution obtained by a *Geant4* simulation is of the order of 1 MeV/c^2.

6.2 Single-hit engine performance

The simulations of $D^+ \to \eta'\pi^+$ decays, with $\eta' \to \pi^+\pi^-\gamma$ decays used to test the single-hit engine have been performed using a "particle gun" simulator. A particle gun is a simplified simulation in which a single signal particle is spawned instead of generating a complete event with PYTHIA. The kinematics and origin position of the particle can be configured to have the desired distributions. The particle then decays into the requested final state.

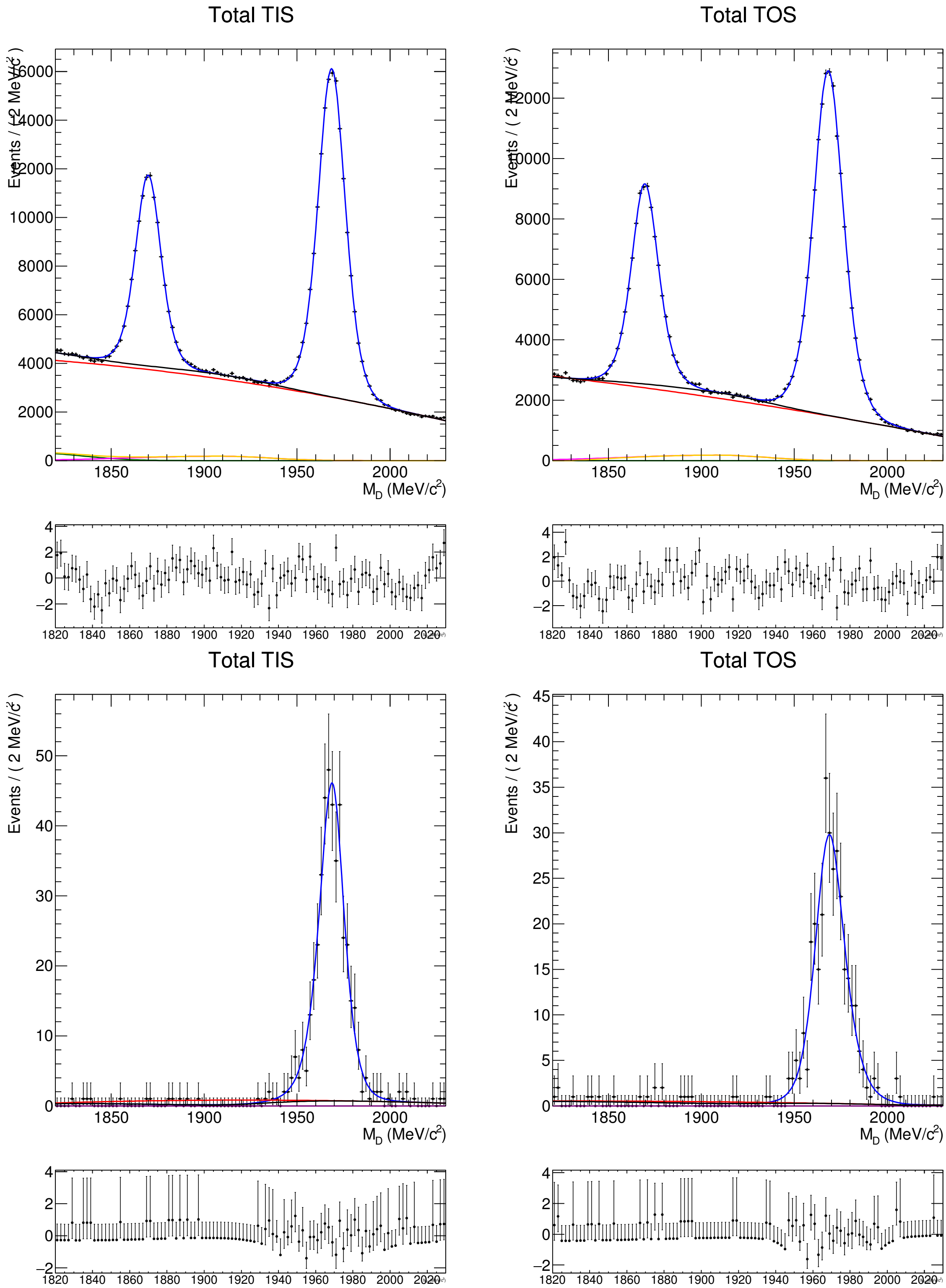

FIGURE 6.1: Mass distributions for the 2016 data (top) and MC (bottom) samples (integrated over charge and magnet polarity), with fit overlayed. Left: TIS samples; right: TOS samples. The blue curve represents the fitted pdf curve. The red curve represents the fitted combinatorial background curve. The magenta curve represents the fitted $D_s^\pm$ peaking background curve. Green curve represents the fitted $D^\pm$ peaking background curve (Data only). The orange curve represents the fitted curve of the summed peaking backgrounds of the $D^\pm$ and $D_s^\pm$ (Data only). The black curve represents the fitted total background curve. The background curves for the MC sample are close to 0.

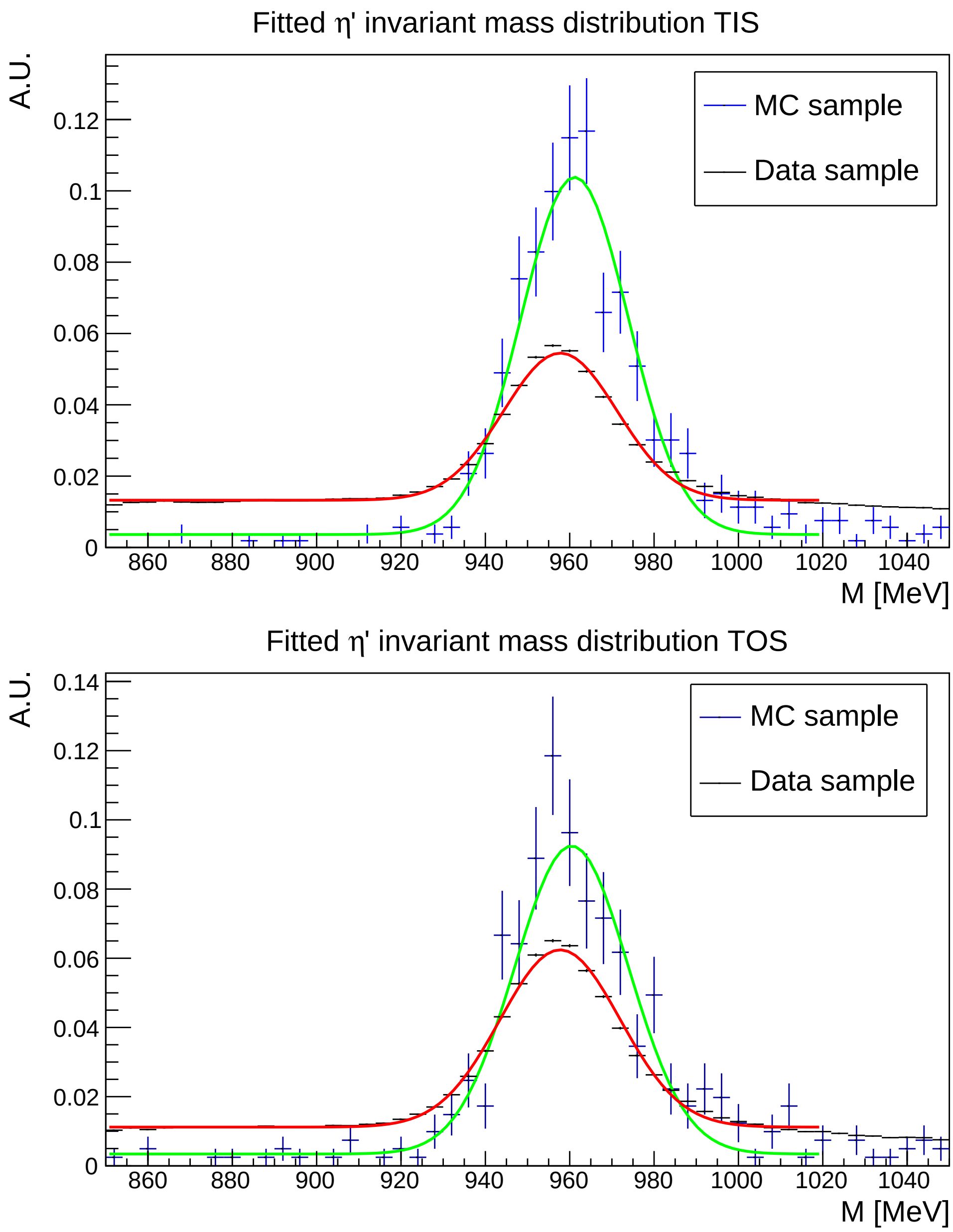

FIGURE 6.2: Comparison between the η' mass distributions of the 2016 data (black) and MC samples (blue) (integrated over charge and magnet polarity). Top: TIS samples; Bottom: TOS samples. The green curve represents the fitted pdf curve on the MC sample. The red curve represents the fitted pdf curve on the data sample.

TABLE 6.3: Fitted η' parameters for the TIS and TOS samples.

	mean $M(\eta')$ [MeV/c^2]	width $M(\eta')$ [MeV/c^2]
	TIS	
Data	957.8 ± 0.1	13.46 ± 0.06
MC	961.2 ± 0.8	12.74 ± 0.68
	TOS	
Data	957.7 ± 0.1	14.25 ± 0.06
MC	960.4 ± 0.9	13.49 ± 0.89

The analysis of the $D^+ \rightarrow \eta'\pi^+$ decays, with $\eta' \rightarrow \pi^+\pi^-\gamma$ decay has been chosen to test the accuracy of the single-hit engine because the information on the energy deposited by the γ in the calorimeter influences the reconstruction of the η' and D candidates. We have studied the agreement between the distributions of the reconstructed quantities (invariant mass M, energy E, momentum p, transverse momentum p_T, incident angle θ and azimuthal angle ϕ) of the D, η and γ obtained with our simple single-hit model and the full simulation.
D mesons were generated with 10 GeV $\leq p \leq$ 15 GeV/c, so that the resulting γ energy falls in the range covered by the single-hit engine. After the reconstruction I obtained 3450 D candidates out of 500k full simulated events which leads to a reconstruction efficiency (number of reconstructed candidates divided by the total number of simulated events) $\epsilon_{reco} = (6.9 \pm 0.1) \times 10^{-3}$, where the uncertainty is statistical. This result can be compared to the 2827 D reconstructed candidates out of 460k obtained with the single-hit engine, corresponding to $\epsilon_{reco} = (6.1 \pm 0.1) \times 10^{-3}$. The efficiencies are surprisingly in good agreement considering the simplicity of the model. Figures 6.3, 6.4 and 6.5 show the comparison between the distributions of reconstructed quantities of the D, η' and γ, respectively, for the *Geant4* and single-hit engine simulations.

The distributions are in good agreement, although the number of reconstructed D and η in the M distribution peak is lower for the single-hit engine. This difference could be associated to the fixed time slot of the fast generated hits and to the low number of hits (four at best, i.e one per subdetector) created by the engine, which can reduce the reconstruction efficiency depending on the photon energy. However, it can be concluded that the single-hit engine is a very effective model in his working energy range, bearing in mind the very simple parameterization used.

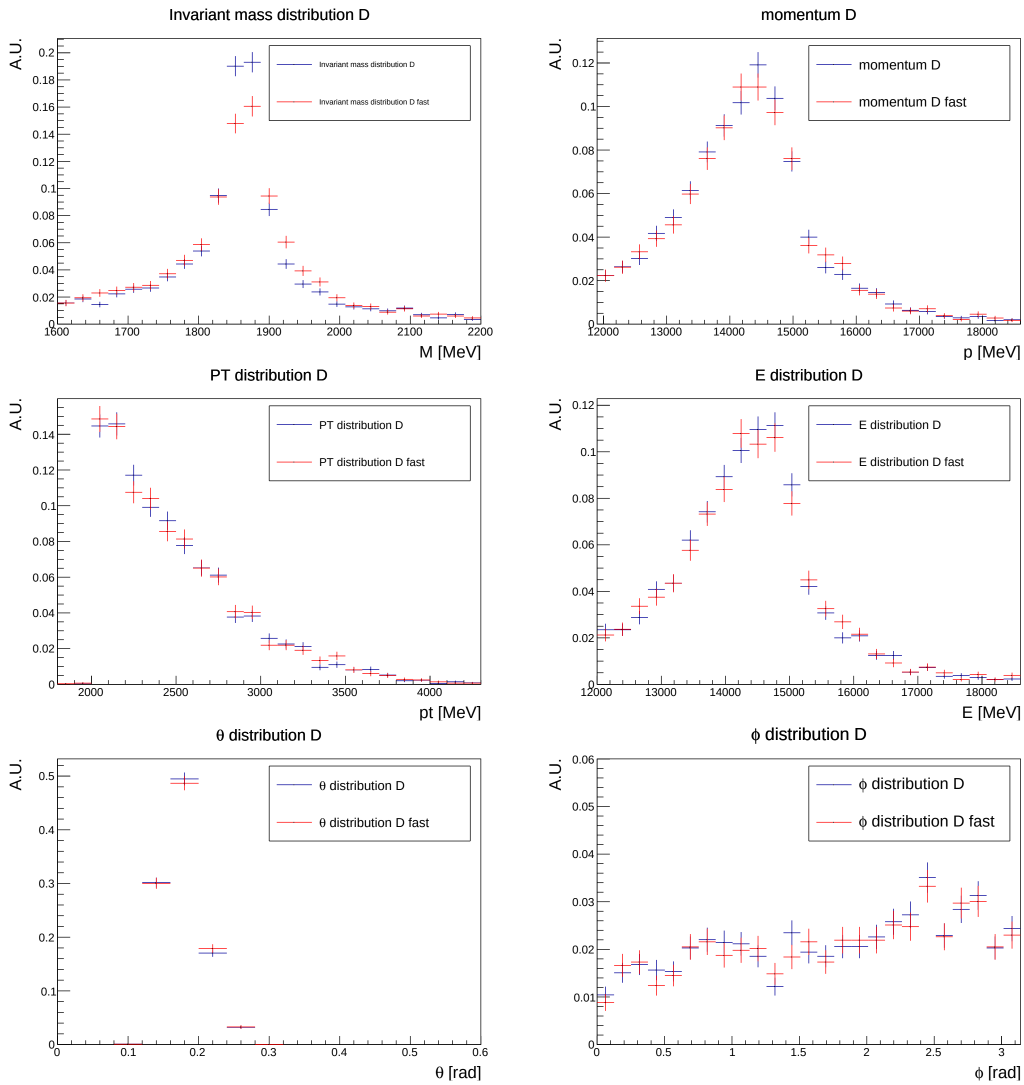

FIGURE 6.3: Comparison between standard (blue) and single-hit engine (red) simulations for the D reconstructed quantities: M, p, p_t, E, θ, ϕ.

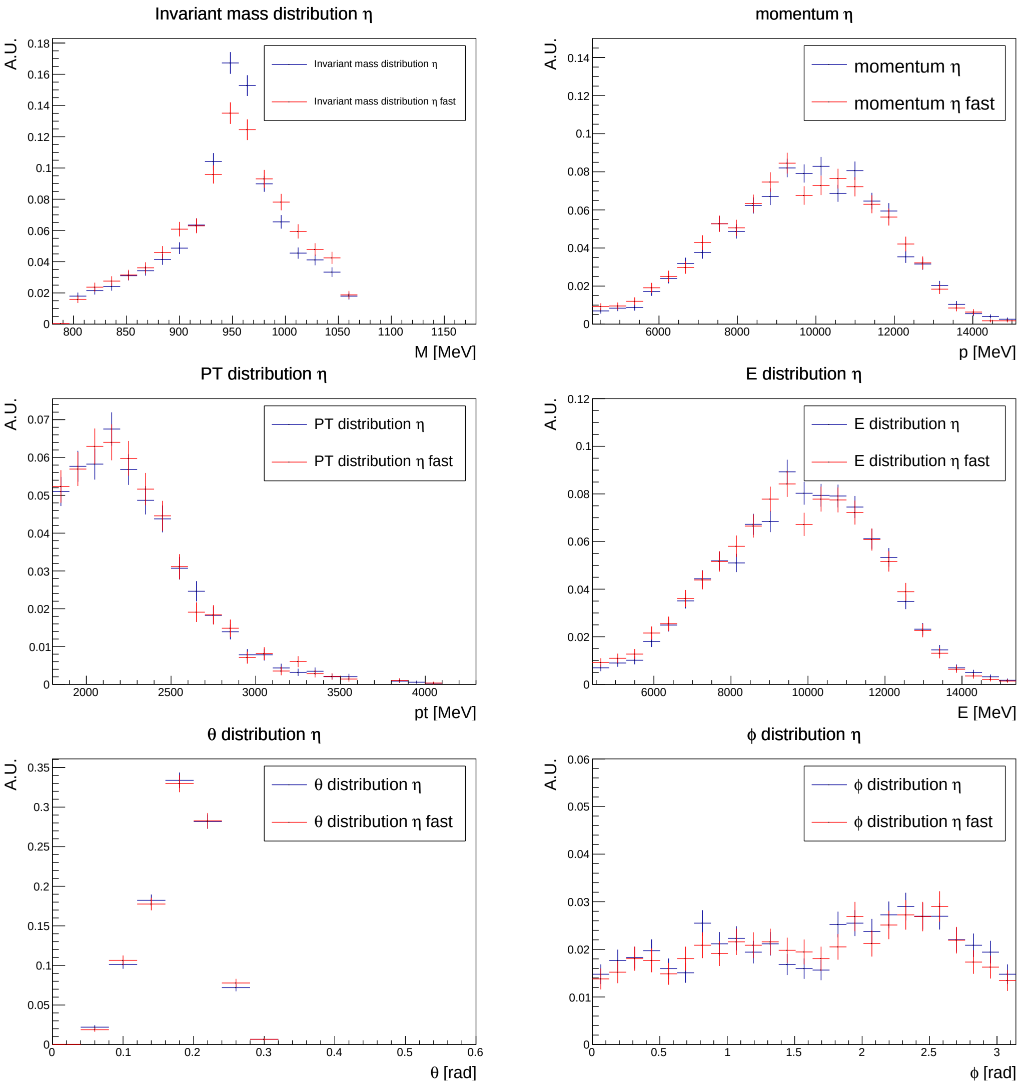

FIGURE 6.4: Comparison between standard (blue) and single-hit engine (red) simulations for the η reconstructed quantities: M, p, p_t, E, θ, ϕ.

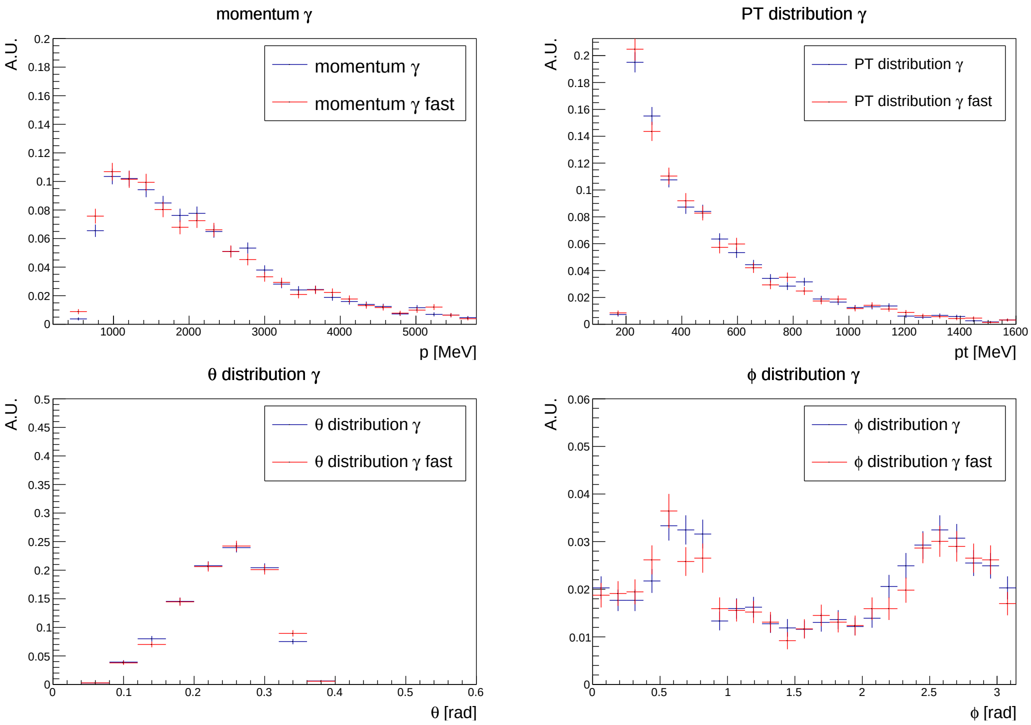

FIGURE 6.5: Comparison between standard (blue) and single-hit engine (red) simulations for the γ reconstructed quantites: p, p_t, θ, ϕ.

6.3 Photon simulation with the *point library*: comparison with *Geant4*

To determine the level of compatibility of the *point library* model with the standard *Geant4* process, some test simulations of single photons generated at the SPD face have been performed for various E, θ and ϕ values. If the *point library* approximates the standard *Geant4* process with a sufficient accuracy, the following parameters must be in agreement when the two simulations are compared:

- the cluster centroid $X(Y)_c$ and width $\sigma^2_{X(Y)}$, defined in Section 5.3.2.
- the cluster correlation defined as $\rho_{XY} = \frac{\sum E_i(X_i - X_c)(Y_i - Y_c)}{\sigma_X \sigma_Y \sum E_i}$.
- the cluster fractionary energy released defined as $E_{frac} = \sum \frac{E_i}{E_{True}}$, with E_{True} the generated energy of the photon.

where E_i, X_i and Y_i are the energy and coordinates of the i-th hit, respectively.
These parameters cannot be simulated by the single-hit model, where each cluster is made of a single energy deposit. Figure 6.6 and Figure 6.7 show the results of some comparisons between the *point library* and the standard *Geant4* simulations for photons generated with $E = 2.75$ GeV, $\theta = 0.26$ rad and $E = 50$ GeV, $\theta = 0.26$ rad, respectively. The generated vertex position of the photon $x_{gen} = 668$ mm, $y_{gen} = -504$ mm, $z_{gen} = 12290$ mm is the same for both simulations, while $\phi = \pi/2$ rad for the *point library* and $\phi = \pi/4$ rad for the *Geant4* simulation. The fast generated hits are then rotated around the z-axis to match the generated ϕ value of the standard simulation. In other words, the points of the library had to be rotated by 45 deg but not translated.
The agreement between the parameters obtained from the rotated *point library* and from the *Geant4* simulation at $\phi = \pi/4$ is good.
To verify the full procedure of translation and rotation of the "points" another similar test simulation has been performed. Figure 6.8 and Figure 6.9 show the results of some comparisons between the *point library* and the standard *Geant4* simulations for photons generated with $E = 2.75$ GeV, $\theta = 0.09$ rad and $E = 50$ GeV, $\theta = 0.26$ rad, respectively. However in this case the generated vertex position is different: $x_{gen} = 2862$ mm, $y_{gen} = -504$ mm, $z_{gen} = 12290$ mm (outer section) for the standard simulation; $x_{gen} = 668$ mm, $y_{gen} = -504$ mm, $z_{gen} = 12290$ mm (inner section) for the *point library*. That is, in this case the points were rotated and then translated according to the particle entrance position in the calorimeter. Even if the points are rotated and then translated, the agreement does not worsen, proving that the idea behind the *point library* works.

These results verify that the *point library* reproduces with an overall good precision the photon propagation in the calorimeter simulated by *Geant4* while significantly reducing the simulation time in the detector.
As a final remark, the same single photon performance tests showed in this section have not been performed for the single-hit engine because the parameters defined above don't have a meaning if there is only one or zero hit per subdetector. However, it has been verified that the single-hit engine creates hits in positions consistent with the $X(Y)_c$ obtained with a standard simulation. Nevertheless, one of the main drawbacks of the single-hit engine is that, for obvious reasons, it doesn't give information on the cluster

width and energy distribution. This limitation becomes more relevant with increasing photon energy, as the clustering algorithm might not associate the fast-generated hit with an actual track. This issue is solved with the use of the *point library*, which produces hit distributions much more similar to a standard simulation than the single-hit engine.

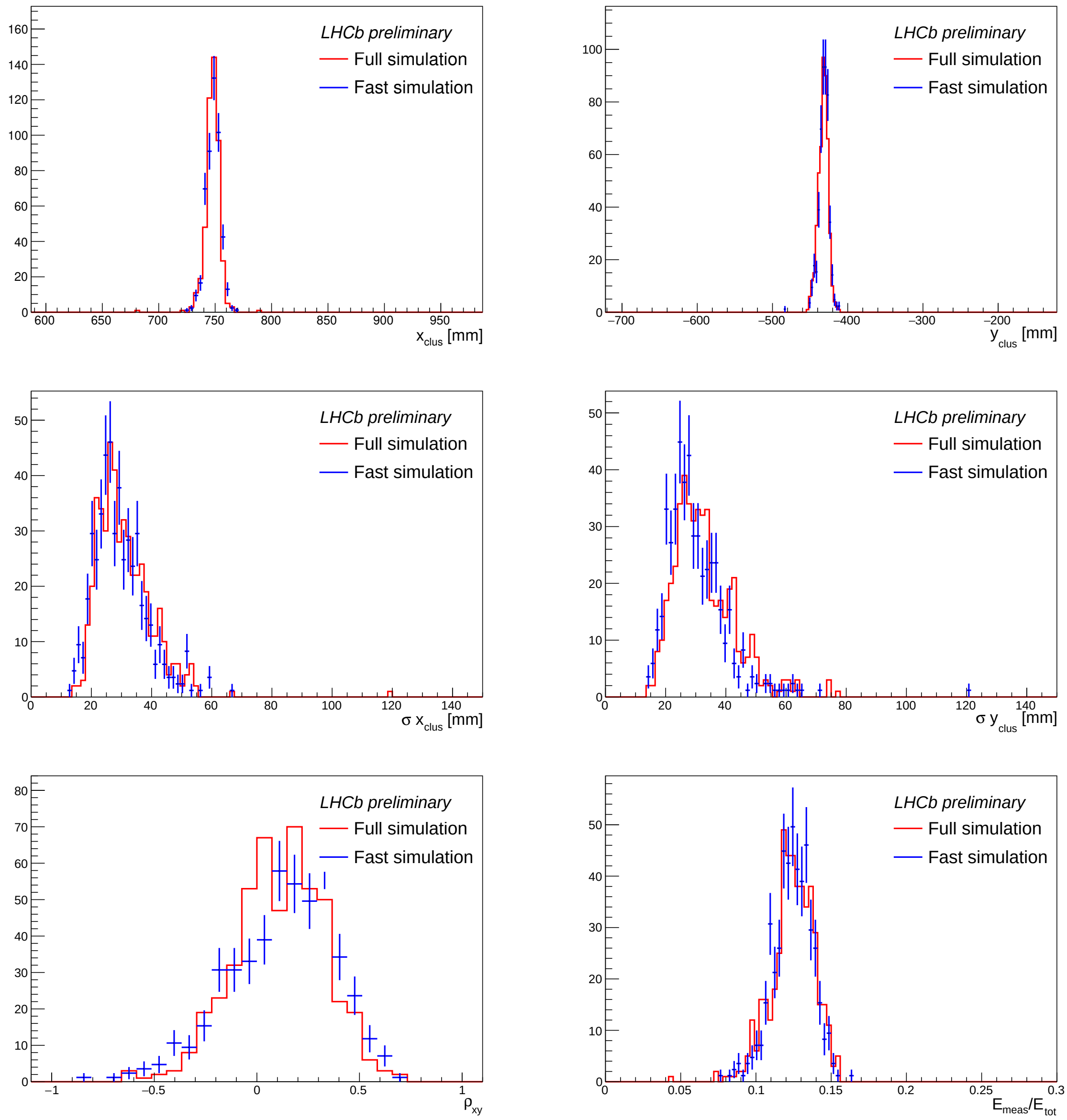

FIGURE 6.6: Comparison between the $X(Y)_c$, $\sigma_{X(Y)}$, ρ_{XY} and E_{frac} distributions for the *point library* model and *Geant4* simulation. The photon has $E = 2.75$ GeV, $\theta = 0.26$ rad and $\phi = \pi/4$ rad and is generated in the vertex position $x_{gen} = 668$ mm, $y_{gen} = -504$ mm, $z_{gen} = 12290$ mm, that is in the bottom-right quadrant just outside the SPD.

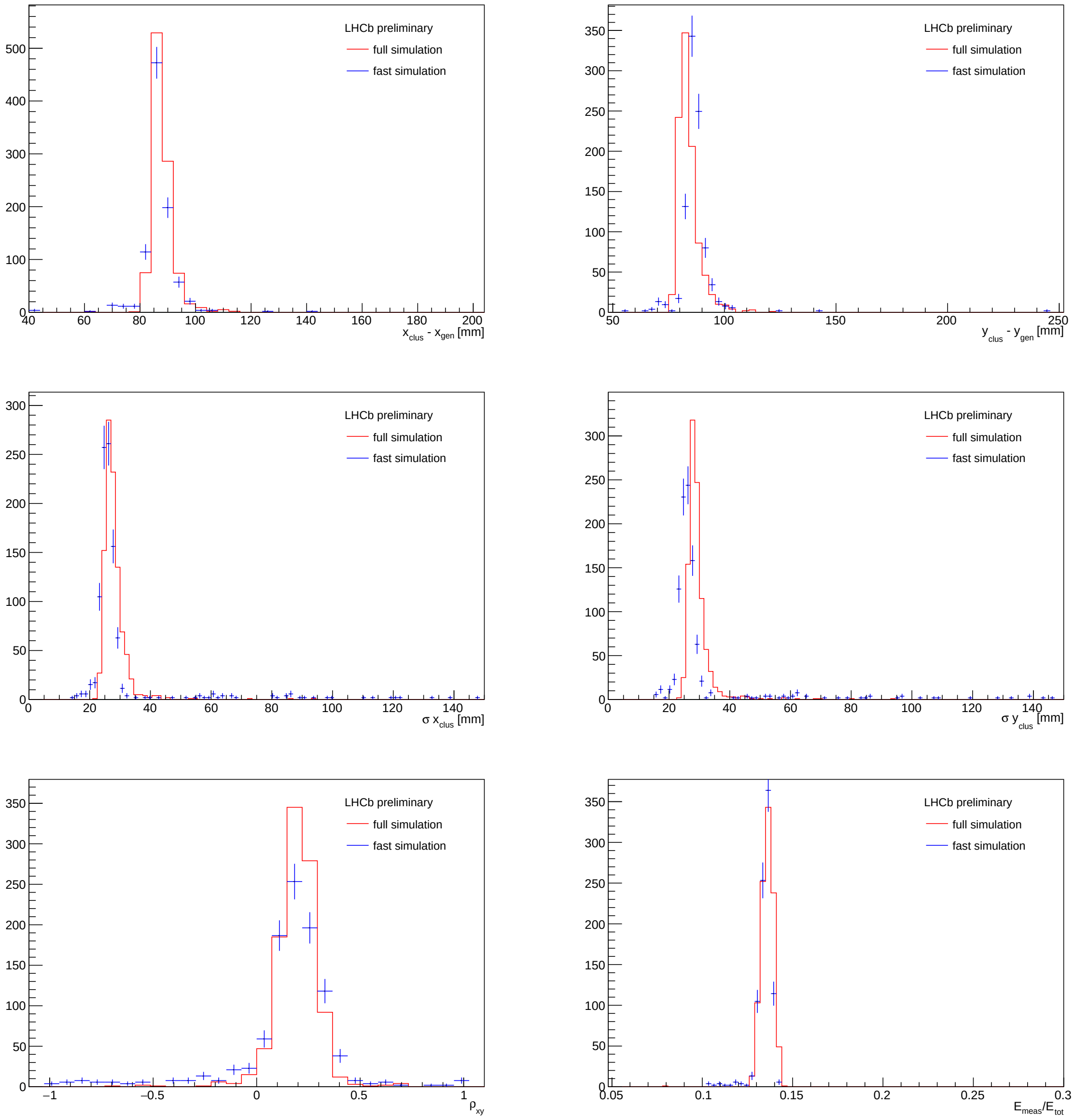

FIGURE 6.7: Comparison between the $X(Y)_c$, $\sigma_{X(Y)}$, ρ_{XY} and E_{frac} distributions for the *point library* model and *Geant4* simulation. The photon has $E = 50$ GeV, $\theta = 0.26$ rad and $\phi = \pi/4$ rad and is generated in the vertex position $x_{gen} = 668$ mm, $y_{gen} = -504$ mm, $z_{gen} = 12290$ mm, that is in the bottom-right quadrant just outside the SPD.

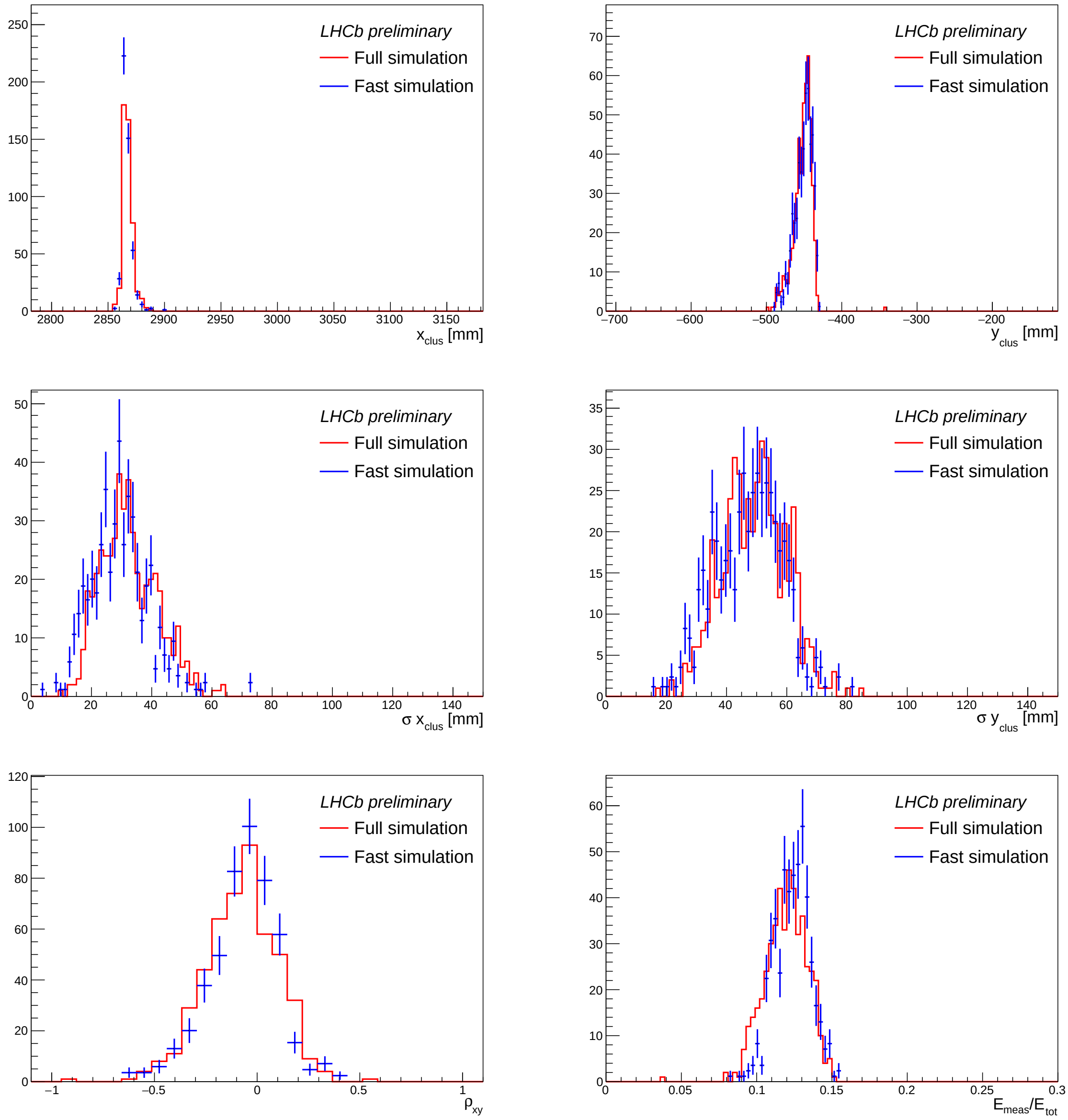

FIGURE 6.8: Comparison between the $X(Y)_c$, $\sigma_{X(Y)}$, ρ_{XY} and E_{frac} distributions for the *point library* model and *Geant4* simulation. The photon has $E = 2.75$ GeV, $\theta = 0.09$ rad and $\phi = \pi/4$ rad. The generated vertex position is $x_{gen} = 668$ mm, $y_{gen} = -504$ mm, $z_{gen} = 12290$ mm for the *point library* and $x_{gen} = 2862$ mm, $y_{gen} = -504$ mm, $z_{gen} = 12290$ mm for the *Geant4* simulation.

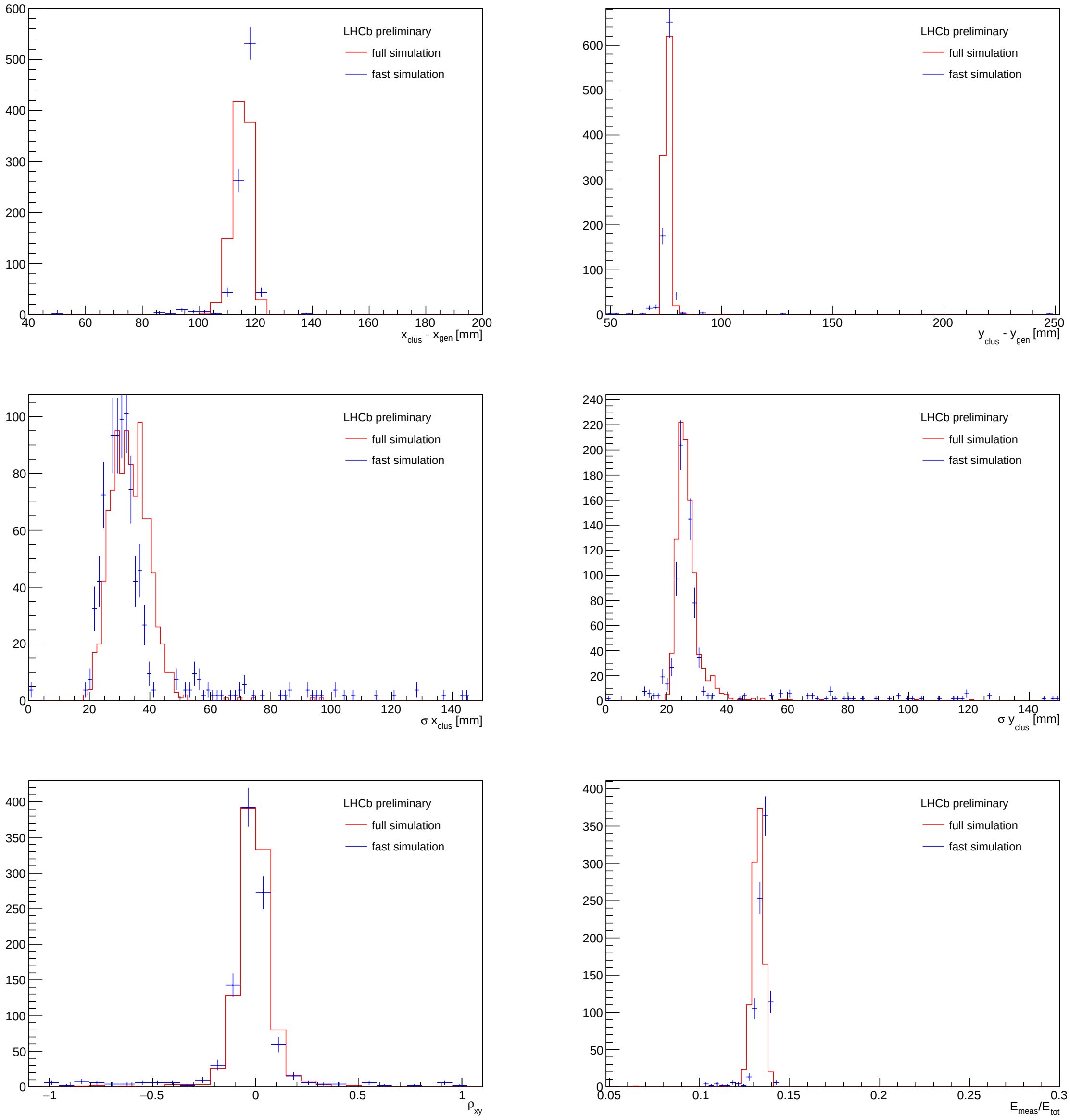

FIGURE 6.9: Comparison between the $X(Y)_c$, $\sigma_{X(Y)}$, ρ_{XY} and E_{frac} distributions for the *point library* model and *Geant4* simulation. The photon has $E = 50$ GeV, $\theta = 0.26$ rad and $\phi = \pi/4$ rad. The generated vertex position is $x_{gen} = 668$ mm, $y_{gen} = -504$ mm, $z_{gen} = 12290$ mm for the *point library* and $x_{gen} = 2862$ mm, $y_{gen} = -504$ mm, $z_{gen} = 12290$ mm for the *Geant4* simulation.

Chapter 7

Conclusions

This thesis presents the development of the first fast simulation interface for the LHCb software and of two fast simulation engines, the single-hit engine and the *point library*, implementing fast simulations of photons in the calorimeter.
The interface has been developed to be flexible enough to allow the users to choose for which subdetector, and for which particles, the fast simulation should replace the standard simulation. Furthermore, for a given subdetector it allows to activate different fast simulation engines depending on the particle properties. In this first implementation of the fast simulation, particles which enter the calorimeter from the beam pipe gap, as opposed to the SPD front face, are stopped without generating hits. This simplification introduces a negligible energy loss in the ECAL and a 5% energy loss in the HCAL.
Timing tests of the single-hit engine have shown a gain of about factor 50 in the simulation time of $O(1)$ GeV energy photons in the calorimeter compared to the standard *Geant4* process. The *point library* allows to achieve a gain of about a factor 20 for photons with energy of $O(1)$ GeV, which improves further at higher energies. Moreover, the comparisons between both engines and the standard *Geant4* simulation have shown a tight agreement that appears to be adequate for most analyses.
The next step in the development of the LHCb calorimeter fast simulation will be the implementation of an appropriate parameterization of the hit position and energy distributions for incident particle whose E and θ values falls between nearest nodes. Moreover, the single-hit model and the *point library* must be implemented in the official MC production. After that, the overheads in terms of library size must be properly evaluated, the models must be debugged and, finally, their physics accuracy must be tested on larger and diverse samples on different types of physics analyses with the help of some beta-testers.
In conclusion, I have shown that it is possible to reduce the simulation time of the LHCb calorimeter, which is currently dominating the simulation time, to a neglible level with respect to other parts of the simulation, while maintaining a similar performance in terms of energy and spatial resolution and reconstruction efficiency. This means a gain in the overall event simulation time of about 50% compared to the standard simulation. The implementation of my code in the official LHCb simulation framework is planned for the first part of 2019. The results of my work also suggest that the application of similar ideas to the RICH detectors could allow to eventually achieve an overall time gain of about 80%, thus increasing the simulated sample statistics by a factor five. This achievement will be very important to unlock the physics potential in a number of key measurements in the LHCb upgrade era.

Bibliography

[1] R Aaij et al. “Implications of LHCb measurements and future prospects”. In: *Eur. Phys. J.* C73.4 (2013), p. 2373. DOI: 10.1140/epjc/s10052-013-2373-2. arXiv: 1208.3355 [hep-ex].

[2] Roel Aaij et al. “Physics case for an LHCb Upgrade II - Opportunities in flavour physics, and beyond, in the HL-LHC era”. In: (2018). arXiv: 1808.08865.

[3] Lyndon Evans and Philip Bryant. “LHC Machine”. In: *Journal of Instrumentation* 3.08 (2008), S08001. URL: http://stacks.iop.org/1748-0221/3/i=08/a=S08001.

[4] A. A. Alves Jr. et al. “The LHCb detector at the LHC”. In: *JINST* 3 (2008), S08005. DOI: 10.1088/1748-0221/3/08/S08005.

[5] LHCb Collaboration. “LHCb VELO TDR: Vertex locator. Technical design report”. In: *CERN-LHCC-2001-011* (2001).

[6] The LHCb Collaboration, A Augusto Alves Jr, et al. “The LHCb Detector at the LHC”. In: *Journal of Instrumentation* 3.08 (2008), S08005. URL: http://stacks.iop.org/1748-0221/3/i=08/a=S08005.

[7] R. P. Bernhard et al. “The LHCb silicon tracker”. In: *Nucl. Instrum. Meth.* A596 (2008), pp. 17–20. DOI: 10.1016/j.nima.2008.07.124.

[8] LHCb Collaboration. “LHCb: Outer tracker technical design report”. In: *CERN-LHCC-2001-024* (2001).

[9] M. Adinolfi et al., LHCb RICH Group. “Performance of the LHCb RICH detector at the LHC”. In: *Eur. Phys. J.* C73 (2013), p. 2431. DOI: 10.1140/epjc/s10052-013-2431-9. arXiv: 1211.6759 [physics.ins-det].

[10] I Machikhiliyan. *The LHCb electromagnetic calorimeter*. Tech. rep. LHCb-PROC-2009-005. LHCb-CONF-2009-005. CERN-LHCb-CONF-2009-005. Geneva: CERN, 2009. URL: https://cds.cern.ch/record/1174766.

[11] Y. Guz et al., LHCb Collaboration. “The LHCb hadron calorimeter”. In: *Journal of Physics: Conference Series, 160(1):12054* (2009).

[12] A A Alves Jr et al. “Performance of the LHCb muon system”. In: *Journal of Instrumentation* 8.02 (2013), P02022. URL: http://stacks.iop.org/1748-0221/8/i=02/a=P02022.

[13] T Head. “The LHCb trigger system”. In: *Journal of Instrumentation* 9.09 (2014), p. C09015. URL: http://stacks.iop.org/1748-0221/9/i=09/a=C09015.

[14] M. Tobin. “Performance of the LHCb Tracking Detectors”. In: *PoS* Vertex2012 (2013), p. 047.

[15] Roel Aaij et al. “Measurement of the $B_s^0 \to \mu^+\mu^-$ branching fraction and effective lifetime and search for $B^0 \to \mu^+\mu^-$ decays”. In: *Phys. Rev. Lett.* 118.19 (2017), p. 191801. DOI: 10.1103/PhysRevLett.118.191801. arXiv: 1703.05747 [hep-ex].

[16] The LHCb collaboration et al. "Measurement of the time-integrated CP asymmetry in D0→ $K_S^0 K_S^0$ decays". In: *Journal of High Energy Physics* 2018.11 (2018), p. 48. ISSN: 1029-8479. DOI: 10.1007/JHEP11(2018)048. URL: https://doi.org/10.1007/JHEP11(2018)048.

[17] Svjetlana Fajfer and Jernej F. et al. Kamenik. "$B \to D^* \tau \overline{\nu}_\tau$ sensitivity to new physics". In: *Phys. Rev. D* 85 (9 2012), p. 094025. DOI: 10.1103/PhysRevD.85.094025. URL: https://link.aps.org/doi/10.1103/PhysRevD.85.094025.

[18] J. P. Lees and V. et al. Poireau. "Measurement of an excess of $\overline{B} \to D^{(*)} \tau^- \overline{\nu}_\tau$ decays and implications for charged Higgs bosons". In: *Phys. Rev. D* 88 (7 2013), p. 072012. DOI: 10.1103/PhysRevD.88.072012. URL: https://link.aps.org/doi/10.1103/PhysRevD.88.072012.

[19] Y. Sato et al. "Measurement of the branching ratio of $\bar{B}^0 \to D^{*+} \tau^- \bar{\nu}_\tau$ relative to $\bar{B}^0 \to D^{*+} \ell^- \bar{\nu}_\ell$ decays with a semileptonic tagging method". In: *Phys. Rev.* D94.7 (2016), p. 072007. DOI: 10.1103/PhysRevD.94.072007. arXiv: 1607.07923 [hep-ex].

[20] R. Aaij et al. "Test of Lepton Flavor Universality by the measurement of the $B^0 \to D^{*-} \tau^+ \nu_\tau$ branching fraction using three-prong τ decays". In: *Phys. Rev.* D97.7 (2018), p. 072013. DOI: 10.1103/PhysRevD.97.072013. arXiv: 1711.02505 [hep-ex].

[21] Rick Field. "Min-Bias and the Underlying Event at the LHC". In: *Proceedings, 31st International Conference on Physics in collisions (PIC 2011): Vancouver, Canada, August 28-September 1, 2011.* 2012. arXiv: 1202.0901 [hep-ph].

[22] Yung-Su Tsai. "Pair production and bremsstrahlung of charged leptons". In: *Rev. Mod. Phys.* 46 (4 1974), pp. 815–851. DOI: 10.1103/RevModPhys.46.815. URL: https://link.aps.org/doi/10.1103/RevModPhys.46.815.

[23] S Miglioranzi et al. *The LHCb Simulation Application, Gauss: Design, Evolution and Experience.* Tech. rep. LHCb-PROC-2011-006. CERN-LHCb-PROC-2011-006. Geneva: CERN, 2011. URL: https://cds.cern.ch/record/1322402.

[24] S. Agostinelli et al. "Geant4—a simulation toolkit". In: *Nuclear Instruments and Methods in Physics Research Section A: Accelerators, Spectrometers, Detectors and Associated Equipment* 506.3 (2003), pp. 250 –303. ISSN: 0168-9002. DOI: https://doi.org/10.1016/S0168-9002(03)01368-8. URL: http://www.sciencedirect.com/science/article/pii/S0168900203013688.

[25] G. Barrand et al. "GAUDI — A software architecture and framework for building HEP data processing applications". In: *Computer Physics Communications* 140.1 (2001). CHEP2000, pp. 45 –55. ISSN: 0010-4655. DOI: https://doi.org/10.1016/S0010-4655(01)00254-5. URL: http://www.sciencedirect.com/science/article/pii/S0010465501002545.

[26] R Aaij et al. "Measurement of CP asymmetries in $D^\pm \to \eta' \pi^\pm$ and $D_s^\pm \to \eta' \pi^\pm$ decays". In: *Physics Letters B* 771 (May 2017). DOI: 10.1016/j.physletb.2017.05.013.

[27] N. L. Johnson. "Systems of frequency curves derived from the first law of Laplace". In: *Trabajos de Estadistica* 5.3 (1955), pp. 283–291. ISSN: 0490-219X. DOI: 10.1007/BF03005988. URL: https://doi.org/10.1007/BF03005988.

[28] P. del Amo Sanchez et al. "Study of $B \to X\gamma$ Decays and Determination of $|V_{td}/V_{ts}|$". In: *Phys. Rev.* D82 (2010), p. 051101. DOI: 10.1103/PhysRevD.82.051101. arXiv: 1005.4087 [hep-ex].